

Electronic Theses and Dissertations, 2004-2019

2013

Heat And Fluid Flow Characterization Of A Single-hole-per-row Impingement Channel At Multiple Impingement Heights

Roberto Claretti
University of Central Florida

 Part of the [Mechanical Engineering Commons](#)
Find similar works at: <https://stars.library.ucf.edu/etd>
University of Central Florida Libraries <http://library.ucf.edu>

This Masters Thesis (Open Access) is brought to you for free and open access by STARS. It has been accepted for inclusion in Electronic Theses and Dissertations, 2004-2019 by an authorized administrator of STARS. For more information, please contact STARS@ucf.edu.

STARS Citation

Claretti, Roberto, "Heat And Fluid Flow Characterization Of A Single-hole-per-row Impingement Channel At Multiple Impingement Heights" (2013). *Electronic Theses and Dissertations, 2004-2019*. 2936.
<https://stars.library.ucf.edu/etd/2936>

HEAT AND FLUID FLOW CHARACTERIZATION OF A SINGLE-HOLE-PER-ROW
IMPINGEMENT CHANNEL AT MULTIPLE IMPINGEMENT HEIGHTS

by

ROBERTO CLARETTI
B.S. University of Central Florida, 2011

A thesis submitted in partial fulfillment of the requirements
for the degree of Master of Science
in the Department of Mechanical and Aerospace Engineering
in the College of Engineering and Computer Science
at the University of Central Florida
Orlando, Florida

Fall Term
2013

Major Professor: Jayanta Kapat

© 2013 Roberto Claretti

ABSTRACT

The present work studies the relationship between target and sidewall surfaces of a multi-row, narrow impingement channel at various jet heights with one impingement hole per row. Temperature sensitive paint and constant flux heaters are used to gather heat transfer data on the target and side walls. Jet-to-target distance is set to 1, 2, 3, 5, 7 and 9 jet diameters. The channel width is 4 jet diameters and the jet stream wise spacing is 5 jet diameters. All cases were run at Reynolds numbers ranging from 5,000 to 30,000. Pressure data is also gathered and used to calculate the channel mass flux profiles, used to better understand the flow characteristics of the impingement channel. While target plate heat transfer profiles have been thoroughly studied in the literature, side wall data has only recently begun to be studied. The present work shows the significant impact the side walls provide to the overall heat transfer capabilities of the impingement channel. It was shown that the side walls provide a significant amount of heat transfer to the channel. A channel height of three diameters was found to be the optimum height in order to achieve the largest heat transfer rates out of all channels.

DEDICATED TO ENNIO, MAMA Y PAPA.

To those with a never-ending thirst for knowledge

ACKNOWLEDGMENTS

Special thanks to my thesis chair Dr. Kapat; your advice has been invaluable. I would also like to thank the rest of my committee members, Dr. Raghavan, Dr. Vasu and Dr. Kassab.

I would like to acknowledge the help I received from John Harrington on the final phases of testing and the help Joshua Bernstein and Jahed Hossain have given me. Thanks to everyone I worked with on FCFC: Greg Natsui, Constantine Wolski, Justin Hodges, Jonathan Allred, Mark Miller and Orlando Ardila. Thanks to Anthony Bravato for keeping the lab together; thanks to Matt Golsen, Mark Ricklick, Lucky Tran, Abhishek Saha, Perry Johnson and Carson Slabaugh for answering the questions I had and engaging in thoughtful discussions about all aspects of turbomachinery and life in general.

Thanks to Jim Downs, Gloria Goebel, An Lee, Michelle Valentino and Bryan Bernier for their kind hospitality over my internship at FTT. Thanks again to Mark Ricklick and everyone else at CD-Adapco for showing me how to work with StarCCM+.

More recently I would like to thank everyone at GRC including Brian Barr, Jon Slepski, Jeff Doom, Suranga Dharmarathne, and Greg Natsui again! for making my stay as a GRC intern memorable.

TABLE OF CONTENTS

LIST OF FIGURES	viii
LIST OF TABLES.....	xi
LIST OF NOMENCLATURE	xii
CHAPTER ONE: INTRODUCTION.....	1
Gas Turbine as a Heat Engine.....	1
Cooling of Gas Turbine Hot Components	4
CHAPTER TWO: LITERATURE REVIEW	5
Impingement Heat Transfer	5
Numerical Impingement Heat Transfer	5
Single Round Nozzle Impingement Heat Transfer.....	7
Impingement Flow Visualization.....	9
Impingement Arrays	10
Impingement Heat Transfer Reviews	14
Other Impingement Literature	15
Experimental Techniques.....	17
CHAPTER THREE: PURPOSE AND PROBLEM STATEMENT	18
CHAPTER FOUR: EXPERIMENTAL SETUP AND DATA REDUCTION.....	20
Data Reduction.....	27

Lateral Conduction Estimation	32
CHAPTER FIVE: EXPERIMENTAL UNCERTAINTY	34
CHAPTER SIX: FLOW RESULTS	37
CHAPTER SEVEN: HEAT TRANSFER RESULTS	39
Smooth Channel Validation	39
Heat Transfer Results.....	40
CHAPTER EIGHT: HEAT TRANSFER DATA ANALYSIS	48
Nusselt Number Dependence of Reynolds number	48
Total Heat Transfer Contribution.....	50
Comparisons with Florschuetz et al. [18] Correlation	52
CHAPTER NINE: CONCLUSIONS.....	55
APPENDIX A: NUSSELT NUMBER PROFILES.....	56
APPENDIX B: SPAN AVERAGED NUSSELT NUMBER DATA.....	62
APPENDIX C: TABULATED NUSSELT NUMBER DATA	69
APPENDIX D: ACTUAL REYNOLDS NUMBERS	76
APPENDIX E: LATERAL CONDUCTION CALCULATIONS	78
REFERENCES	81

LIST OF FIGURES

Figure 1: Energy Consumption in Electricity Generation (10^{15} BTU).....	1
Figure 2: Energy Uses in the United States and their Respective Sources.....	2
Figure 3: Turbine airfoil cooled with a series of impingement channel with heat paths showing importance of side wall heat transfer	19
Figure 4: Isometric view of $Z/D=1$ impingement channel CAD	21
Figure 5: Impingement channel geometric parameters.....	21
Figure 6: Impingement channel flow loop and camera setup.....	22
Figure 7: Temperature sensitive paint calibration setup.....	25
Figure 8: Temperature sensitive paint calibration results and comparisons with older correlations	26
Figure 9: 1D diagram of test section layers (not drawn to scale)	27
Figure 10: Conduction Loss Diagram.....	28
Figure 11: Heat loss results and correlation.....	29
Figure 12: Sample Pressure Profile.....	30
Figure 13: Lateral Conduction Estimates	33
Figure 14: Absolute Uncertainties of Nusselt Number.....	35
Figure 15: Absolute Uncertainties of Reynolds Number.....	36
Figure 16: Channel mass flux to jet mass flux ratio distribution.....	37
Figure 17: Local jet mass flux to average jet mass flux ratio and comparisons to analytical models.....	38
Figure 18: Smooth Channel Validation	40

Figure 19: Target Wall Comparison at $Re_{j_{avg}}=10,000$	42
Figure 20: Target Wall Comparison at $Re_{j_{avg}}=15,000$	42
Figure 21: Side Wall Comparison at $Re_{j_{avg}}=10,000$	43
Figure 22: Side Wall Comparison at $Re_{j_{avg}}=15,000$	44
Figure 23: Target Wall Nusselt number Comparisons at $Re_{j_{avg}}=15,000$	45
Figure 24: Side Wall Nusselt number Comparisons at $Re_{j_{avg}}=15,000$	45
Figure 25: Isometric View of all Channels at $Re_{j_{avg}}=10,000$	47
Figure 26: Isometric View of all Channels at $Re_{j_{avg}}=15,000$	47
Figure 27: Variation of Reynolds Number Exponent, "m", as a Function of Wall and Channel Height.....	49
Figure 28: Contributions of Target and Side Walls on Overall Channel Heat Transfer for $Re_{j_{avg}}=10,000$	51
Figure 29: Contributions of Target and Side Walls on Overall Channel Heat Transfer for $Re_{j_{avg}}=15,000$	52
Figure 30: $Z/D = 2$ Nusselt Number Profile Comparisons with Florschuetz et al.....	53
Figure 31: $Z/D = 3$ Nusselt Number Profile Comparisons with Florschuetz et al.....	54
Figure 32: $Z/D=1$ Target Wall Nusselt number Profiles at Multiple Reynolds Numbers	57
Figure 33: $Z/D=2$ Target Wall Nusselt number Profiles at Multiple Reynolds Numbers	57
Figure 34: $Z/D=3$ Target Wall Nusselt number Profiles at Multiple Reynolds Numbers	57
Figure 35: $Z/D=5$ Target Wall Nusselt number Profiles at Multiple Reynolds Numbers	58
Figure 36: $Z/D=7$ Target Wall Nusselt number Profiles at Multiple Reynolds Numbers	58
Figure 37: $Z/D=9$ Target Wall Nusselt number Profiles at Multiple Reynolds Numbers	58
Figure 38: $Z/D=1$ Side Wall Nusselt number Profiles at Multiple Reynolds Numbers	59

Figure 39: $Z/D=2$ Side Wall Nusselt number Profiles at Multiple Reynolds Numbers	59
Figure 40: $Z/D=3$ Side Wall Nusselt number Profiles at Multiple Reynolds Numbers	59
Figure 41: $Z/D=5$ Side Wall Nusselt number Profiles at Multiple Reynolds Numbers	60
Figure 42: $Z/D=7$ Side Wall Nusselt number Profiles at Multiple Reynolds Numbers	60
Figure 43: $Z/D=9$ Side Wall Nusselt number Profiles at Multiple Reynolds Numbers	61
Figure 44: Target Wall Laterally Averaged Nusselt Number for $Z/D=1$	63
Figure 45: Side Wall Laterally Averaged Nusselt Number for $Z/D=1$	63
Figure 46: Target Wall Laterally Averaged Nusselt Number for $Z/D=2$	64
Figure 47: Wall Laterally Averaged Nusselt Number for $Z/D=2$	64
Figure 48: Target Wall Laterally Averaged Nusselt Number for $Z/D=3$	65
Figure 49: Wall Laterally Averaged Nusselt Number for $Z/D=3$	65
Figure 50: Target Wall Laterally Averaged Nusselt Number for $Z/D=5$	66
Figure 51: Wall Laterally Averaged Nusselt Number for $Z/D=5$	66
Figure 52: Target Wall Laterally Averaged Nusselt Number for $Z/D=7$	67
Figure 53: Wall Laterally Averaged Nusselt Number for $Z/D=7$	67
Figure 54: Target Wall Laterally Averaged Nusselt Number for $Z/D=9$	68
Figure 55: Wall Laterally Averaged Nusselt Number for $Z/D=9$	68

LIST OF TABLES

Table 1: Florschuetz Correlation Constants for an Inline Array.....	11
Table 2: Test Matrix.....	23
Table 3: Absolute and Relative Nusselt Number Uncertainties	34
Table 4: Absolute and Relative Reynolds Number Uncertainties	35
Table 5: Nusselt Number Dependence on Reynolds Number	48
Table 6: Total Channel Heat Transfer	50
Table 7: Z/D=1 Target Wall Pitch Averaged Nusselt Number	70
Table 8: Z/D=1 Side Wall Pitch Averaged Nusselt Number	70
Table 9: Z/D=2 Target Wall Pitch Averaged Nusselt Number	71
Table 10: Z/D=2 Side Wall Pitch Averaged Nusselt Number	71
Table 11: Z/D=3 Target Wall Pitch Averaged Nusselt Number	72
Table 12: Z/D=3 Side Wall Pitch Averaged Nusselt Number	72
Table 13: Z/D=5 Target Wall Pitch Averaged Nusselt Number	73
Table 14: Z/D=5 Side Wall Pitch Averaged Nusselt Number	73
Table 15: Z/D=7 Target Wall Pitch Averaged Nusselt Number	74
Table 16: Z/D=7 Side Wall Pitch Averaged Nusselt Number	74
Table 17: Z/D=9 Target Wall Pitch Averaged Nusselt Number	75
Table 18: Z/D=9 Side Wall Pitch Averaged Nusselt Number	75
Table 19: Actual Reynolds Numbers	77

LIST OF NOMENCLATURE

A_{cs}	Cross Sectional Area
A_h	Heater Surface Area (m ²)
c_p	Specific Heat at Constant Pressure (kJ/kg K)
D	Jet Diameter (m)
D_{ch}	Channel Hydraulic Diameter (m)
h	Heat Transfer Coefficient (HTC) (W/m ² K)
\bar{h}	Average Heat Transfer Coefficient (W/m ² K)
k	Thermal Conductivity (W/m K)
L	Channel Length (m)
\dot{m}	Mass Flow Rate (kg/s)
Nu	Nusselt Number
P	Static Pressure (kPa)
P_0	Total Pressure (kPa)
Pr	Prandtl Number
q''	Heat Flux (W/m ²)
Q	Total Heat Input (W)
R_h	Heater Resistance (ohm)
Re	Reynolds Number
SW	Side Wall
T	Temperature (K)
TW	Target Wall

V	Voltage Potential
x	Streamwise Location
y	Spanwise Location
z	Height from Target Wall
X	Streamwise Distance (m)
Y	Spanwise Distance (m)
Z	Impingement Height (m)
γ	Ratio of Specific Heats
ρ	Air Density (kg/m^3)

Subscripts

C	Cold
cs	Cross-section
ch	Channel
$Carnot$	Describing a Carnot cycle
e	Exit
eff	Effective
H	Hot
j_{avg}	Average jet quantity (applicable to Re)
$loss$	Quantity Lost to the Environment
$reff$	Reference Value
w	Wall Value
0	Base Line Value or Total Quantity

CHAPTER ONE: INTRODUCTION

Gas Turbine as a Heat Engine

Gas turbines power all commercial and military aircraft as well as provide a quarter of the electricity generated in the United States [1]. With the rising environmental, political and fuel cost of the operation of these engines, users are seeking to increase their efficiency. To put electricity generation into perspective, Figure 1 shows the total amount of energy used in the generation of electrical power in the United States. A total of 40.04 quadrillion BTUs are used to generate 14.82 quadrillion BTUs of electrical power — a conversion rate of 37%. Out of the 40.04 quadrillion BTUs of total energy used, 8.05 quadrillion BTUs come from natural gas, the primary fuel power generation gas turbines operate on. Jet fuel accounts for 7.6% of the petroleum consumption in the US at 1.43 million barrels per day [1]. The scale of energy use in the United States displays the major benefits obtainable from an increase of efficiency of gas turbine engines.

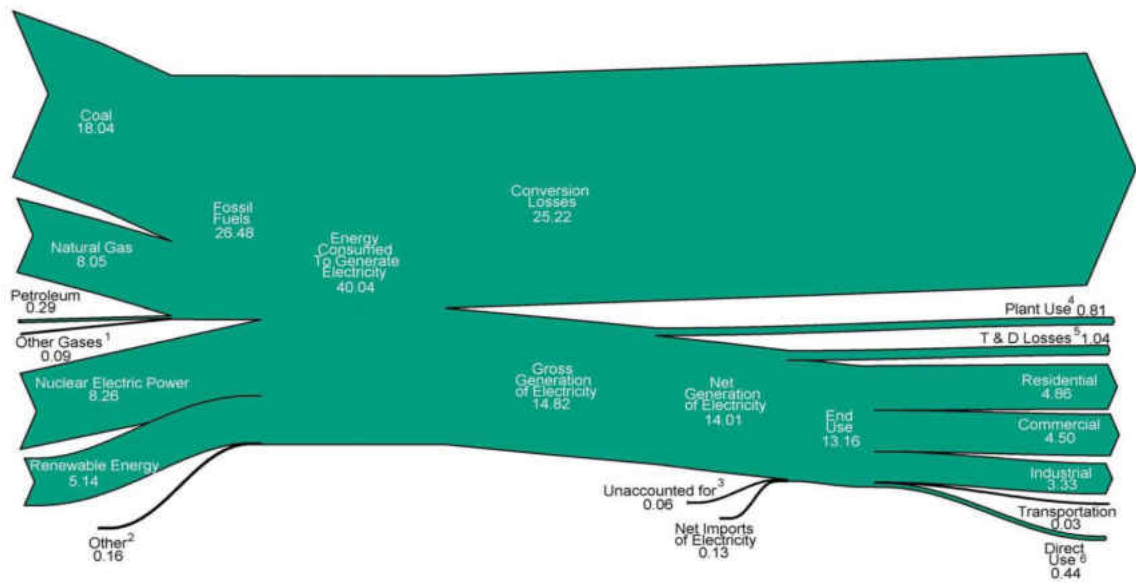


Figure 1: Energy Consumption in Electricity Generation (10¹⁵ BTU)

Source: DOE U.S. Energy Information Administration Annual Energy Review

<http://www.eia.gov/totalenergy/data/annual/pdf/aer.pdf>

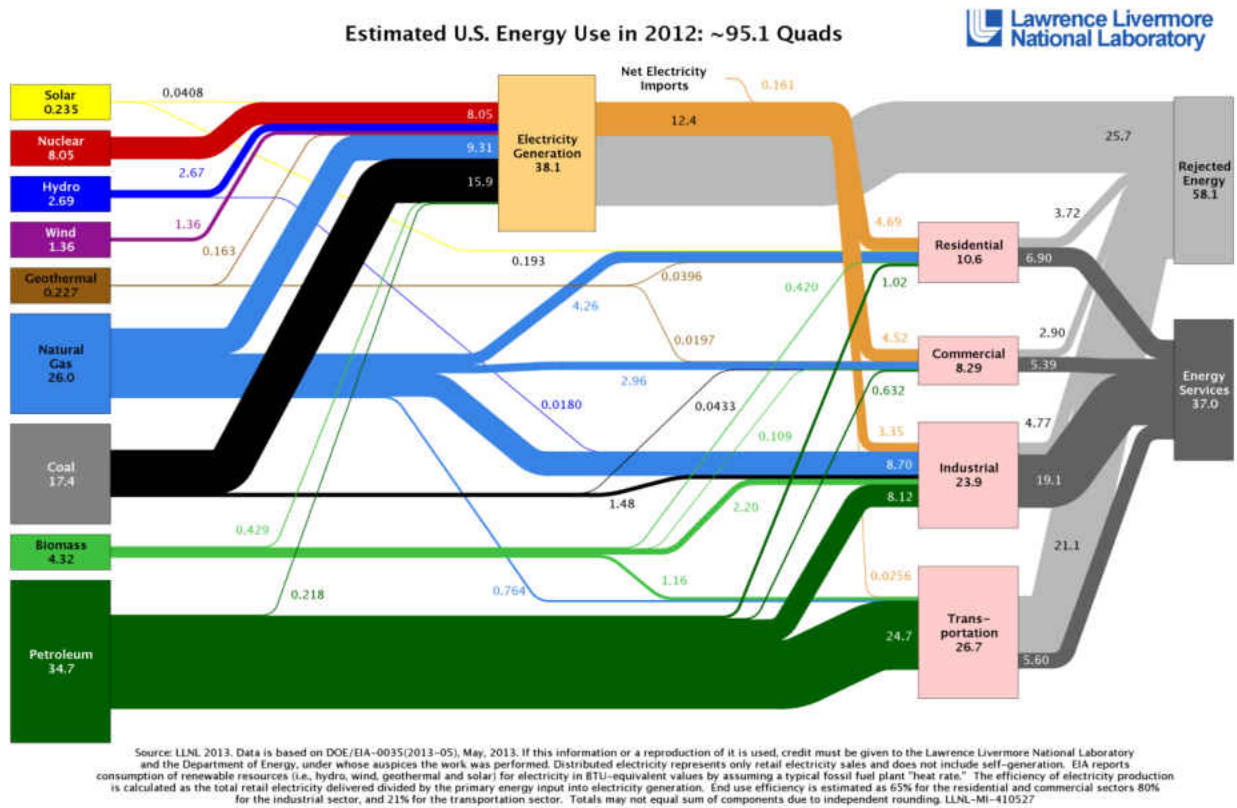


Figure 2: Energy Uses in the United States and their Respective Sources.

Source: Lawrence Livermore National Laboratory Energy Flow Charts

<https://flowcharts.llnl.gov/>

Contrary to the chart shown in Figure 1, which only shows the flow of energy used in the generation of electrical power, Figure 2 also contains energy used for transportation. It can be seen that transportation is the main user of petroleum products. Transportation features the lowest conversion efficiency out of all sources of energy at a meager 21%. Gas turbines are used to power some modes of transportation including all commercial and military aircraft and some sea vessels; increasing the efficiency of these engines not only decreases the cost of electricity but also decreases the cost of some modes of transportation.

Gas turbines are modeled thermodynamically by the Brayton Cycle. The cycle entails three main processes that can be directly tied to different parts of a gas turbine. Pressure is increased in the compressor; heat is added by combusting natural gas or gasified coal on power generation engines and jet fuel on aviation engines; energy is then extracted from the working fluid (post combustion gasses) in the turbine which provides power to the compressor and to the generator on power generation gas turbines and to the compressor and fan on aviation engines. The exhaust is deposited in the atmosphere for all aviation engines and simple cycle power generation engines; for combined cycle power generation, the exhaust gases are fed through a heat recovery steam generator, or HRSG, where, as the name describes, some of the remaining heat from the post-combustion gasses is transferred to steam which is then used to power steam turbines. The use of the waste heat drastically improves the overall efficiency of the power plant.

The isentropic efficiency of Brayton Cycle engines is given by

$$\eta_{Brayton} = 1 - \frac{T_1}{T_2} = 1 - \frac{1}{Pr^{\frac{\gamma-1}{\gamma}}} \quad (1)$$

Using the isentropic efficiency to determine what aspect of a real engine should be improved is appropriate due to the fact that even if the real engine efficiency cannot be determined using the isentropic efficiency, an increase in isentropic efficiency will be reflected in the real engine efficiency. It is therefore possible to analyze the Brayton cycle using the isentropic efficiency to determine possible improvements. A decrease in T_1 would increase the efficiency; however, since T_1 is the atmospheric temperature, engineers have little control of it other than location of certain power plant, or the cruising altitude of an airliner. The other option engineers have is to increase the turbine inlet temperature, T_3 . The problem in increasing the turbine inlet temperature is that the current temperature gas turbines operate on is higher than the melting point of the materials that they are made out of [2], [3], [4]. Current gas turbines are

cooled with compressor bypass air that flow through cooling channels in the turbine blades and vanes as well as in the transition duct; the cooling air is the bled out onto the hot surfaces as film cooling which provides a cooling blanket of air protecting the surface from the hot gasses. Cooling alone is not sufficient enough to assure the reliable operation of gas turbine hot components. Designers employ the use of nickel-based super alloys which are coated with thermal barrier coatings. It is the combination of the high-temperature capable super alloys, thermal barrier coatings and internal and external cooling that allow the continuous operation of the critical components in the harsh environment.

Cooling of Gas Turbine Hot Components

Gas turbine blades are cooled multiple ways depending on the manufacturer. Early versions of cooled blades only contained radial convective cooling channels. As time progressed, cooling technologies as well as better super alloys and thermal barrier coatings were developed and deployed. Modern blades are cooled with serpentine channels in the midchord region lined with turbulators to enhance their heat transfer capability, pin fin arrays located in the trailing edge region and impingement cooling coupled with showerhead cooling on the leading edge. Vanes, or stators, are cooled with an array of impinging jets generated by a jet-inducing insert. The vanes are also lined with showerhead cooling holes on the leading edge and film cooling holes on the pressure and suction sides as well as on both endwalls. Transition ducts are cooled with channels lined with turbulators as well as impingement and multiple rows of film cooling. Designers have begun to take advantage of the cooling capability of impingement due to the large heat transfer coefficients it generates at a given coolant mass flow rate.

CHAPTER TWO: LITERATURE REVIEW

Impingement Heat Transfer

Impingement cooling has been researched since the early 1960s. Hundreds of papers have been published describing the heat transfer and flow characteristics of single round nozzle impingement, staggered and inline impingement arrays, impingement on curved surfaces to simulate the ones found on a leading edge, angled impingement, swirling jets, impingement on surfaces with porous foam and turbulators, flow visualization, coupled impingement-effusion, effects of nozzle geometry and multiple other geometric, flow or heat transfer studies.

Due to the large breadth of literature on impingement cooling, only relevant work to the present study as well as multiple cornerstone studies on impingement heat transfer are discussed in detail.

Numerical Impingement Heat Transfer

Multiple works have studied numerical simulations of impingement heat transfer. El-Gabry [5] performed a numerical investigation of an impingement channel which consisted of 8 streamwise holes. The paper investigated the Nusselt number prediction differences between two different turbulence models; the Yang-Shih and standard k- ϵ . Computational results were compared to experimental results obtained previously. Two channel heights were tested of 1 and 2 jet diameters; three jet inclinations were also tested at 30, 60 and 90 degrees off of the target wall normal. The deviation of Nusselt number between the experimental and computational results were calculated. The Yang-Shih turbulence model predicted well at low Reynolds numbers as the area averaged Nusselt number being 5% off from the experimental value while the standard k- ϵ was off by 9.4%. As jet Reynolds number was increased, the error of the standard k- ϵ model dropped to as low as 3.9% higher than the experimental data while the error from the Yang-shih model increased to

7.6% below the experimental average. Plots containing experimental and computational span-averaged Nusselt number results are shown. A peak of Nusselt number is predicted by both codes directly beneath the stagnation region; however, the magnitude of the span-averaged Nusselt number profile of both numerical solutions is higher than the experimental one. The amplitude of fluctuations is greater for the CFD solutions; it is important to note that even though the error in average Nusselt number is not great, the actual differences in the profile are much greater; upwards of 20% difference of heat transfer coefficients between the experimental and numerical heat transfer peaks. Such discrepancy may not be entirely due to numerical errors and/or the inability for either turbulence model to predict the heat transfer at the stagnation regions; it may also be caused to potential lateral conduction on the experimental side.

Zuckerman, et al. [6] compared a much wider array of turbulence models in their ability to predict Nusselt numbers caused by jet impingement. The models tested were $k - \epsilon$, $k - \omega$, Reynolds Stress Model, algebraic stress models, shear stress transport and lastly, the v^2f turbulence model. Large eddy simulation was run as the only time-dependent turbulence model. The paper summarizes all the different models used, their computational cost, impingement Nusselt number, and their ability to predict the secondary peak encountered at low impingement heights. As expected LES provide the best prediction of both stagnation and secondary peak heat transfer coefficient; however, this comes at a large computational cost. The $k - \epsilon$ and $k - \omega$ provide poor heat transfer results for the stagnation region where they can have 30% error from the correct value. The realizable $k - \epsilon$ model provides better heat transfer results while still maintaining a low computational cost. The highest accuracy to cost ratio was achieved by the v^2f model where it predicts the heat transfer coefficient for the surface with a minimum of 2% error while not being as expensive as the other unsteady models such as DNS and LES.

Mushatat [7] performed basic 2-D computational studies on a slot impingement channel with initial crossflow. Multiple numbers of slot jets were studied as well as rib features on the target wall. Nusselt number plots were shown and discussed with little comparison of the results with previous literature. The work shows an increase in target wall heat transfer with an increase in slot velocity at constant crossflow velocity; an increase of the ratio of slot jet width to rib thickness yielded an increase in Nusselt number.

Taslim, et al. [8] investigated numerically and experimentally the heat transfer characteristics of jet impingement on a curved leading edge surface with and without ribs. The highest area average convective coefficients were found on the rib-less geometry. One of the ribbed geometries tested yielded the highest rate of heat transfer due to the increased wetted area - a result commonly found on internal cooling enhancement with the use of rib turbulators.

Acharya, et al. [9] examined velocity profiles generated by the exhaust of flow incoming through a circular tube into a crossflow similar to geometries seen in showerhead film cooling. Incoming flow carried a preset velocity which decreased as flow was removed from it as it exited through orifices on the tube. Velocity profiles for flow through each orifice is shown and are used to understand the different jet velocity profiles generated with varying crossflow conditions.

Single Round Nozzle Impingement Heat Transfer

Single round nozzle impingement consists of a single jet impinging a surface with the spent air exiting in the radial direction. Multiple variations have been studied in the literature.

Gulati, et al. [10] studied the effect of different nozzle shapes including round, square, and rectangular nozzle at Z/D of 0.5, 1, 2, 4, 6, 8, 10, and 12 with D being the hydraulic diameter of the respective jet. The Nusselt number profile closely resembled the shape of the nozzle at low

impingement heights; however, as the impingement height increased, the profile lost its shape as the jet lost its momentum by diffusion. Rectangular jets were found to have radially varying profiles even at large impingement heights. The Reynolds number dependence of Nusselt number was not found to be altered by nozzle shape implying the hydraulic diameter correctly predicted the length scale of the different shaped jets. The pressure loss due to the jet formation and impingement was found to be lowest for the circular shape and highest for the rectangular shape – this result is expected due to the jets being allowed to develop for 50 jet hydraulic diameters, causing a large pressure drop on the rectangular jet due to the larger wetted area. Herrero-Martin et al. [11] studied two types of nozzle shapes and their effect on target wall Nusselt number distribution. The two different nozzles consisted of the intersection of three circular profiles located at the three vertices of an equilateral triangle with a side length equal to the diameter of the circles and the intersection of four circular jets whose center was located on each corner of a square whose side was slightly smaller than the diameter of the jets; they are named triangular nozzle and quadrangular nozzle respectively. Several impingement heights were tested $Z/D = 1, 2, 3, 4, 5, 6, 7,$ and 12 . The performance of the different nozzles were found to be a function of Reynolds number; at a Reynolds number greater than $15,000$, the quadrangular nozzle delivered the highest rate of heat transfer while the triangular nozzle performed better at Reynolds numbers less than $15,000$. Lee, et al. [12] studied round nozzles with variations of the finish on the flow side of the jet-issuing-plate. Three geometries were tested, one with a square edged exit, one with a chamfered exit and one with a sharp exit. The thickness of the jet-issuing-plate was $1/5$ of the jet diameter, $L/D=1/5$. Multiple impingement heights were tested $Z/D = 2, 4, 6,$ and 10 . The Nusselt number dependence factor on Reynolds number was found not to be a function of nozzle finish. Slight variations in the area averaged

Nusselt number were found with varying nozzle finish. The authors provided Nusselt number correlations for all three nozzle finishes. The nozzle with the square exit was found to be the most beneficial due to it scaling at a higher rate with an increase of Reynolds number.

Other work on single round nozzle impingement is given in literature reviews, most notably in Martin [13], Viskanta [14], and Weigand et al. [15]. These works are discussed in more detail in the impingement review section.

Impingement Flow Visualization

Carcasci [16] used multiple flow visualization techniques to study the resulting flow field caused by numerous types of impingement geometries. The techniques used included oil and pigment on a wall (target wall in this case), thermo-tropic liquid crystal on a wall as well as a simple smoke flow test. The different geometries tested included a single round nozzle impingement, inline jet interactions (similar to the geometry studied in this work) inline jet interaction with the effect of crossflow and finally, a geometry consisting 9 jets in a square pattern with crossflow. The paper explains the difference in secondary vortices generated between a jet impinging on a surface with and without crossflow. The addition of crossflow causes the main wall jet from an upstream jet to separate from the wall as it meets the wall jet caused by a jet impinging directly downstream causing an effect similar to a hydraulic jump in the wall jet stagnation region. The high turbulence shown in this region is used to explain relatively higher convective coefficients when compared to regions of wall jets with no interaction with other flows. The study does not take into account side walls used in the inline cases; it would be beneficial for future impingement researchers to study the flow behavior at the

side walls (with oil and dye) in order to better understand the interaction of the wall jet and the side wall and its effect on heat transfer.

Impingement Arrays

Among the most well known impingement heat transfer studies lays the Florschuetz, et al. NASA technical reports and corresponding journal articles [17],[18] and[19] (at the time of writing, the NASA reports have been taken down from the NASA FOIA website).The research done by Florschuetz et al. studied an impingement array with the purpose of finding the optimum lateral and streamwise jet spacing, Y/D and X/D respectively, in order to maximize the target wall heat transfer. Jet-to-target wall spacing, Z/D ranged from 1 to 3, the streamwise spacings tested were X/D=5, 10 and 15 while the lateral spacing was kept at Y/D 4, 6 and 8. Florschuetz's et al. major contribution was the development of a correlation which provided a relationship between jet area average Nusselt number as a function of flow and geometric parameters. The correlation takes the form

$$Nu = A(Re_j)^m \left\{ 1 - B \left[\left(\frac{Z}{d} \right) \left(\frac{G_c}{G_j} \right) \right]^n \right\} * Pr^{1/3} \quad (2)$$

with A, m, B and n being functions of geometric parameters calculated using the following correlation

$$n = C \left(\frac{X}{D} \right)^{n_x} \left(\frac{Y}{D} \right)^{n_y} \left(\frac{Z}{D} \right)^{n_z} \quad (3)$$

The constants C, n_x , n_y , and n_z are given in Table 1 for an inline array

Table 1: Florschuetz Correlation Constants for an Inline Array

	C	nx	ny	nz
A	1.18	-0.944	-0.642	0.169
m	0.612	0.059	0.032	-0.022
B	0.437	-0.095	-0.219	0.275
n	0.092	-0.005	0.599	1.04

Florschuetz et al. also developed a one dimensional analytical flow model useful for the study of flow distribution inside impingement arrays; the first is an equation that provides the local jet mass flux, G , normalized by the average jet mass flux. This relationship is useful due to the Reynolds number being specified as the average jet Reynolds number instead of local jet Reynolds number. By multiplying the average jet Reynolds number by the ratio of jet to average jet mass flux, the local jet Reynolds number is acquired. The equation takes the form of

$$\frac{G_j}{G_{javg}} = \beta * N_c * \frac{\cosh\left(\beta\left(\frac{x}{x_n}\right)\right)}{\sinh(\beta * N_c)} \quad (4)$$

The second flow equation shown in the Florschuetz et al. reports provides a relationship between the ratio of local channel mass flux to local jet mass flux as a function of multiple geometric and flow parameters. This equation is useful when trying to understand the relative strength of the crossflow compared to the mass flux of the jet. It takes on a meaning similar to the inverse of the blowing ratio commonly seen in the film cooling literature. The equation takes the form of

$$\frac{G_c}{G_j} = \frac{1}{\sqrt{2} * C_d} * \frac{\sinh\left(\beta\left(\frac{x}{x_n} - \frac{1}{2}\right)\right)}{\cosh\left(\beta * \frac{x}{x_n}\right)} \quad (5)$$

The term C_d is the discharge coefficient calculated using the isentropic flow relations; the beta coefficient in the previous equations is provided by

$$\beta = \frac{\sqrt{2} * C_D * \frac{\pi}{4}}{\left(\frac{y}{d} * \frac{z}{d}\right)} \quad (6)$$

Other notable impingement array works were done by Liu et al. [20] where an array of jets impinging on a featured surface was studied with thermochromic liquid crystals. The features included ribs in the spanwise direction located directly underneath each row of jets in an inline pattern or in between two rows of jets in the staggered pattern. The work also studied ribs positioned along the streamwise direction directly beneath the jets for the inline case and in between jets in the staggered case. The authors found a decrement of heat transfer for the inline cases; they attribute it to the breakup and separation of the wall jet. The overall heat transfer was not dramatically altered by the ribs; even though the work did not delve into pressure loss, a safe assumption can be made that in the longitudinal rib case, a significant increase in pressure drop may counteract the little heat transfer enhancements the ribs provide. Professor Metzger [21] studied a single row of impingement holes with varying crossflow. The work shows that a decrease in lateral spacing, or Y/D , increases the heat transfer and the jets ability to counteract the crossflow; the authors point out that the negative effects of crossflow can easily be counteracted by decreasing the lateral spacing of the holes.

Typical jet length-to-diameter ratios, L/D , are kept below one in most impingement studies. San et al. [22] studied the effect of jet hole length on target wall heat transfer with varying Z/D , X/D and Y/D . They found that an increase in L/D amounted to a decrease in area averaged Nusselt number within the range of tested L/D 's of 5.5 and 166. On another article, San et al. [23] ran a study to find the optimum jet-to-jet spacing in order to maximize area averaged Nusselt number. The results shows optimum lateral jet spacings be a function of jet height. The work provides a correlation for stagnation region Nusselt number.

Work similar to the one done by Florschuetz et al. was done by Van Treuren et al. [24]. They studied impingement arrays at multiple Reynolds numbers and channel heights. The domain, like the one studied in this thesis is constrained on three sides. The authors provide a correlation for stagnation Nusselt number as a function of Reynolds number, mass flux ratios and geometric parameters. Chambers et al. [25] tested an inline and staggered impingement channel with the ability to add crossflow at the entrance of the channel. The study tested the effect of different amounts of initial crossflow on area average heat transfer. The results show that even with 10% of the total flow being put through the initial crossflow, the amount of heat transfer provided by the jets is diminished by a factor of two. Park et al. [26] studied the effects of Mach number and Reynolds number on an array of jets. The results show discharge coefficients varying with Mach number as well as Reynolds number. A correlation is given for the ratio of Nusselt number normalized by the Nusselt number provided using the Florschuetz et al. correlation [18] as a function of Mach number; the correlation takes the form of

$$\frac{\overline{Nu}}{\overline{Nu}_F} = 1 + 0.58Ma^{1.35} \quad (7)$$

A similar work done by Goodro et al. [27] provides a Nusselt number augmentation correlation

$$\frac{\overline{Nu}}{\overline{Nu}_F} = 1.1 + 1.2Ma^{2.3} \quad (8)$$

These correlations are useful when applying correlations developed using low Mach number experiments to high Mach number flows (typically encountered in turbine cooling applications)

Impingement Heat Transfer Reviews

One of the most well known accumulations of impingement research was done by Holger Martin [13]. In this compilation, non dimensional jet to target spacing was studied; they ranged from $Z/D=1/2-10$, providing plots of Sherwood number as a function of radius for four different jet to target spacings. The local Sherwood number was also given for a slot jet for H/S ranging from .5 to 20. Sherwood number is the mass transfer value analogous to Nusselt number. The relationship between Sherwood number and Nusselt number is given by

$$\frac{Nu}{Sh} = \left(\frac{Pr}{Sc}\right)^{0.42} \quad (9)$$

Studies on impingement jet arrays were also gathered alongside an array of slot jets. Correlations were given for multiple setups present in the paper. Circular jet arrays and slot arrays are studied in detail with both analytical and experimental approaches. The paper also combines studies done on swirling jets, turbulence enhancers on the target surface, impingement on concave surfaces and angle of attack variations. Optimization studies were also done to find the optimal spacing for round and slot jet arrays. Martin provides correlations for single round nozzles as well as single slot nozzles that are still commonly used today; the single round nozzle correlation takes the form

$$\frac{Nu_{SRN}}{Pr^{0.42}} = \frac{D}{r} \frac{1-1.1D/r}{1+0.1(Z/D-6)D/r} * \sqrt{4Re + \frac{Re^{1.55}}{50}} \quad (10)$$

The single slot nozzle correlation takes the form

$$\frac{Nu_{SSN}}{Pr^{0.42}} = \frac{1.53}{x/S+H/S+1.39} * Re^m; \quad m = 0.695 - \frac{1}{x/S+H/S^{1.33}+3.06} \quad (11)$$

Viskanta [14] is a paper similar to the one by Martin [13] with the inclusion of work done between 1977 and 1992; the study also incorporates the research done on flame jets typically used on the annealing of metals or in furnaces. The review includes impingement literature on

single round nozzle, single slot nozzle, a single row of round jets (similar to the one in this work disregarding side walls) a row of slot jets, angled impingement of round jets, impingement onto concave and convex surfaces by round jets, inline and staggered arrays of round jets similar to those found in Florschuetz et al. [19], a slot jet with crossflow and arrays of jets with different crossflow confinement techniques. More recently, Professor Weigand and Spring [15] published a review on multiple jet impingement with similar emphasis as the two aforementioned works. The paper also provides an overview of numerical work on impingement. The review takes a different route than the one taken by Martin [13] and Viskanta [14] by only surveying multiple round jet impingement, studying the flow features that affect the Nusselt number profiles and providing explanations for patterns seen in the distributions. A concise table obtaining a significant amount of correlations is also provided; in it are the Martin [13], Florschuetz [19], Park [26] and Goodro [27] correlations among many others. The Weigand impingement review [15] is an excellent starting point on which students can begin their impingement literature survey.

Other Impingement Literature

As stated previously, there are hundreds of articles that study heat transfer due to jet impingement; we have discussed some of the more relevant work previously; in the spirit of completeness, a brief introduction to different types of impingement are provided in this section. Cho et al.[28] studied experimentally and numerically coupled impingement-effusion on two geometries: one with the effusion hole being directly downstream of the impingement hole called “shifted array” and another with the effusion hole being staggered from the impingement hole called “staggered array”. Higher heat transfer coefficients are achieved by the staggered array.

Onstand et al. [29] studied a unique impingement array that featured a spent flow removal technique through the jet plate; the removal of the post-impingement spent flow minimized the negative effects of crossflow allowing for large and uniform heat transfer coefficients. Bunker and Metzger [30] and Metzger and Bunker [31] studied impingement on a concave surface with and without coolant extraction, respectively. Results show the dominant heat transfer is caused by the impingement flow; single round nozzles outperforming a single slot nozzle and, surprisingly, having the impinging jets be inline with the effusion holes caused heat transfer enhancements of up to 50%. Gillespie et al. [32] did similar work to the one done by Metzger and Bunker [31] with the impingement target wall being flat instead of curved. Contours of Nusselt number are provided and discussed. Deng et al. [33] studied impingement on a leading edge cavity with the effect of rotation and film extraction at multiple angles. The paper provides correlations for Nusselt number as a function of Reynolds number and rotation number at three bleed angles on three different internal surfaces. Following the work done by Bunker et al. [30] Fenot et al. [34] ran an experimental study on jets impinging on a concave wall mimicking a turbine leading edge. The paper provides a correlation for area averaged Nusselt number as a function of Reynolds number, Z/D and ratio of target wall diameter to jet diameter d/D .

Many researchers have studied impingement to featured surfaces; the consensus seems to be that features on the target wall break the wall jet causing separated flows near the wall effectively decreasing the Nusselt number. The only promising use of any kind of features on the target wall is by placing ribs in the streamwise direction between two rows of holes; in this setup, the flow does not separate and the rib acts as a fin increasing the wetted area.

Multiple works on featured impingement includes Yan et al. [35], [36] using ribs to enhance heat transfer on the target wall, Kanokjaruvijit et al. [37] using dimples, Rallabandi et al. [38] using ribs and porous foam, Ekkad et al. [39] using dimples on the target wall and Akella et al. [40] impinging on dimpled surfaces of a rotating channel.

Experimental Techniques

The publication most pertinent to the experimental technique used in this study is that of Liu, et al. [41] and Liu's dissertation [42]. In both works, the author details how temperature sensitive paint, TSP, and pressure sensitive paint, PSP, are utilized to investigate the heat transfer due to a single round jet impinging on a surface at different jet-to-target wall spacings. Liu described in detail the history of the development of TSP and PSP, their respective calibration procedures, and degradation due to time and other environmental factors. Further reading into the dissertation is encouraged as it contains data of the degradation of TSP and PSP as a function of luminosity, exposure time and other important factors. The dissertation also provides valuable lessons learned on the use of TSP. Again, the reader is strongly encouraged to review this piece of literature before conducting experiments with TSP to prevent costly mistakes.

It is assumed that simple fluid dynamics experimental techniques (pressure taps, total pressure and static pressure measurements) are part of a common knowledgebase of a fluids mechanics/heat transfer researcher. It is also assumed that the reader is familiar with simple electrical measurements used to gather heater voltages and currents

CHAPTER THREE: PURPOSE AND PROBLEM STATEMENT

As mentioned previously, one of the major roadblocks in the development of gas turbines with higher efficiency is being able to increase the turbine inlet temperature without sacrificing the longevity of the hot components. In order to increase the turbine inlet temperature, better super alloys and thermal barrier coatings have to be developed alongside better cooling technologies. The advantages that impingement channel cooling possesses provide a potential advancement of cooling technologies of the future. In order for heat transfer engineers to design the cooling system of certain hot component, he or she must consider the heat transfer generated by all wetted surfaces.

Only two investigations have studied and presented the Nusselt number profiles on the side walls of impingement channels. It is believed that the side walls provide a significant amount of cooling especially when the impingement channels are placed side to side as shown in Figure 3; the side walls of two adjacent channels behave as a fin, increasing the total heat transfer area. The current literature lacks side wall characterization at a large range of impingement heights. The purpose of this work is to characterize the Nusselt number distribution on the target and side walls of a narrow impingement channel at six different channel heights of $Z/D = 1, 2, 3, 5, 7,$ and 9 at five Reynolds numbers while keeping the lateral spacing constant at $Y_c/D=4$.

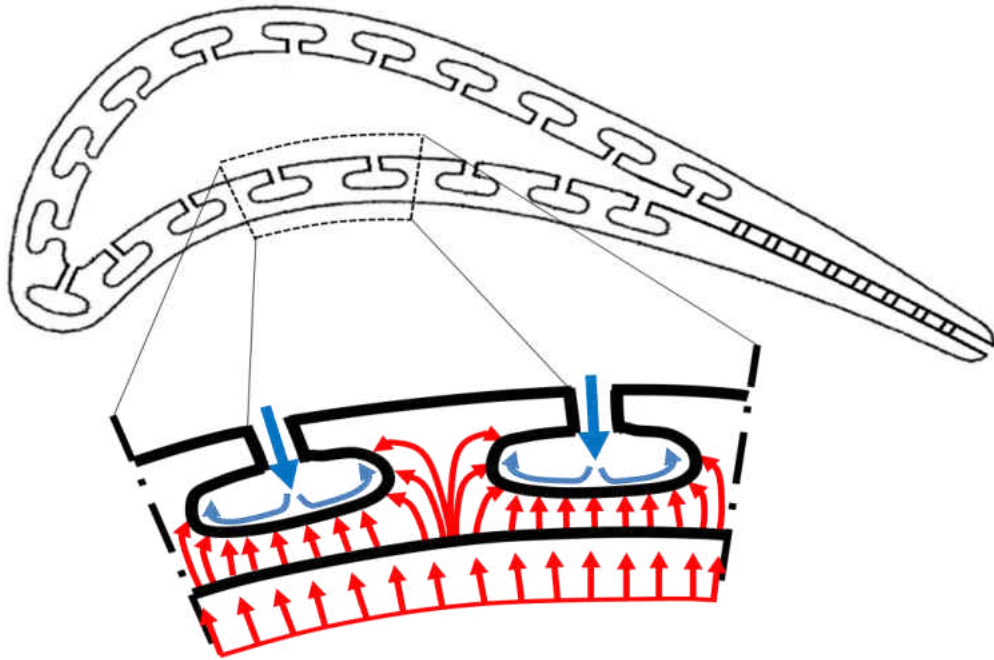


Figure 3: Turbine airfoil cooled with a series of impingement channel with heat paths showing importance of side wall heat transfer

CHAPTER FOUR: EXPERIMENTAL SETUP AND DATA REDUCTION

The channel consists of four walls enclosing the channel in the streamwise direction as shown in Figure 4. The top wall, called jet-issuing plate or jet plate, is made out of $\frac{3}{4}$ inch acrylic. It contains fifteen 7.5mm jets whose entrance is counter bored with a diameter of 22.5mm, or 3 jet diameters, in order for the thickness of the plate at the jet location to be exactly one jet diameter, $L/D=1$. Having a jet length of one diameter ensures a flat velocity profile and is commonly used in the literature. The side walls are also made out of $\frac{3}{4}$ " thick acrylic. One of the side walls contains 16 pressure probes in the between-jet regions that are used to gather pressure data throughout the channel. The opposite side wall is painted using the temperature sensitive paint and is the wall where heat transfer data is taken. Multiple side walls are used to generate the spacing between the jet plate and the target plate. The side walls are 20mm taller than the channel height as the jet plate and target plate have an offset of 10mm between the plane where the side walls are attached to and the plane the flow is in contact with. The interface between side wall and target or jet plate is sealed with single sided Teflon tape. The target plate is made out of $\frac{3}{4}$ " thick acrylic and is also painted with temperature sensitive paint. A removable end cap was placed at the origin of the channel, $x=0$. The end cap was removed and the holes were blocked from both the plenum side and the flow side for validation testing.

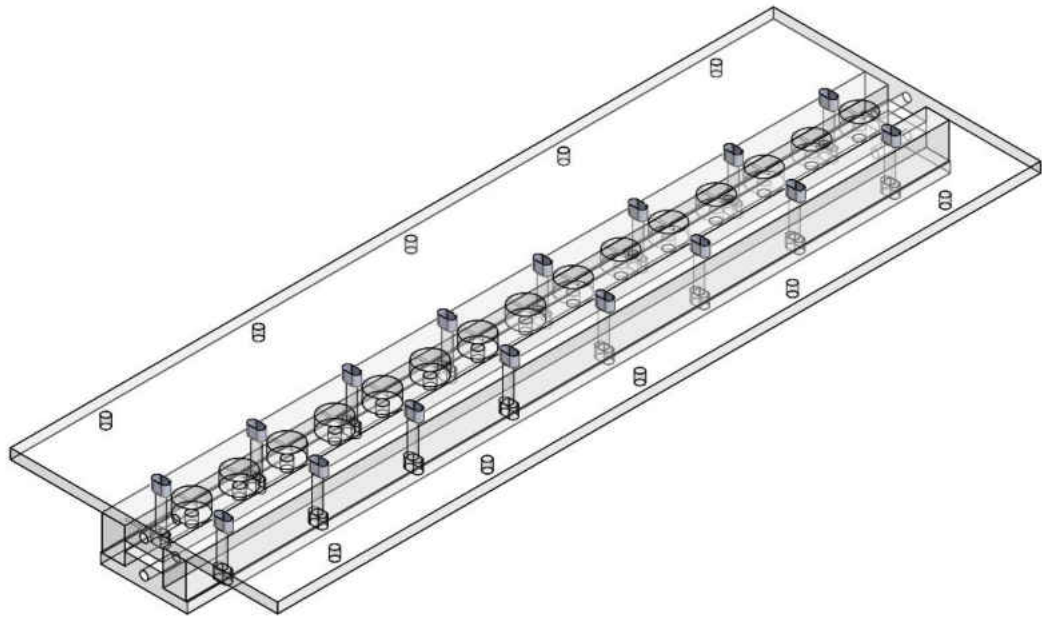


Figure 4: Isometric view of $Z/D=1$ impingement channel CAD

Six different channel heights were tested: $Z/D = 1, 2, 3, 5, 7, 9$; the streamwise jet spacing was of $X/D = 5$ and the spanwise distance was of $Y_c/D = 4$. The distance between the end cap and the first jet is of 5 diameters as is the distance between the last jet and the exit of the channel. A more detailed look of the geometry of the impingement channel is shown in Figure 5.

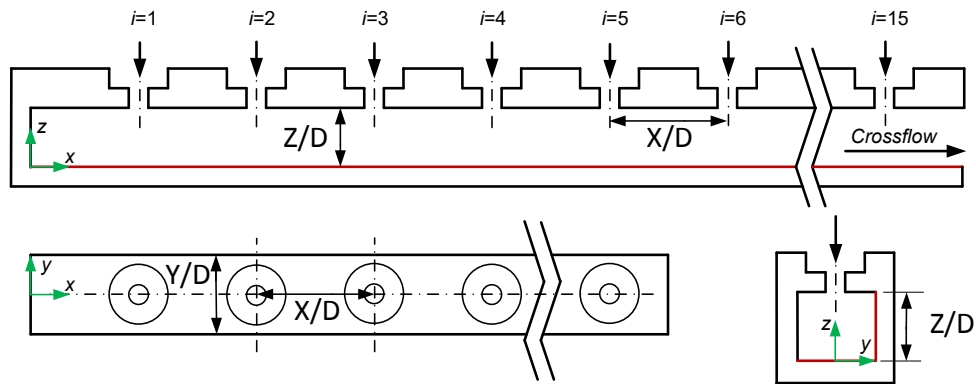


Figure 5: Impingement channel geometric parameters

An exit plenum is attached to the exit of the impingement channel which converts the rectangular cross-section of the channel to a circular cross-section where a 3” pipe is attached. As the flow moves downstream, it passes through a flow metering gate valve, a venturi flow meter and a secondary flow metering valve before combining with the bypass flow and heading into the blower where it is then pressurized and dumped into the atmosphere. The camera is attached on a beam approximately 1.6 meters beneath the test section. For the side wall, the camera setup was rotated 90 degrees along the streamwise axis so that the camera could have a clear view of the side wall. Since the acquisition of a second camera, two walls can be tested simultaneously decreasing the testing time by a factor of two.

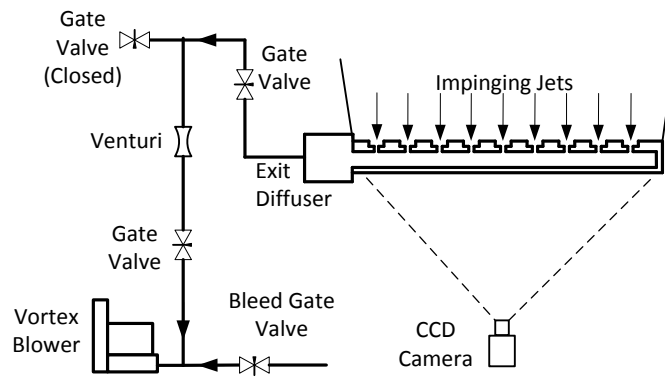


Figure 6: Impingement channel flow loop and camera setup

Target and side wall heat transfer data was gathered at five average jet Reynolds numbers. The Reynolds numbers ranged between 5,000 and 30,000; the maximum Reynolds number obtained on the $Z/D = 1$ channel was of 15,000 due to the large pressure drop in the channel. A comprehensive test matrix containing all geometric parameters and Reynolds numbers is shown in Table 2. A test matrix with actual Reynolds number is provided in the appendix.

Table 2: Test Matrix

X/D	Y/D	Z/D	Reynolds number
5	4	1	5,000
			7,500
			10,000
			12,500
			15,000
		2	10,000
			15,000
			20,000
			25,000
			30,000
		3	10,000
			15,000
			20,000
			25,000
			30,000
		5	10,000
			15,000
			20,000
			25,000
			30,000
		7	10,000
			15,000
			20,000
			25,000
			30,000
9	10,000		
	15,000		
	20,000		
	25,000		
	30,000		

Temperature sensitive paint, or TSP, is used to gather temperature data on the surface of the test section. The TSP is purchased from ISSI in 500 ml cans. The lab where the experiments were performed has a long history of TSP usage; hence, multiple calibrations exist. In order to ensure the use of the correct calibration a test piece was painted with the TSP can that is used to paint all side and target walls. The test piece was surrounded by ROHACELL isolative foam in order to ensure no lateral heat transfer. The painted test piece was attached to a copper block with the use of double sided Kapton tape. The copper block was attached to a thermoelectric heater with copper tape as well as heat sink thermal paste in order to reduce contact resistance. A computer heat sink was attached to the cold side of the thermoelectric heater in order to maximize heat transfer. A US sensor thermistor was embedded into the copper block covered with thermal paste in order to ensure proper contact and a correct temperature measurement. Figure 7 shows a diagram of the TSP calibration setup.

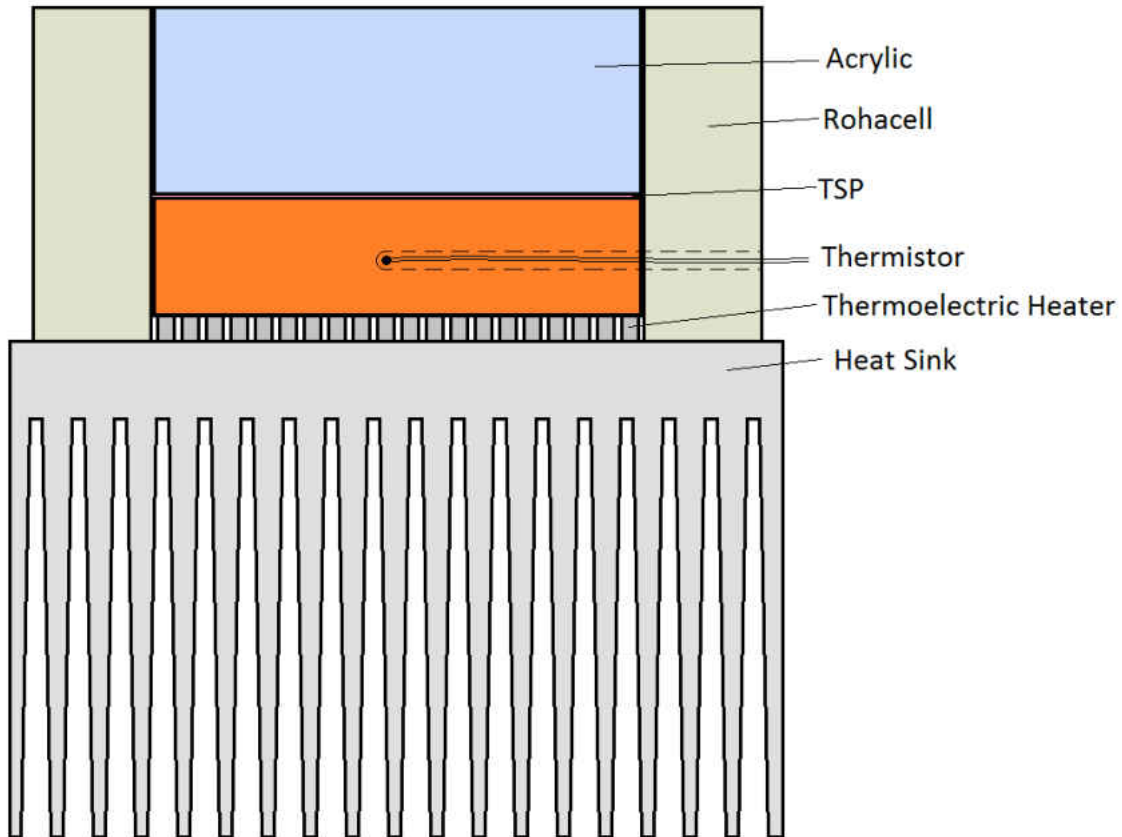


Figure 7: Temperature sensitive paint calibration setup

Calibration was done at multiple temperatures; thirty images were taken and averaged alongside their respective thermistor resistance measurement. Only the center region of the TSP was used to collect the area averaged intensity of each image set. Thermistor resistances were converted into temperatures with the use of the correlations provided by the manufacturer. Image intensity ratios are then plotted versus temperature ratios and a third order polynomial curve was fitted to the data. Figure 8 shows the strong agreement between the current calibration and the legacy calibration used in the codes. The small deviation between all calibrations provides a sense of robustness of the TSP as its calibration varies very slightly with time.

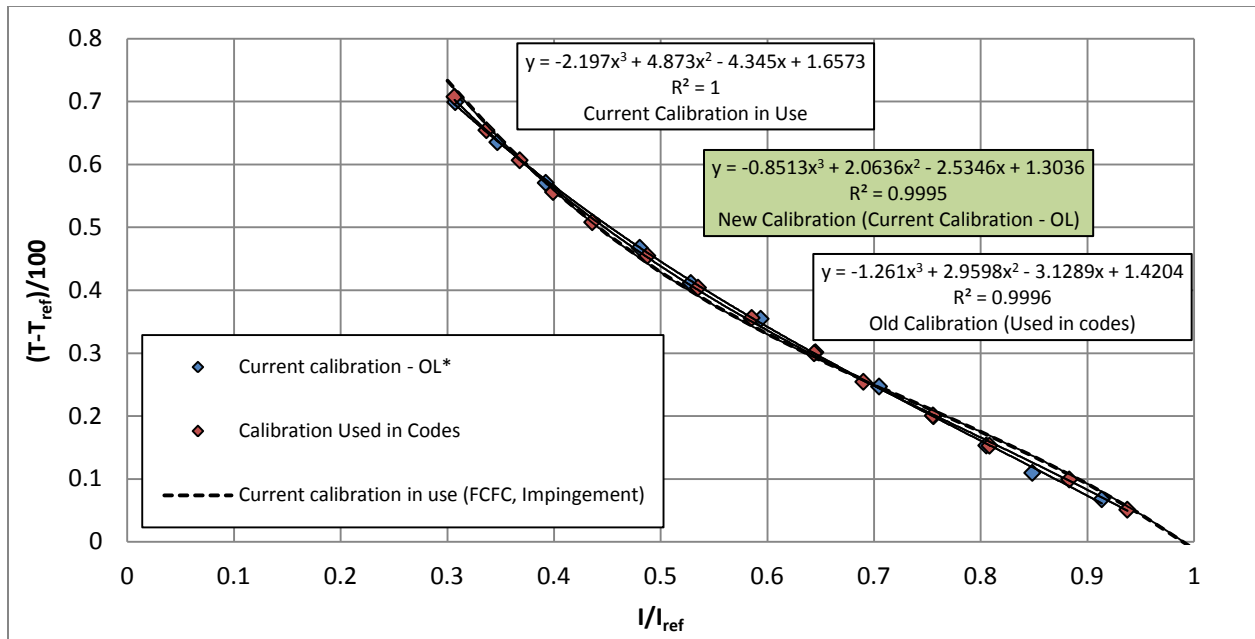


Figure 8: Temperature sensitive paint calibration results and comparisons with older correlations

It is important to note that direct comparison between the different calibrations is not advised since they were taken at different reference temperatures. If the profiles were linear, the comparisons could be made; however, they are most certainly not linear. Reference temperature differences have a stretching effect on the y axis. The current calibration in use is not the final correlation. The backwards calculation to go from reference temperature of calibration to reference temperature of the actual test has not been taken.

Walls where heat transfer data is to be taken are painted with TSP and cured on an oven at 353K for 20-30 minutes. Heater foils are cut out of .002” (5.08E-5m) thick stainless steel type 321 tool wrap foil. Double sided Kapton tape is attached to the foil heaters; the steel-Kapton foil is then attached to the cool painted surface. The painted acrylic should be cool before the heater

is attached in order to ensure little mismatch due to thermal expansion. Figure 9 shows a layered diagram with their respective thickness; the foil is in direct contact with the flow.

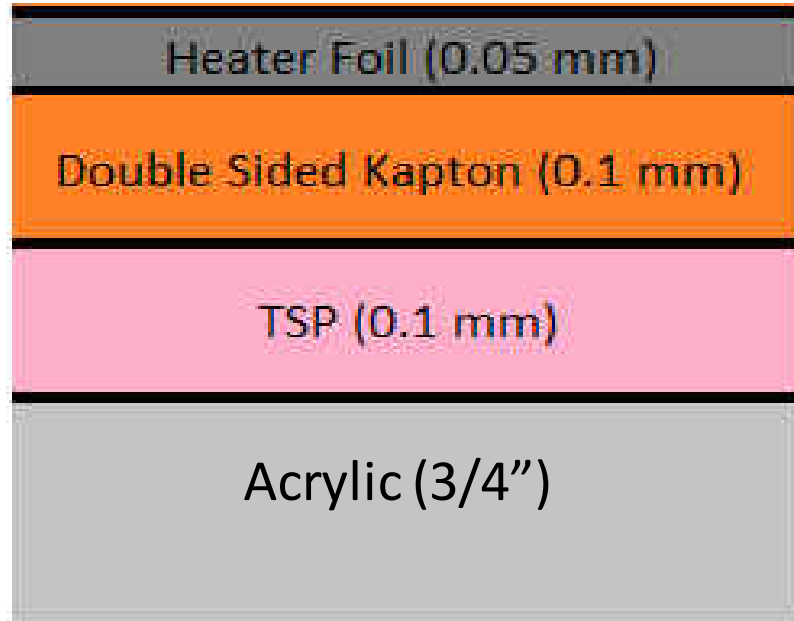


Figure 9: 1D diagram of test section layers (not drawn to scale)

Copper tape is used to make leads to the heaters in the test section. Copper wire is soldered to the copper leads and is then connected to the power supply. Two 12 Volt, 30 Amp DC power supplies were used to power the heaters. The current readout of the power supply is used as the current measurement.

Data Reduction

In order to determine the heat transfer coefficient, the electrical current (i) and heater resistance (R) are converted into an input heat flux (q_{gen}''). This is shown in Equation 12, where A_s represents the surface area of the heater exposed to the mainstream flow.

$$q_{gen}'' = \frac{i^2 R}{A_s} \quad (12)$$

The heater resistance is calculated using the resistivity (ρ_{el}) of stainless steel and the dimensions of the heater. The length (l) is measured in the stream direction, x , while the width (w) is measured in the span direction, y . The thickness (t) is the thickness of the stainless steel foil, measured in the wall normal direction, z .

$$R = \frac{\rho_{el} l}{wt} \quad (13)$$

Since the material that the heater is attached to, acrylic, is not a perfect insulator, some heat is lost through it. A simple one dimensional conduction model, shown in Figure 10, is used to estimate the amount of heat lost through it. The driving temperature is the temperature of the heater which is assumed to be constant throughout its thickness as Biot number was calculated to be $7.62E-4$; the author realizes that calculating a Biot number of the heater while it is generating heat is misleading (as by definition, the temperature profile is *not* constant, rather parabolic in shape, due to heat generation [43]), the miniscule value of the Biot number provides a reasonable inference that the temperature is constant inside the heater foil.

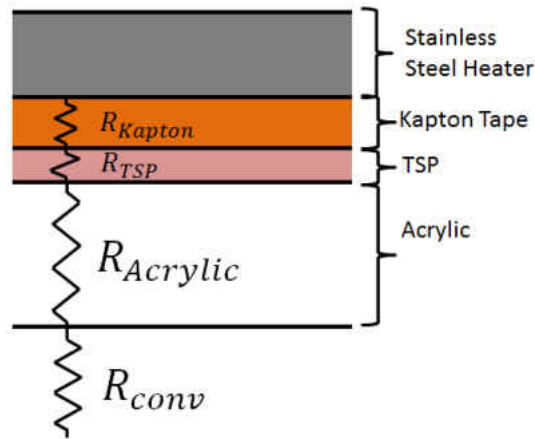


Figure 10: Conduction Loss Diagram

$$q''_{cond} = 12.98[T_w(x, z) - T_\infty] \quad (14)$$

The analytical model lacks the contact resistances between the interfaces of the Kapton, TSP and the heaters; the model also assumes constant properties of the materials as a function of temperature as well as the estimation of the backside heat transfer coefficient; due to all these inaccuracies, a heat loss test was setup on the actual test section to more accurately gauge the backside heat loss. The channel was filled with fiberglass insulation to ensure all the heat was lost through the acrylic. Four points were taken at different temperature ranges. The resulting curve is shown in Figure 11

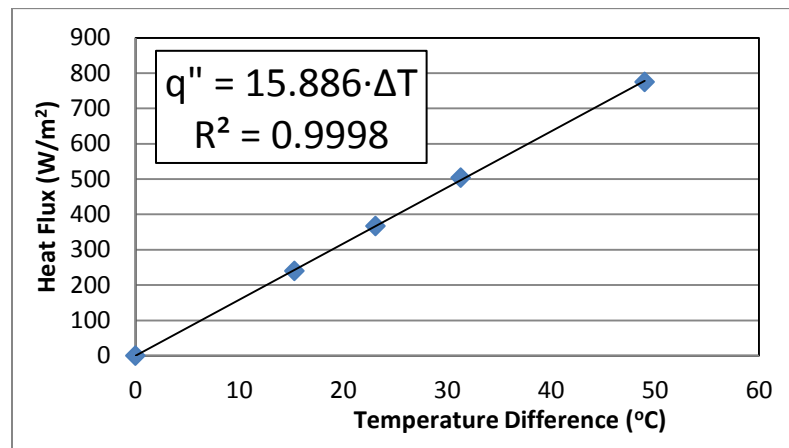


Figure 11: Heat loss results and correlation

The corresponding heat loss equation then varies slightly to become:

$$q''_{cond} = 15.89[T_w(x, z) - T_\infty] \quad (15)$$

Normal test heat fluxes ranged between 11,000 and 4,000 W/m² with area averaged temperature difference between the TSP and the atmosphere at 35 and 30 K respectively; therefore, typical heat loss was near 5% of the heat generated. Since there is higher fidelity on the correlation acquired by running the heat loss test, it will be used instead of the analytical model to calculate the heat transfer.

Pressure measurements were taken from the taps installed on the side wall of the channel with a handheld manometer. The pressure taps were located in between jet rows. Figure 12 shows a sample of the pressure profile acquired from the test. Each point is an average of a set of 30 measurements.

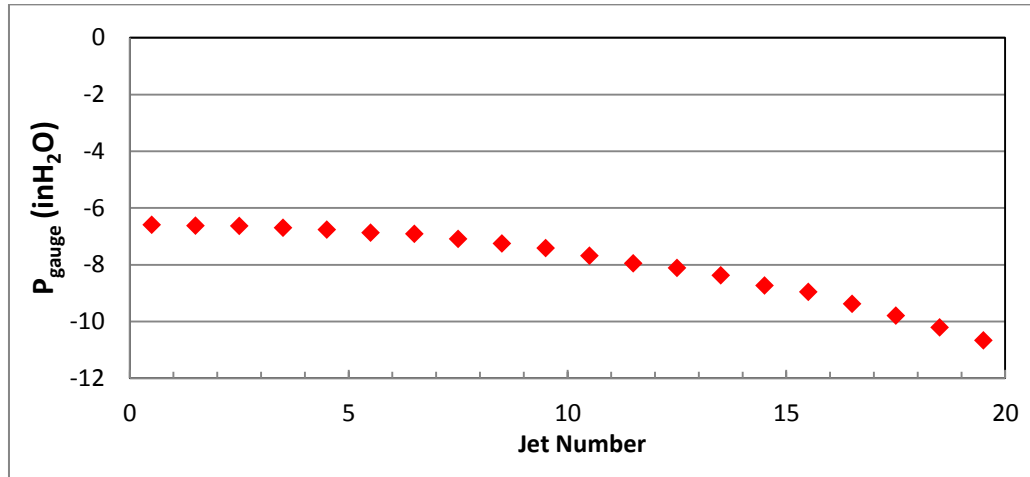


Figure 12: Sample Pressure Profile

This pressure data was then converted into absolute pressure in Pascals. The pressure ratio across the jet plate was then calculated, followed by the Mach number. The highest jet Mach number was calculated to be 0.19 at a pressure ratio of 1.027. Since the highest Mach number doesn't exceed 0.3, the flow is in the incompressible range. The jet velocity was then calculated using:

$$P_{absolute} [Pa] = P_{Gauge} [inH_2O] \cdot 249.08 \left[\frac{Pa}{inH_2O} \right] + P_{ATM} [Pa] \quad (16)$$

$$U_n = \sqrt{\frac{2 \cdot (P_{Plen} - P_n)}{\rho}} \quad (17)$$

Each individual jet velocity was then multiplied by the array-average discharge coefficient, C_d , to acquire an actual jet velocity. The jet mass flux ratio was then obtained using.

$$\frac{G_j}{G_{javg}} = \frac{\rho \cdot U_n}{\frac{\rho}{N_x} \sum_{n=1}^{N_x} U_n} \quad (18)$$

Channel mass flux was calculated using equation 19; equation 20 was used to calculate channel to jet mass flux ratio.

$$G_{cn} = \frac{\pi}{4 \left(\frac{Y}{d}\right) \left(\frac{Z}{d}\right)} \rho \sum_{n=1}^{N_x} U_n \quad (19)$$

$$\frac{G_c}{G_j} \Big|_n = \frac{\rho \cdot U_n}{\frac{\pi/4}{\left(\frac{Y}{d}\right) \left(\frac{Z}{d}\right)} \rho \sum_{n=1}^{N_x} U_n} \quad (20)$$

The calculated mass flux ratios are compared with the analytical model provided by Florschuetz; Local jet mass flux to average jet mass flux ratio is given by:

$$\frac{G_j}{G_{javg}} = \frac{\beta \cdot N_c \cosh \beta^{x/X}}{\sinh \beta^{x/X}} \quad (21)$$

Crossflow-to-jet mass flux ratio is given by:

$$\frac{G_c}{G_j} = \frac{1}{\sqrt{2} C_D} \frac{\sinh \beta^{(x/X)^{-1/2}}}{\cosh \beta^{(x/X)}} \quad (22)$$

where β is given by:

$$\beta = \frac{C_D \sqrt{2} \pi / 4}{\left[\left(\frac{Y}{d}\right) \left(\frac{Z}{d}\right)\right]} \quad (23)$$

Lateral Conduction Estimation

Lateral conduction through the heater is believed to be significant due to the nature of the heat transfer profiles. Large temperature gradients are encountered at low x/D between the cool stagnation region of the jet and the hot region between impinging jets. One dimensional lateral conduction calculations were done on the steel heater; the Kapton tape, paint and acrylic were omitted due to their thermal conductivities being an order of magnitude smaller than that of the steel; this assumption, as shown further ahead, is proven to be valid for all heat transfer profiles shown in this study. In order to do the calculation, the Nusselt number profile with the highest spatial Nusselt number inequality was used. Several profiles were tested to find the one with the highest Nusselt number gradient; $Z/D=2$ target wall heat transfer profile at $Re_{j,avg}=30,000$ was found to have the largest temperature gradient. A two dimensional conduction model was used to calculate the heat flux in the lateral direction through the steel foil compared to the heat flux in the wall normal direction driven by convection.

Figure 13 shows the results of the calculations; the blue dotted line shows the net lateral heat flux through the steel foil. The slope is seen to reach zero at the peak of Nusselt number due to the gradient being zero; as x moves away from the peak, the lateral conduction increases in magnitude. The red curve shows the wall normal heat flux. It is seen that the lateral conduction is two orders of magnitude less important than the wall normal heat flux. More importantly, the variation in wall normal heat flux is seen to be very monotonous throughout the stagnation region, reassuring the assumption of constant flux throughout the domain. A complete set of calculations can be found on the appendix

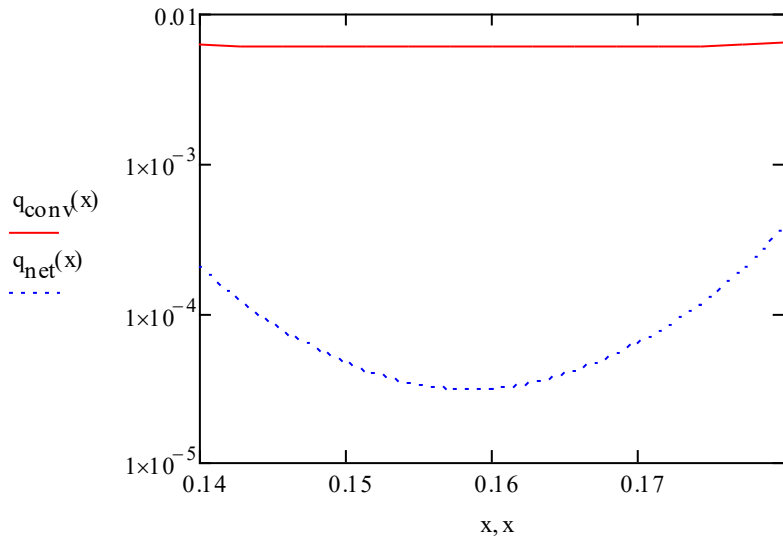


Figure 13: Lateral Conduction Estimates

CHAPTER FIVE: EXPERIMENTAL UNCERTAINTY

Experimental uncertainties were quantified using the methods described in Figliola and Beasley [44]. Five runs were setup using the $Z/D=3$ channel testing target wall heat transfer to quantify the precision uncertainty of Nusselt number as well as Reynolds number. The bias error for each measurand was gauged by reading the manuals of the respective instruments.

A table showing absolute uncertainties for Nusselt and Reynolds number are shown below in Table 3 and Table 4, respectively. The measurands for Nusselt number are the current, electrical resistivity of the steel, width and thickness of the heater, reference and test intensity, jet diameter as well as plenum and reference temperatures. The measurands for Reynolds number are the static pressure at the Venturi, atmospheric pressure, Venturi temperature, Delta pressure in the Venturi and jet diameter.

Table 3: Absolute and Relative Nusselt Number Uncertainties

Nusselt Number Uncertainty		
Measurand	Bias	Precision
Current	5.263	0.904
Electrical Resistivity	0.513	0
Width of Heater	0.125	0.293
Thickness of Heater	0.185	0
Intensity	0.015	5
Reference Intensity	0.011	9.789
Plenum Temperature	3.257	1.647
Reference Temperature	3.257	1.044
Hole Diameter	0.239	0.379
Individual Totals	7.02	11.21
Total Uncertainty	13.23	
Relative Uncertainty	18.90%	

Table 4: Absolute and Relative Reynolds Number Uncertainties

Reynolds Number Uncertainty		
Measurand	Bias	Precision
Venturi Static Pressure	57.904	1.206
Atmospheric Pressure	0.56	15.123
Venturi Temperature	36.484	10.426
Delta Pressure	2532	210.288
Diameter	79.689	6.00E-12
Individual Totals	2534.18	211.09
Total Uncertainty	2542.95	
Relative Uncertainty	10.91%	

In order to facilitate the understanding of the major sources of uncertainty, the bias and precision absolute uncertainties are plotted for both Nusselt and Reynolds number. They are shown in Figure 14 and Figure 15, respectively.

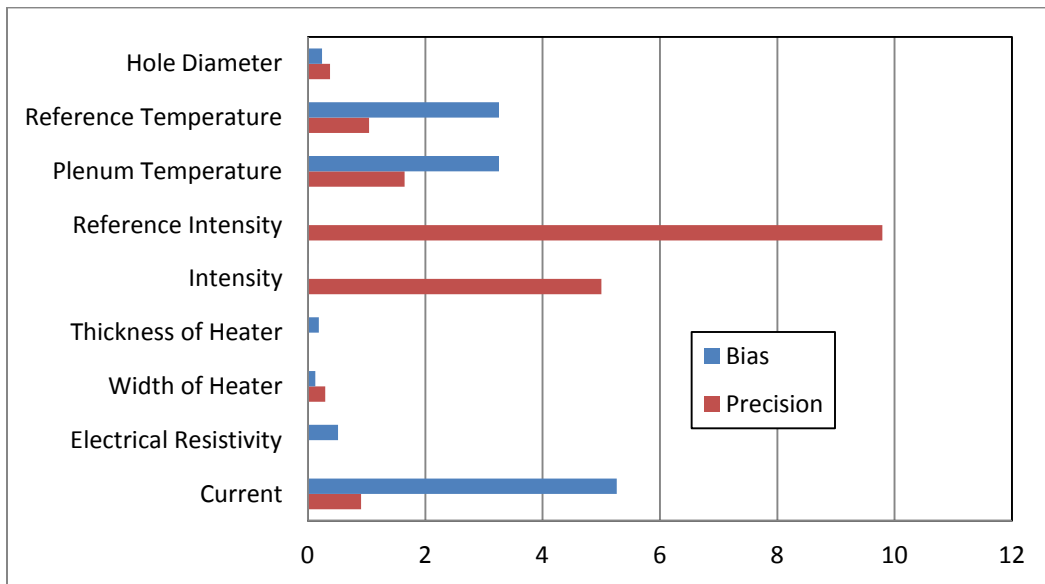


Figure 14: Absolute Uncertainties of Nusselt Number

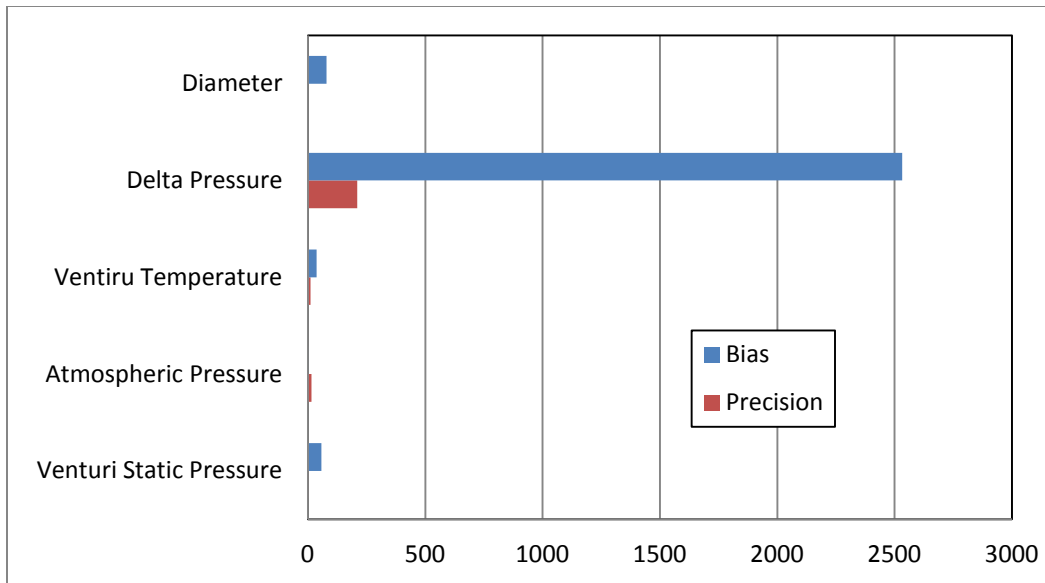


Figure 15: Absolute Uncertainties of Reynolds Number

The largest source of uncertainty for the Nusselt number comes from the precision in intensities due to the repeated use of the same paint in all the precision runs. Electrical current plays a major role in the bias followed by the reference and plenum temperatures; acquiring better instrumentation for the temperature measurements would be advisable since it provides large drops in uncertainty with little cost. The precision uncertainty for the Reynolds number is almost non-existent. The largest source of uncertainty for Reynolds number is the DP measurement across the Venturi. Using multiple manometers to measure pressures in their optimum range would be advisable in the future. Two different manometers were used for these experiments; the worst of the two was used for the bias uncertainty.

CHAPTER SIX: FLOW RESULTS

Using the aforementioned equations, mass flux ratio distributions were calculated and compared with the analytical models provided by Florschuetz, et al. [19] Channel mass flux to jet mass flux ratio distribution and their comparisons to the analytical models are shown in Figure 16. The model and local data match at large channel heights; however, as the channels get smaller, friction causes a significant pressure drop as a function of streamwise distance causing the model and experimental data to deviate. Exit effects may also cause misleading pressure measurements on the downstream-most pressure tap.

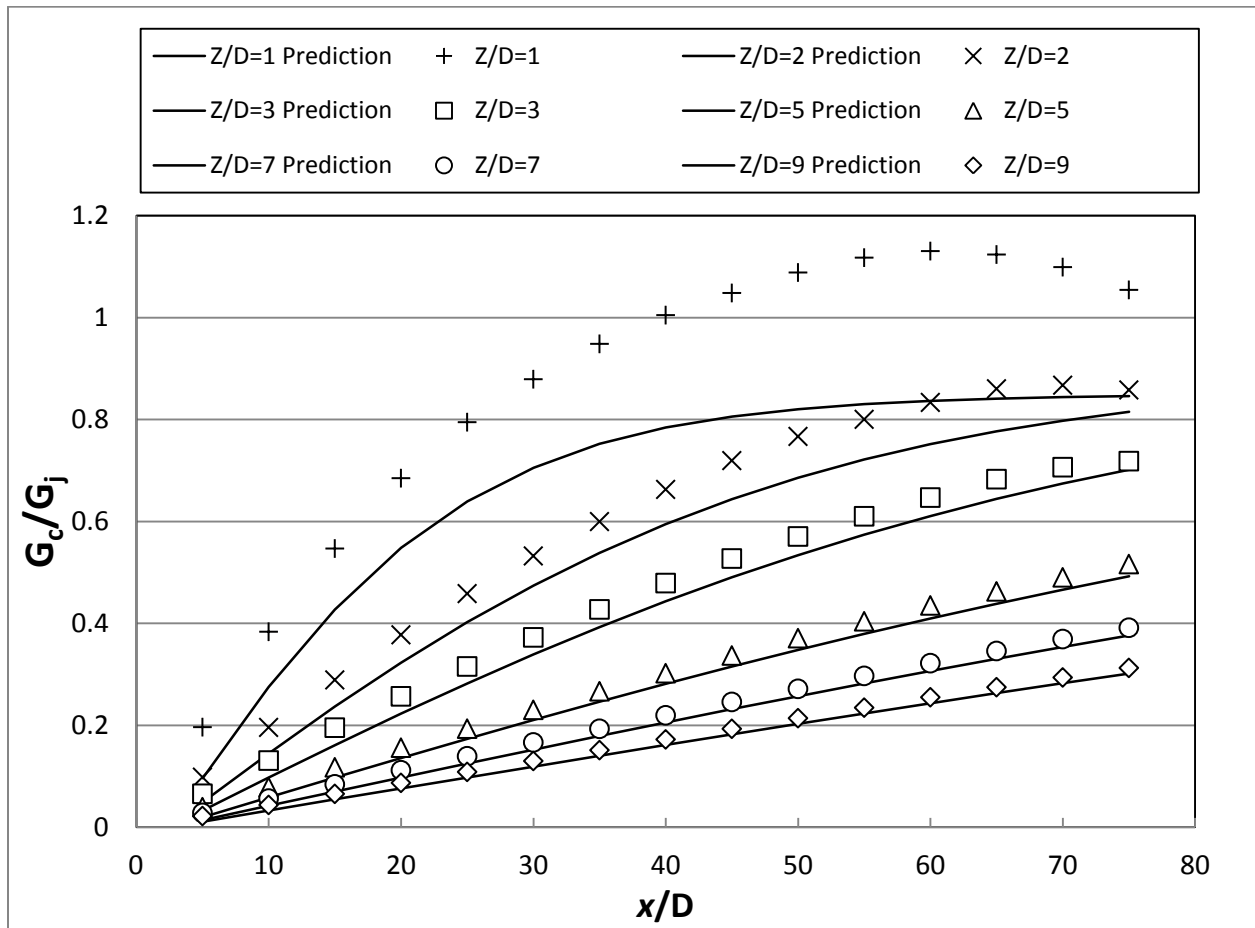


Figure 16: Channel mass flux to jet mass flux ratio distribution

Local jet mass flux to average jet mass flux is also calculated and compared to the analytical model; the results are shown in Figure 17. The mass flux ratio indicate the deviation of the local jet Reynolds number from the average jet Reynolds number; that is, for the $Z/D = 1$ case, the first jet approximately has a Reynolds number 65% lower than the average jet Reynolds number. The variation in local jet Reynolds number is large for low impingement heights with the local jet Reynolds number varying by an order of magnitude between the first and last jet. As the channel height increases, the jet Reynolds number profile flattens as the pressure drop in the larger channels is smaller than the one on the smaller channels. As previously described, large pressure drop inside the channels with small impingement height is believed to be the source of discrepancy between the analytical model and the experimental data.

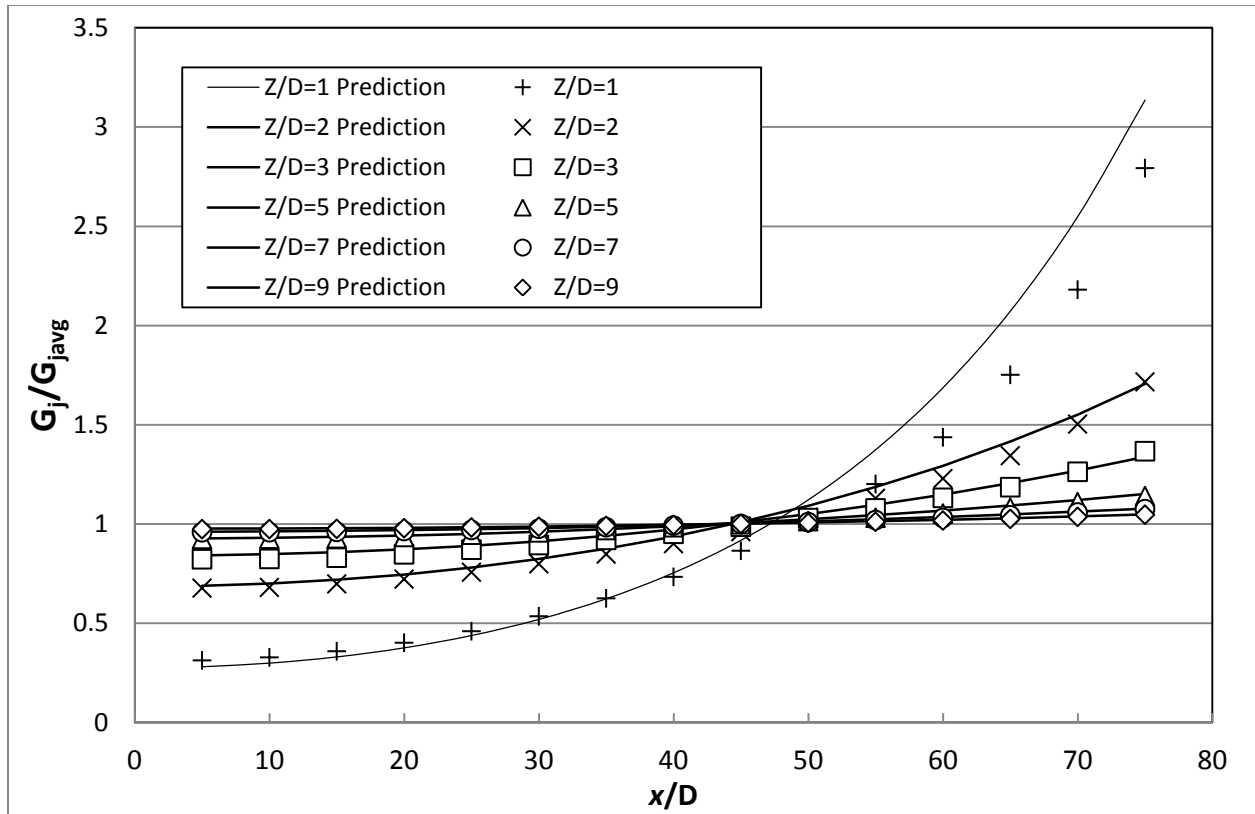


Figure 17: Local jet mass flux to average jet mass flux ratio and comparisons to analytical models

CHAPTER SEVEN: HEAT TRANSFER RESULTS

Smooth Channel Validation

Heat transfer data was collected on two walls of the impingement channel as explained previously. A validation run used to compare the results of the current test setup with heat transfer results that are widely known was done. The $Z/D = 3$ channel was setup by blocking all the hole exits on the flow side of the jet play with clear smooth packing tape. On the plenum side, the jet plate was sealed with aluminum tape to ensure no leakage flow through the 15 jets. The front end cap was removed; a trip wire was placed near the target wall to trip the flow in order for it to develop faster. The data was gathered using the target wall at two Reynolds numbers based off of hydraulic diameter of the channel. The length of the channel was close to 22 hydraulic diameters ensuring a fully developed hydrodynamic and thermal boundary layer. The span averages of the validation runs are shown in Figure 18. The profiles are normalized by their corresponding Dittus-Boelter correlation [43]. The Nusselt number profile starts high when both hydrodynamic and thermal boundary layers are developing. As the streamwise distance decreases, both profiles are seen to converge near unity signifying a successful validation of the channel with respect to the well-accepted Dittus-Boelter correlation. A validation attempt using the $Z/D=1$ channel was done with the results matching well in the area averaged basis; however, due to the $Z/D=1$ channel having an aspect ratio of 4, the local profiles exhibited local non uniformities at the entrance of the channel possibly due to secondary flows. It was then decided to validate with a channel with an aspect ratio as close as possible to 1 which lead to the choosing of the $Z/D=3$ channel.

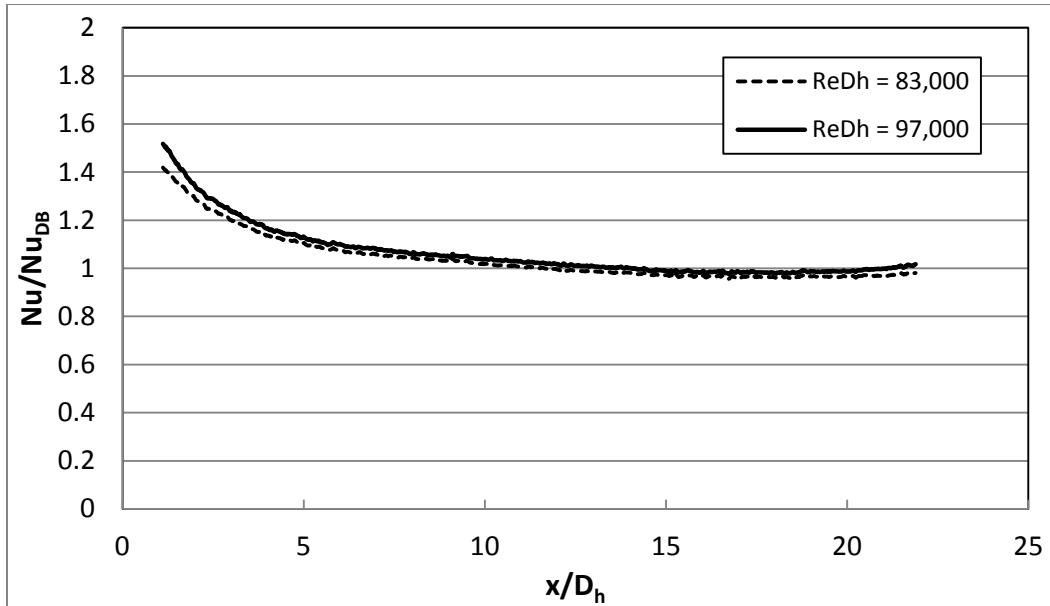


Figure 18: Smooth Channel Validation

Heat Transfer Results

Now with the experimental setup validated, results for the target wall and side walls are shown for some Reynolds numbers and all channel heights. The heat transfer profiles of all walls and channels at all Reynolds numbers are shown in the appendix; for the sake of brevity, only comparisons are shown and described in this chapter. Figure 20 and Figure 20 show the target wall Nusselt number profiles at average jet Reynolds number of 10,000 and 15,000 respectively. The $Z/D=1$ profile features increasing heat transfer as a function of streamwise distance, x . Local maxima are seen directly underneath the jets generated due to the jet impinging on the surface. The Nusselt number profile for the $Z/D = 2$ channel exhibits the most uniform heat transfer outline out of all channels; although maxima due to jet impingement are visible, the Nusselt number does not seem to be a function of the streamwise location. As channel heights increase, the stagnation region Nusselt number decreases for the first few jets and quickly decreases as a

function of streamwise distance. One feature seen in the target wall profiles for both Reynolds number is the dominance of the second – and sometimes the third – jet over the first one. The Florschuetz et al. correlation does not predict this behavior. It may be caused by transient effects where the crossflow from the first jet may be shedding vortices that affect the behavior of the downstream jets by forcing them to deflect from their centerline in a periodic fashion allowing it to cool a larger area. It would be advisable to run a URANS simulation of the first 5 jets to see if there are transient flow fields caused by the upstream jet.

The downstream shift of the jets due to crossflow is seen in the local target wall profiles. The $Z/D = 2$ channel only contains 14 distinct peaks visible implying that the 15th jet has been deflected by the crossflow downstream by at least 3 diameters; this downstream shift is expected as the mass flux ratio between the channel and the jet reaches a value near $G_c/G_j=0.8$ which implies the crossflow is coming in with a velocity close to the velocity of the jet. The equivalent blowing ratio analogy is that the jet has a blowing ratio of $M=1.25$ which, as seen in the film cooling literature allows for the jet to liftoff from the surface but is quickly deflected downstream.

The shapes of the Nusselt number distribution caused by the first jet is circular of $Z/D= 2, 3, 5, 7,$ and 9 . As crossflow builds up, the jets start being deflected downstream causing their shapes to morph into a parabolic shape that is sharp at the centerline and blunt on the sides. The change of shape is due to the wall jet of the upstream jet moving downstream creating an up wash similar to a hydraulic jump; the upstream wall jet moves above the local wall jet generating the detrimental crossflow. Local minima and maxima are not visible far downstream of the $Z/D = 7$ and 9 channels due to the jets not having enough momentum to reach the target wall; it is presumed that the heat transfer in this regions is dominated by the crossflow.

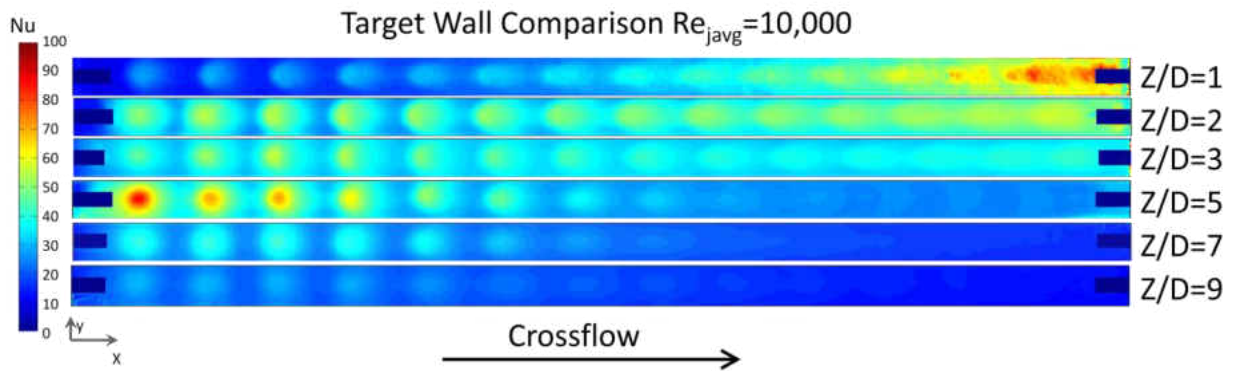


Figure 19: Target Wall Comparison at $Re_{javg}=10,000$

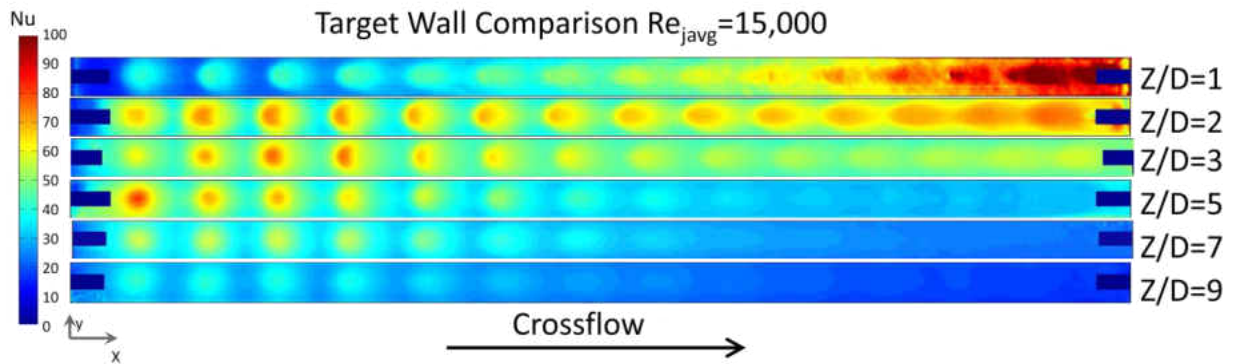


Figure 20: Target Wall Comparison at $Re_{javg}=15,000$

Side wall Nusselt number contours are shown in Figure 21 and Figure 22 for $Re_{javg} = 10,000$ and $Re_{javg} = 15,000$ respectively. The stagnation regions of the wall jets are visible at low z/D . Similarly to its respective target wall heat transfer profile, the $Z/D=1$ side wall Nusselt number profile shows increasing Nusselt number as a function of streamwise distance. The side wall profiles show less distinct maxima than their respective target wall; this may be attributed to the fact that the wall jets have to travel a distance of two diameters in either direction before impinging on the side wall. As stated previously, the shapes of the Nusselt number profiles changes as a function of streamwise location and channel height; the deflection of the wall jet

downstream prevents it from reaching the side wall. For the $Z/D = 2$ channel, as streamwise distance increases, the Nusselt number is also seen to increase maintaining the trend seen in the $Z/D = 2$ target wall of it having the most uniform Nusselt number profile.

One notable difference in side wall Nusselt number profile as a function of channel heights comes from the deflection of the jets downstream with increased crossflow; as stated previously, the downstream deflection in Nusselt number maxima can be seen having a greater effect on the side wall than on the target wall profiles. At low channel heights, the local maxima occurs at low z/D (near the target wall). The trend holds accurate for the first 4 or 5 jets at all channel heights. The peak starts shifting to a higher z/D for the tall channels, $Z/D = 5, 7$ and 9 . The shift of the maxima to locations away from the target wall is due to the crossflow not allowing the jet to reach the target wall; instead, the jet gets deflected downstream diffusing, and possibly wobbling from side to side due to vortex shedding of the upstream jets causing it to only alter the side wall heat transfer; the maxima are seen at an $x/D=3.5$ for the $Z/D = 7$ channel and at an $x/D=4.5$ for the $Z/D = 9$

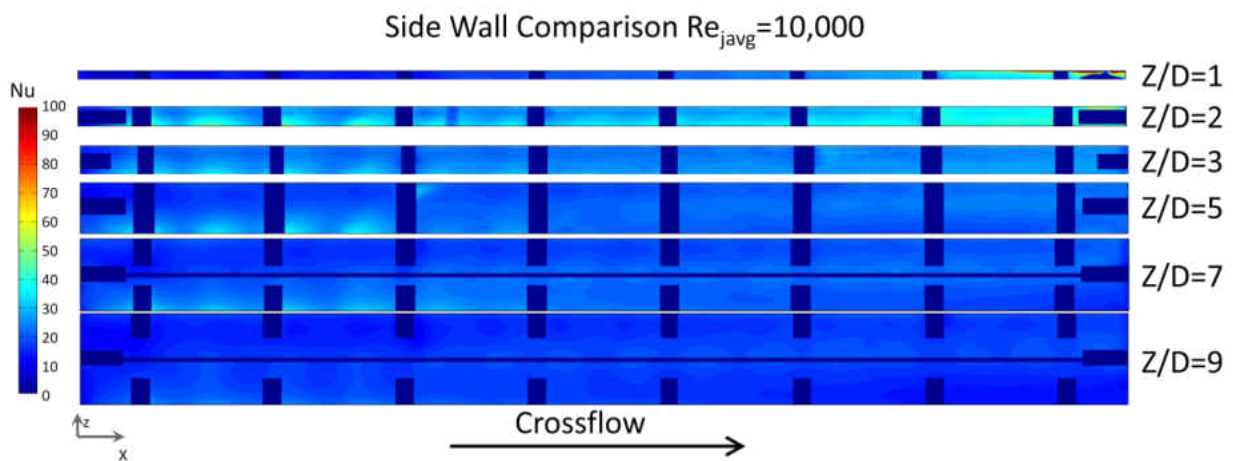


Figure 21: Side Wall Comparison at $Re_{javg}=10,000$

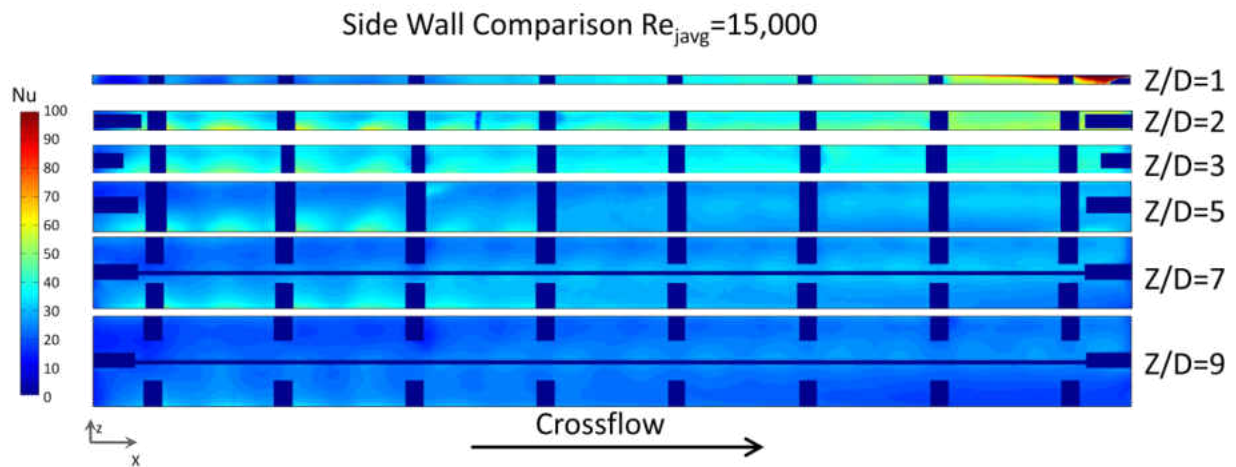


Figure 22: Side Wall Comparison at $Re_{javg}=15,000$

In order to better understand the heat transfer profiles, laterally averaged plots of Nusselt number are shown only for $Re_{javg} = 15,000$ in Figure 23 for all target walls and Figure 24 for all side walls. Demonstrating the points made previously, the $Z/D=1$ profile is seen to increase as a function of streamwise location, the $Z/D=2$ lateral average confirms the fact that it, alongside the $Z/D=3$ channel, is very uniform in the streamwise direction. The profiles of the $Z/D= 5, 7$ and 9 channels seem to decrease monotonically as a function of the channel height. Comparisons between the target and side walls show the difference in downstream shift of peaks in Nusselt number. From a systems point of view, the area averaged Nusselt number does not vary significantly for any channel height; however, the $Z/D = 2$ and 3 channel seem to provide the highest cooling capability at a relatively low (compared to $Z/D = 1$) pressure loss.

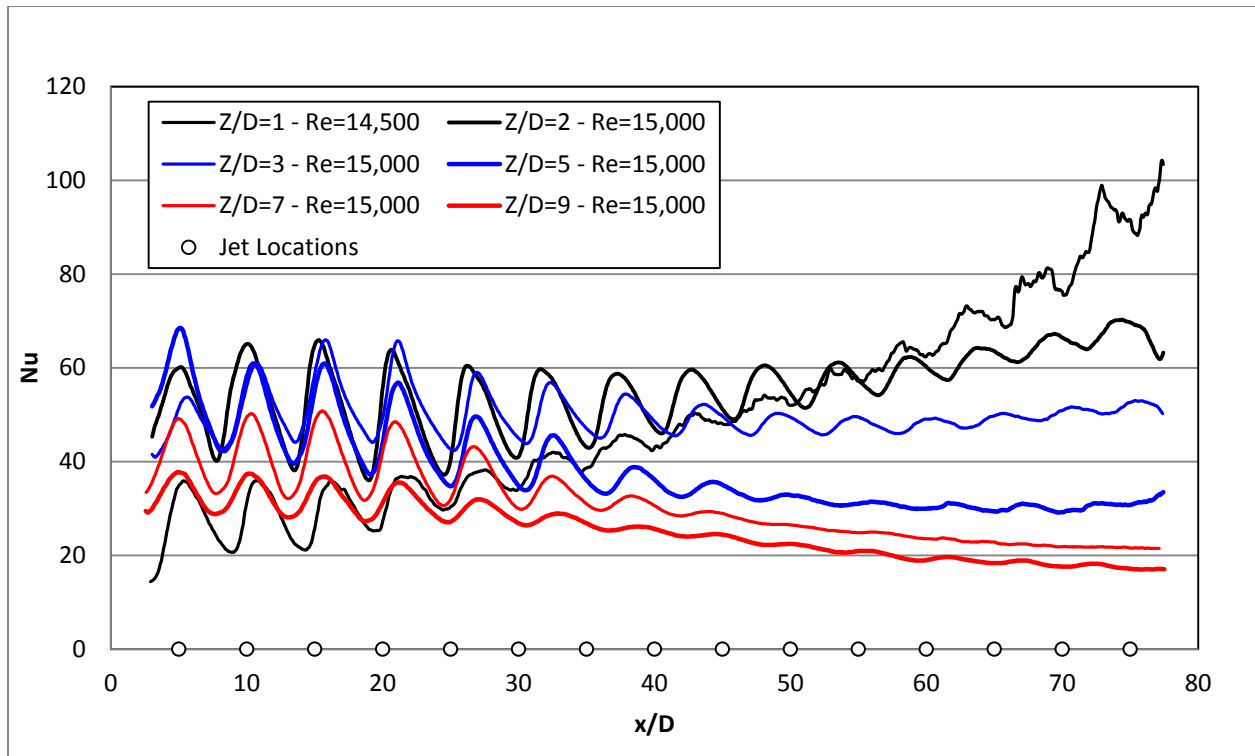


Figure 23: Target Wall Nusselt number Comparisons at $Re_{javg}=15,000$

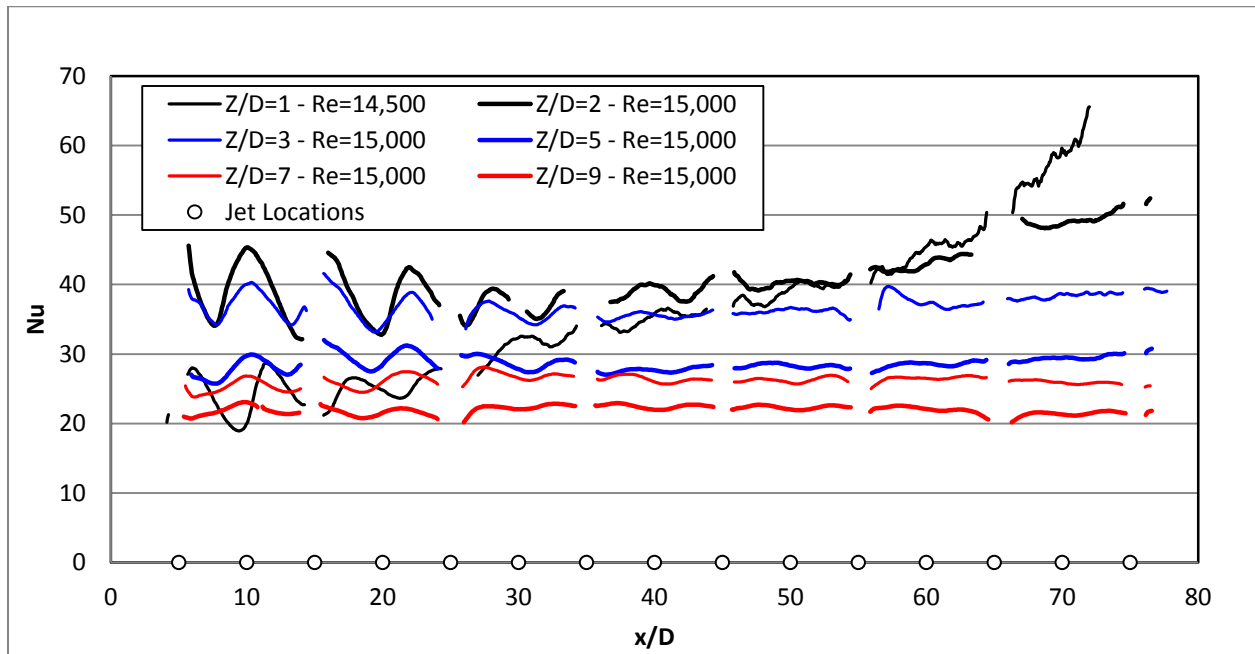


Figure 24: Side Wall Nusselt number Comparisons at $Re_{javg}=15,000$

One of the major focuses of this project is to understand the interaction between the target and side wall heat transfer profiles. Isometric views were generated by placing the side wall Nusselt number profiles in the vertical position and the target wall profiles in the horizontal position for all channel heights; due to the target and side walls being run at the same time, the corresponding Reynolds numbers are identical for both walls shown at a single channel height.

The isometric view of $Re_{javg} = 10,000$ is shown in Figure 25 while the one for $Re_{javg} = 15,000$ is shown in Figure 26. The profiles seen here are identical to the ones seen in figures Figure 206, Figure 20, Figure 21, and Figure 22 rearranged in order to get a better feel of the interaction between the two walls.

At low impingement height, the high Nusselt number regions of the side wall are seen to match directly with the ones seen on the target wall for the first couple of jets; as the downstream distance increases, the side wall peaks are seen to be shifting downstream with respect to the corresponding peak in target wall Nusselt number. This direct comparison shows the impact of the crossflow by forcing through both sides of the channel and deflecting the wall jet downstream. Similar to the description by Florschuetz et al. [18] explaining that the negative effect of the crossflow is a combination of mass flux ratio, G_c/G_j , and channel height, Z/D ; it is seen that the downstream shift of the side wall is also proportional to the mass flux ratio and channel height. Additional differences are the shift of the maxima on the tall side walls away from the target wall at middle streamwise locations.

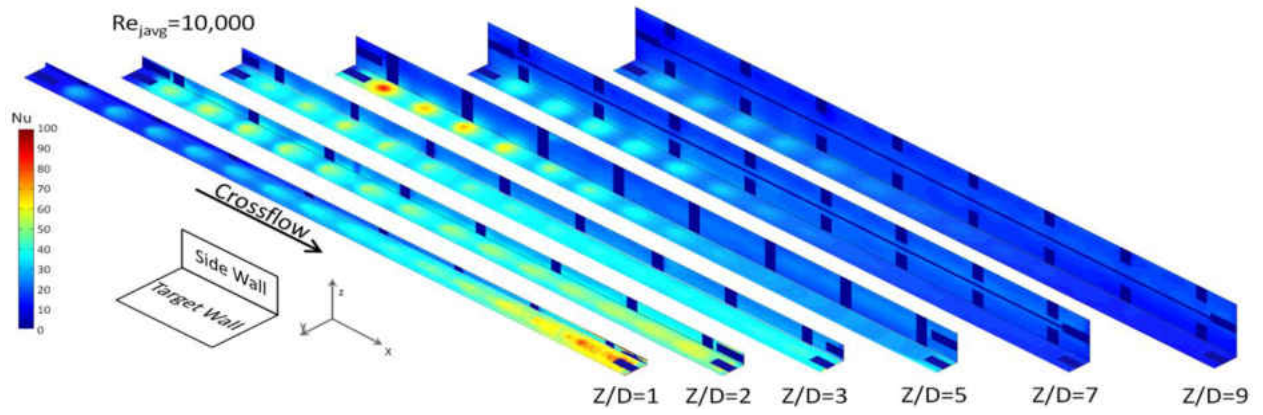


Figure 25: Isometric View of all Channels at $Re_{javg} = 10,000$

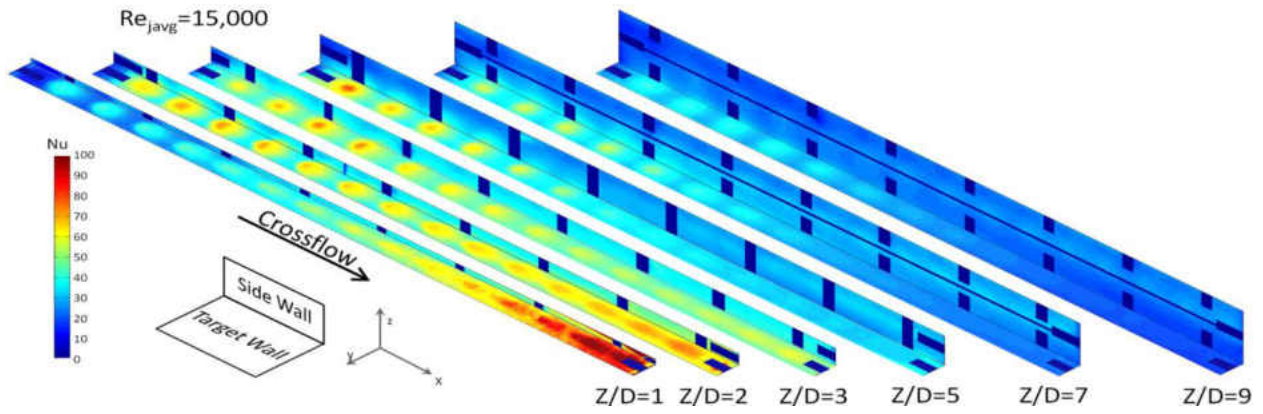


Figure 26: Isometric View of all Channels at $Re_{javg} = 15,000$

CHAPTER EIGHT: HEAT TRANSFER DATA ANALYSIS

Nusselt Number Dependence of Reynolds number

Reynolds number dependence of all channels was studied. The 15 points of pitch averaged Nusselt number were averaged to generate an area average for each wall at every single Reynolds number. It is seen in the literature that Nusselt number trends proportional to Reynolds number raised to a power “m”. Taking a logarithmic of both quantities, Nusselt and Reynolds number, and plotting the five resulting points alongside a linear fit provides the Reynolds number exponent “m” as the slope of the linear regression. This process was done for all channel heights on both the target and side walls. Table 5 shows the values of the “m” coefficients for all twelve cases.

Table 5: Nusselt Number Dependence on Reynolds Number

	Target Wall	Side Wall	Average
Z/D=1	0.847	0.910	0.88
Z/D=2	0.906	0.879	0.89
Z/D=3	0.780	0.836	0.81
Z/D=5	0.631	0.750	0.69
Z/D=7	0.869	0.788	0.83
Z/D=9	0.785	0.760	0.77

The non-monotonic variation of Reynolds number exponents throughout the domain does not lend the data to be collapsed by any function of Reynolds number exponent versus channel height function as the one given by Florschuetz et al. [18]. Throughout the first four channel heights, $Z/D = 1, 2, 3,$ and 5 , the values seem to be decreasing as expected by the Florschuetz et al. correlation; however, once $Z/D = 7$ and 9 are considered, the trend collapses. The cause of this anomaly is believed to originate due the combination of uncertainty from Reynolds Number and Nusselt number combining leading the uncertainty of the Reynolds number coefficient to be

larger than their relative differences. A plot of Reynolds number coefficients as a function of channel height is seen in Figure 27.

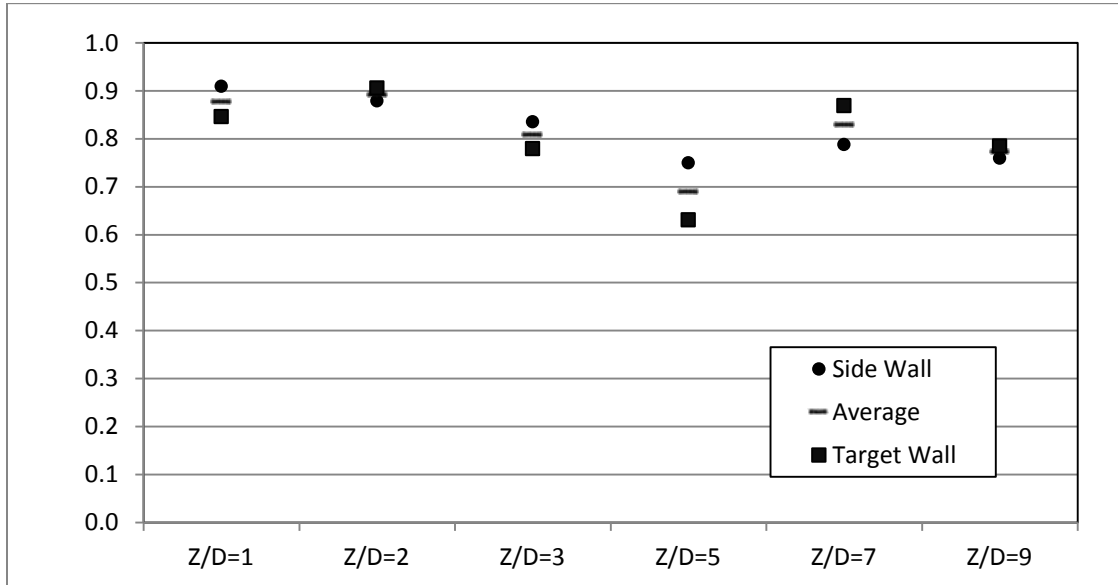


Figure 27: Variation of Reynolds Number Exponent, "m", as a Function of Wall and Channel Height

In order to ensure continuity of flow and wall fluxes, the Reynolds number exponents between target wall and side wall at a single channel height are expected to be the same; that is, both the side wall and the target wall behave identically with a change in Reynolds number. The variation seen among the target and side wall Reynolds number coefficients are small compared to the uncertainty in the value "m". Therefore, the small differences in Reynolds number coefficient can be assumed to be statistically insignificant. Unfortunately, the differences between the average Reynolds number coefficients values as a function of channel heights are within uncertainty and cannot be used to draw any significant contribution of channel height effects on Reynolds number exponent.

Total Heat Transfer Contribution

In order to see which channel provides the maximum amount of heat transfer, the area averaged Nusselt number at $Re_{j,avg}=10,000$ and $15,000$ were multiplied with their respective width. For example, all target wall area averaged Nusselt numbers were multiplied by $Y_c/D=4$, all side walls were multiplied by their respective non dimensional heights, Z/D , and by a factor of two signifying the contributions from both side walls. A table was generated with the contributions from target and side walls as well as their sum being shown at the two Reynolds numbers. The results are shown in Table 6.

Table 6: Total Channel Heat Transfer

	$Re_{j,avg}=10,000$			$Re_{j,avg}=15,000$		
	Target Wall Contribution	Side Wall Contribution	Total	Target Wall Contribution	Side Wall Contribution	Total
$Z/D=1$	137	44	180	199	75	274
$Z/D=2$	166	125	291	223	164	387
$Z/D=3$	145	150	296	200	221	420
$Z/D=5$	135	216	350	154	286	440
$Z/D=7$	91	269	360	125	365	490
$Z/D=9$	76	295	371	102	395	496

In order to get a better feeling of the specific contributions from target and side walls on the total heat transfer of the channel, they were plotted as a function of channel height for both Reynolds numbers; Figure 28 shows the channel heat transfer for a Reynolds number of 10,000 while Figure 29 shows it for a Reynolds number of 15,000. It can be seen that the trends do not vary with Reynolds number. The maximum overall heat transfer rate is achieved by the $Z/D=9$ channel due to the large area that the heat has the ability to travel through. The designer must choose a balance between target wall heat transfer versus increasing the side wall heat transfer area. It seems that a $Z/D=3$ supports the highest target wall and side wall heat transfer

coefficients. Other parameters are also to be taken into account such as availability of space and the minimum acceptable target wall heat transfer.

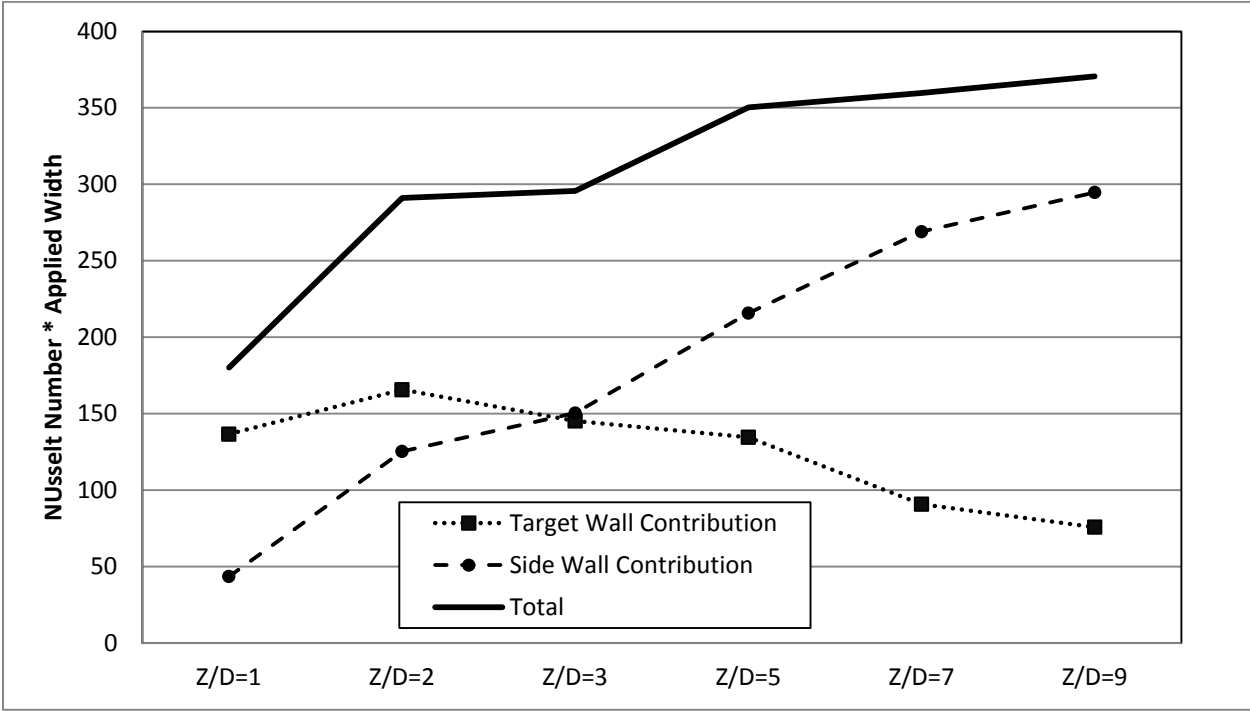


Figure 28: Contributions of Target and Side Walls on Overall Channel Heat Transfer for $Re_{javg}=10,000$

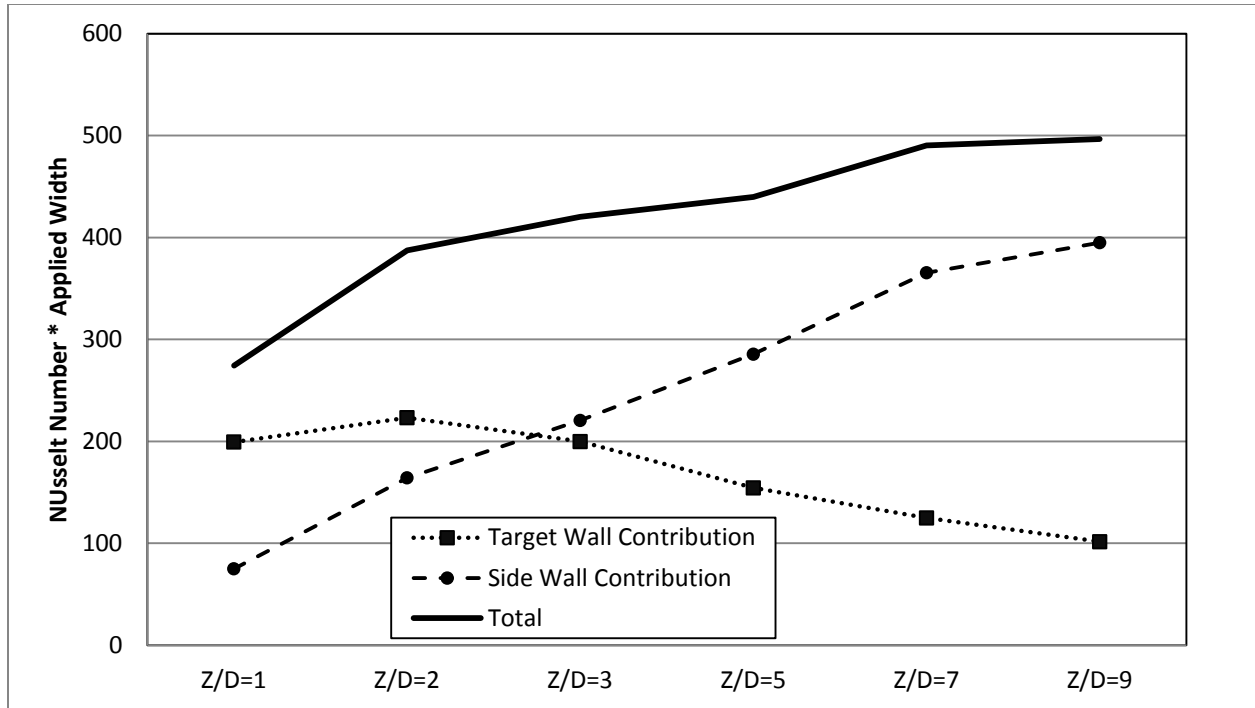


Figure 29: Contributions of Target and Side Walls on Overall Channel Heat Transfer for $Re_{j,avg}=15,000$

Comparisons with Florschuetz et al. [18] Correlation

Using the correlation provided by Florschuetz et al. [18], two channel heights were compared at two Reynolds numbers each. The channel heights compared were $Z/D = 2$ which lies well within the test matrix of Florschuetz et al. and $Z/D=3$ which lies at one extreme end of the test matrix. The results are shown in Figure 30 for $Z/D=2$ channel and in Figure 31 for the $Z/D=3$ channel.

The results of the $Z/D=2$ channel are seen to agree well with the Florschuetz et al. correlation; the correlation predicts a slight decrease in heat transfer due to crossflow followed by an increase in heat transfer due to an increase of jet mass flux as a function of streamwise location previously described with the use of Figure 17.

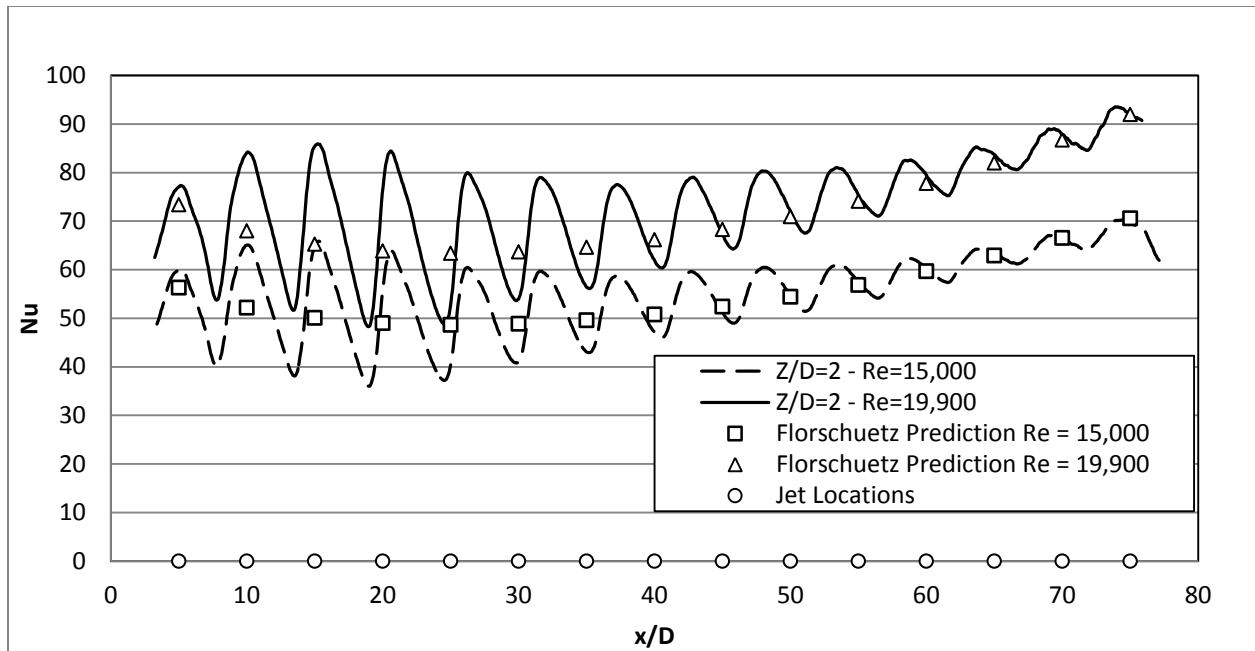


Figure 30: $Z/D = 2$ Nusselt Number Profile Comparisons with Florschuetz et al.

The $Z/D = 3$ results do not match as well as the ones for the $Z/D = 2$ channel. The discrepancy may be due to the Florschuetz correlation not being valid at one of the corners of the Florschuetz matrix ($Z/D = 5$, $Y/D = 4$, $Z/D = 3$). The results; however, show an interesting aspect of the profile that is predicted by the correlation which is the positive concavity of the Nusselt number profile; as G_c/G_j increases, there comes a point where the crossflow starts dominating the heat transfer inside the channel and its effects switch from being detrimental to the overall heat transfer at low x/D to an increase in heat transfer due to channel flow similar to the one predicted by the Dittus-Boelter correlation.

The area averaged values of the Florschuetz correlation compared to the area averaged values of the current data lie within experimental uncertainty of both the correlation and the current data. Having the uncertainty estimates being significant compared to the magnitude of the difference between the prediction and the actual values as well as the knowledge that the

point where the comparisons are trying to be made is in a corner of the test matrix used to develop the correlation allows for the safe assumption that the results are valid for their respective tests. A much safer comparison is shown with the $Z/D=2$ channel since it lies inside the Florschuetz test matrix.

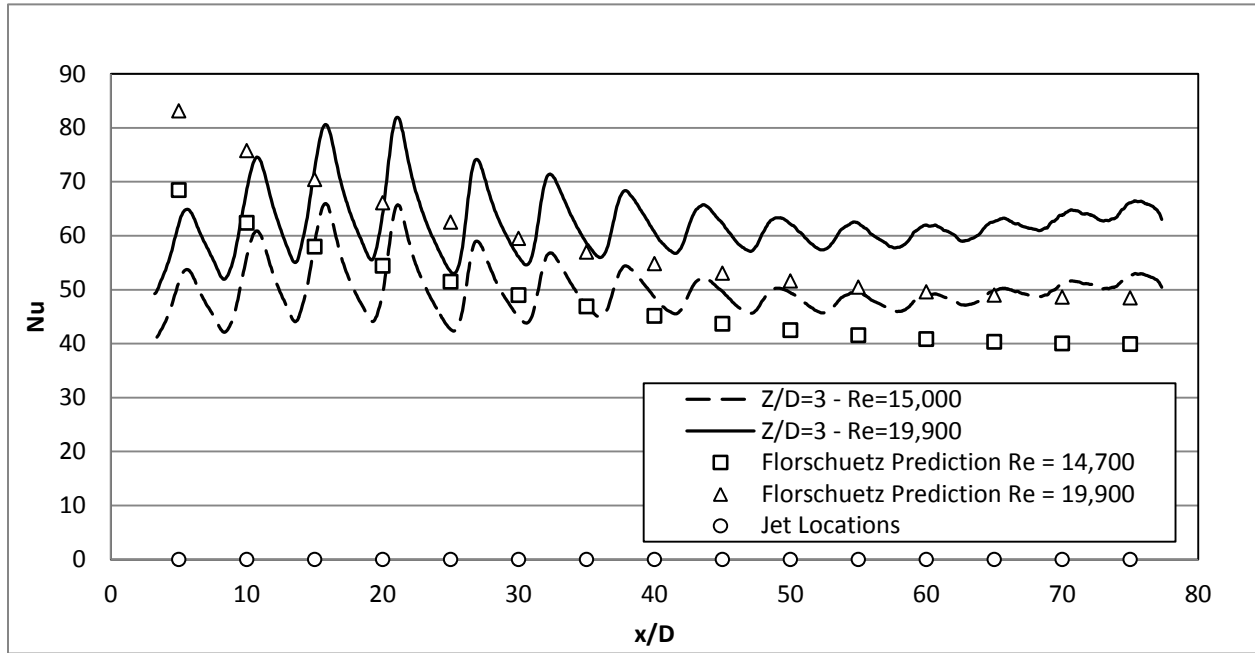


Figure 31: $Z/D = 3$ Nusselt Number Profile Comparisons with Florschuetz et al.

CHAPTER NINE: CONCLUSIONS

The work by Ricklick [45] has been continued to fully understand the effect of channel height on target wall as well as side wall Nusselt number. The research involves the heat transfer characterization of six inline impingement channels at channel heights of $Z/D = 1, 2, 3, 5, 7,$ and 9. A single streamwise jet spacing of $X/D = 5$ and lateral spacing of $Y/D = 4$ was studied. It is shown that the target and side walls interact to generate large heat transfer profiles at the lower height of the side walls. Results also show dependencies of the downstream shift in Nusselt number on channel height and mass flux ratios as previously seen by Florschuetz et al. [17]

The impact of side walls were seen to be significant when total channel heat transfer was calculated; at low impingement heights, the side walls, due to their small size, do not display a significant amount of heat transfer capability; however, as the channel height increase, the effect of side walls on overall heat transfer increases. At $Z/D=3$ the two side walls have the same heat transfer capacity as the single target wall; as Z/D increases, although the area averaged Nusselt number drops, the overall heat transfer capability increases due to the larger area. At $Z/D=1$, both side walls accounted for a mere 24% of the overall heat transfer of the channel; at a $Z/D=3$, the side walls provided a total of 50% of the heat transfer; as the channel height is increased to $Z/D = 9$ the amount of heat transfer provided by the side walls increased 80% of the heat transfer capacity of the channel. The previous results symbolize the importance of the inclusion of side wall heat transfer to a confined impingement channel.

APPENDIX A: NUSSELT NUMBER PROFILES

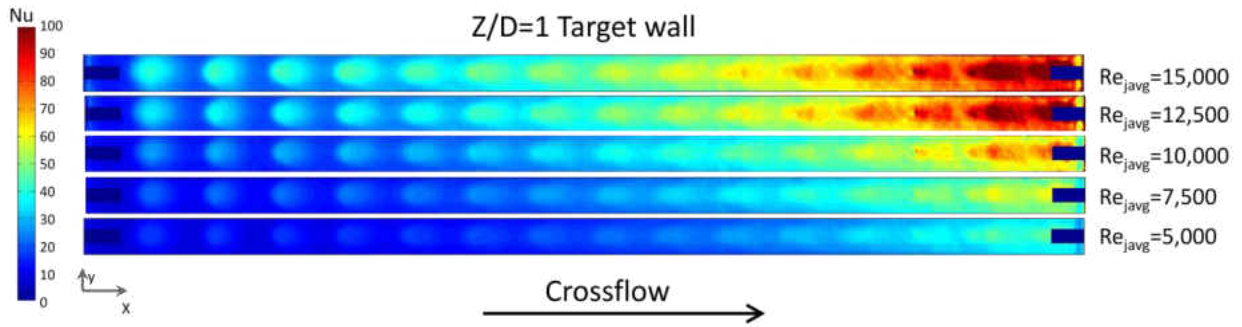


Figure 32: $Z/D=1$ Target Wall Nusselt number Profiles at Multiple Reynolds Numbers

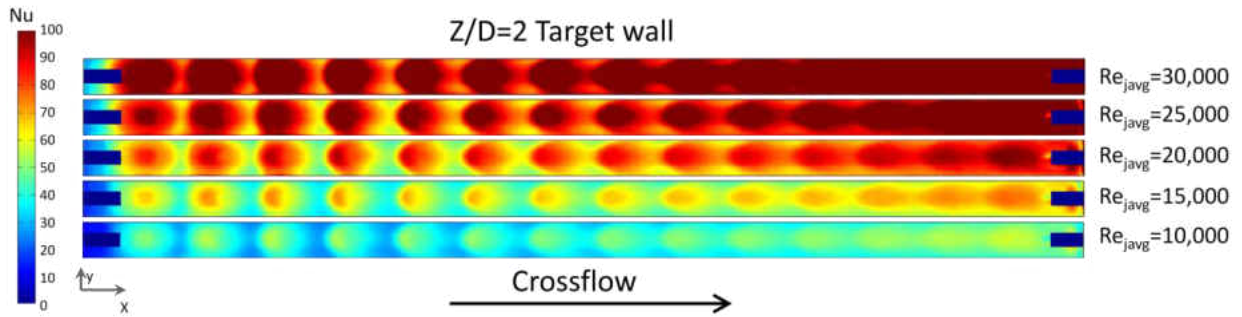


Figure 33: $Z/D=2$ Target Wall Nusselt number Profiles at Multiple Reynolds Numbers

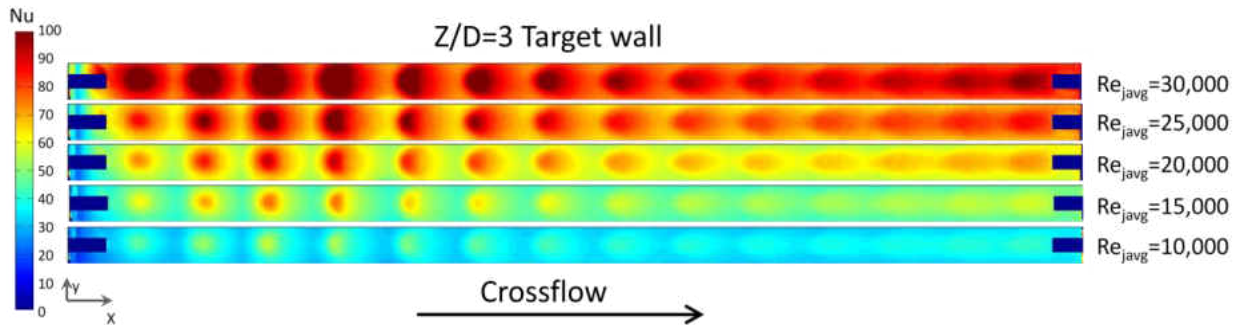


Figure 34: $Z/D=3$ Target Wall Nusselt number Profiles at Multiple Reynolds Numbers

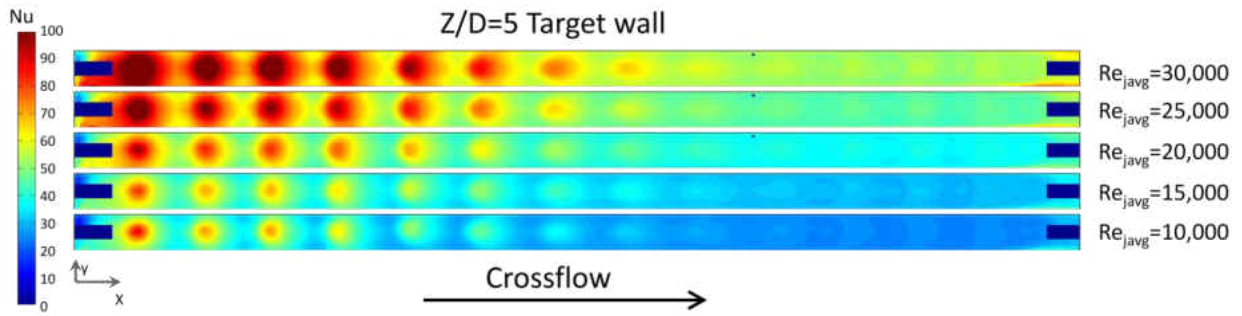


Figure 35: Z/D=5 Target Wall Nusselt number Profiles at Multiple Reynolds Numbers

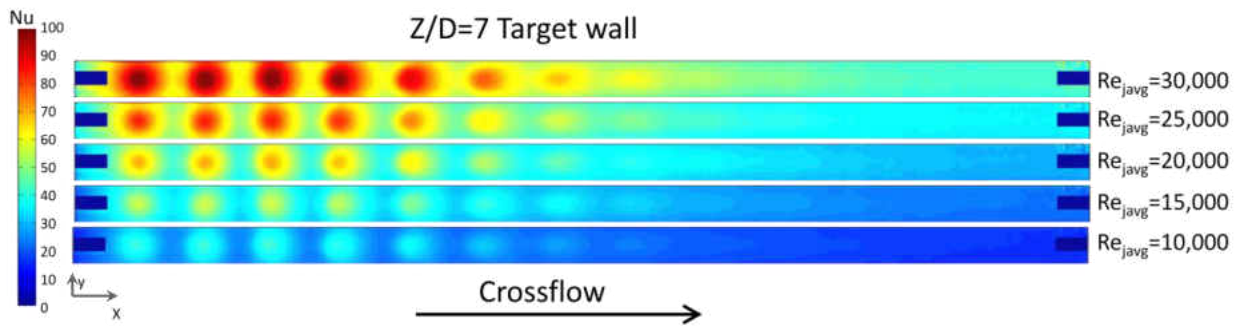


Figure 36: Z/D=7 Target Wall Nusselt number Profiles at Multiple Reynolds Numbers

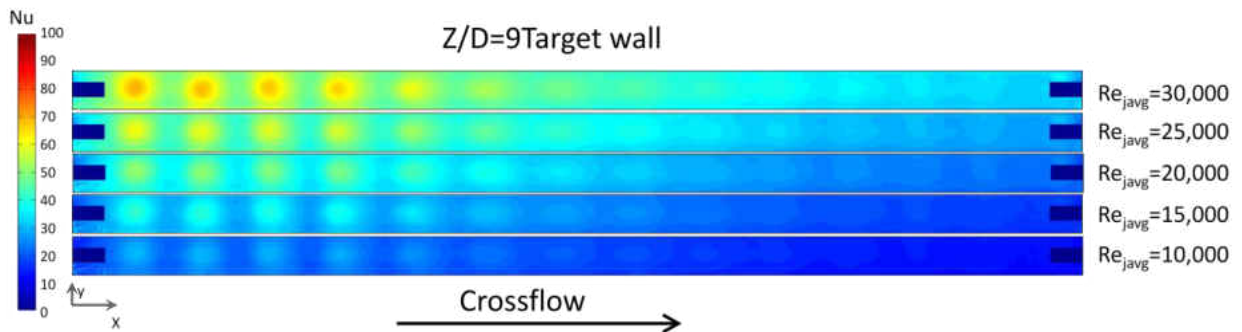


Figure 37: Z/D=9 Target Wall Nusselt number Profiles at Multiple Reynolds Numbers

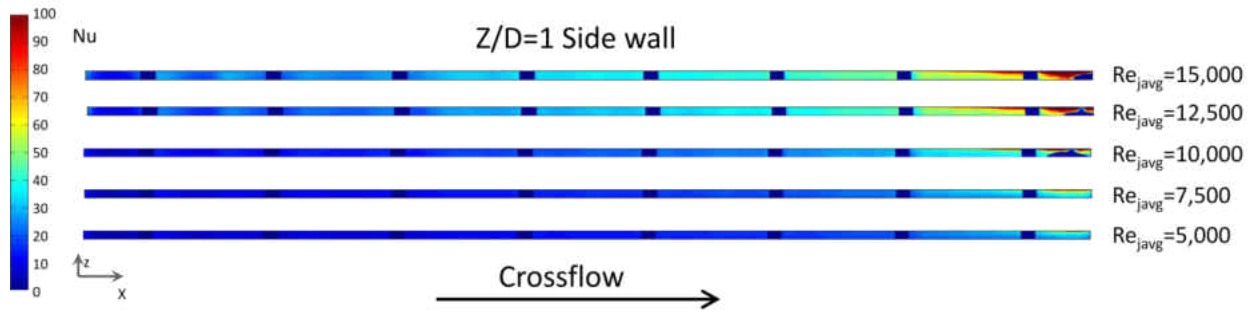


Figure 38: Z/D=1 Side Wall Nusselt number Profiles at Multiple Reynolds Numbers

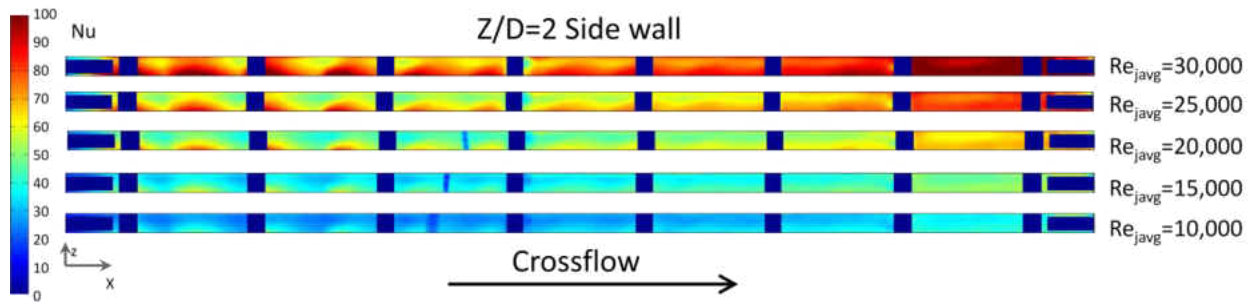


Figure 39: Z/D=2 Side Wall Nusselt number Profiles at Multiple Reynolds Numbers

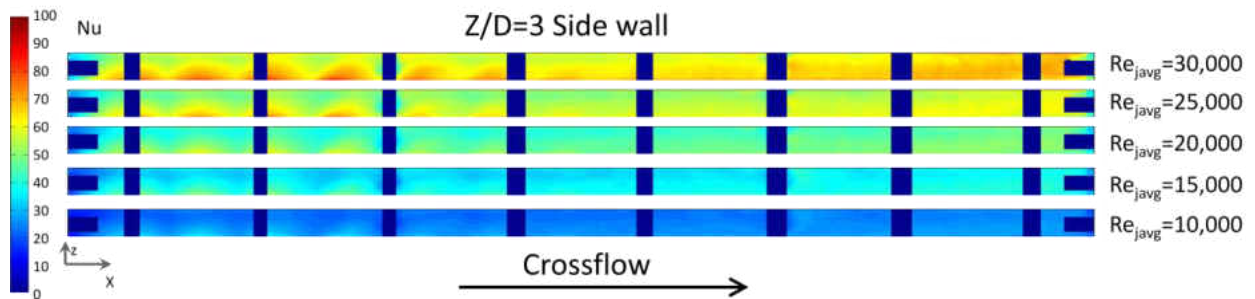


Figure 40: Z/D=3 Side Wall Nusselt number Profiles at Multiple Reynolds Numbers

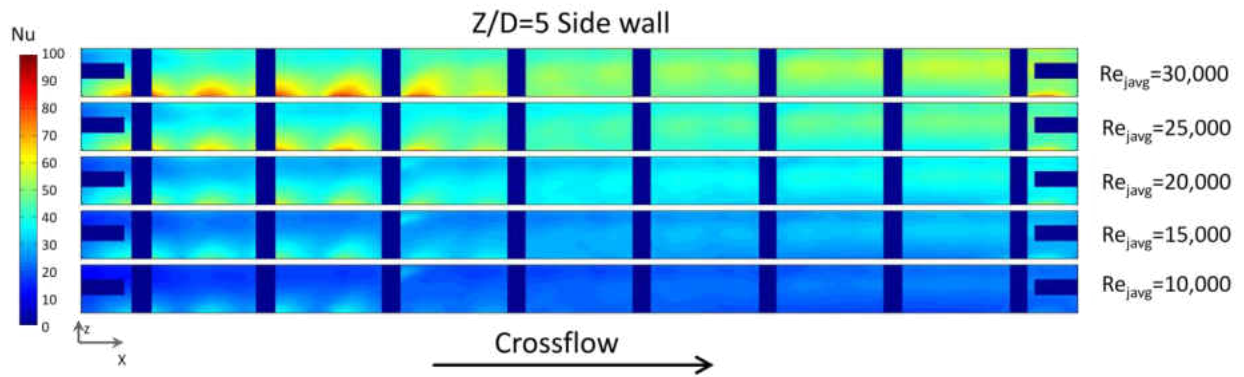


Figure 41: $Z/D=5$ Side Wall Nusselt number Profiles at Multiple Reynolds Numbers

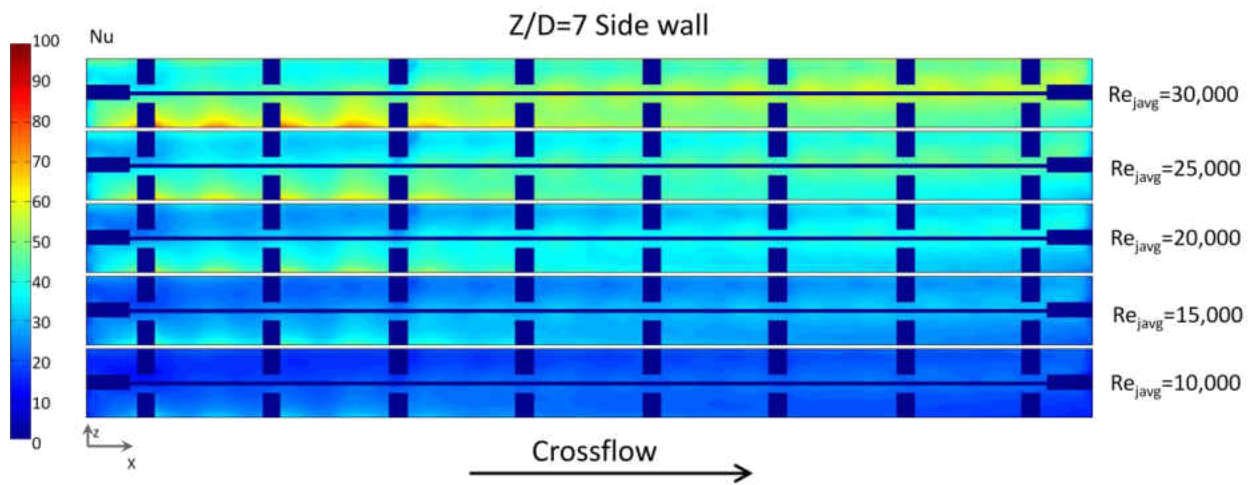


Figure 42: $Z/D=7$ Side Wall Nusselt number Profiles at Multiple Reynolds Numbers

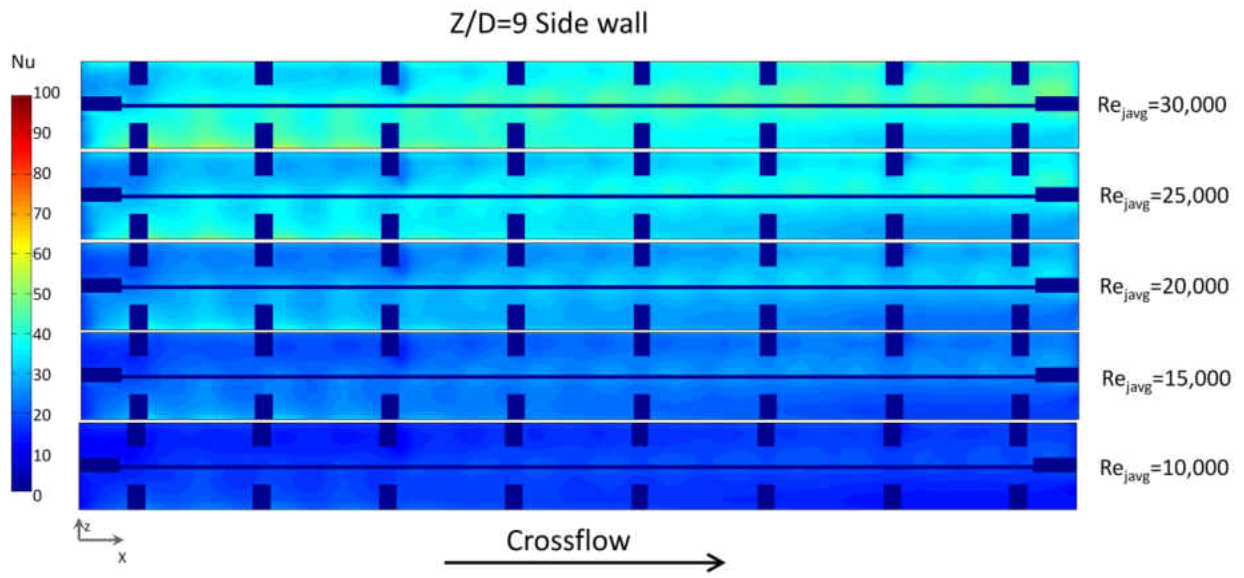


Figure 43: $Z/D=9$ Side Wall Nusselt number Profiles at Multiple Reynolds Numbers

APPENDIX B: SPAN AVERAGED NUSSOLT NUMBER DATA

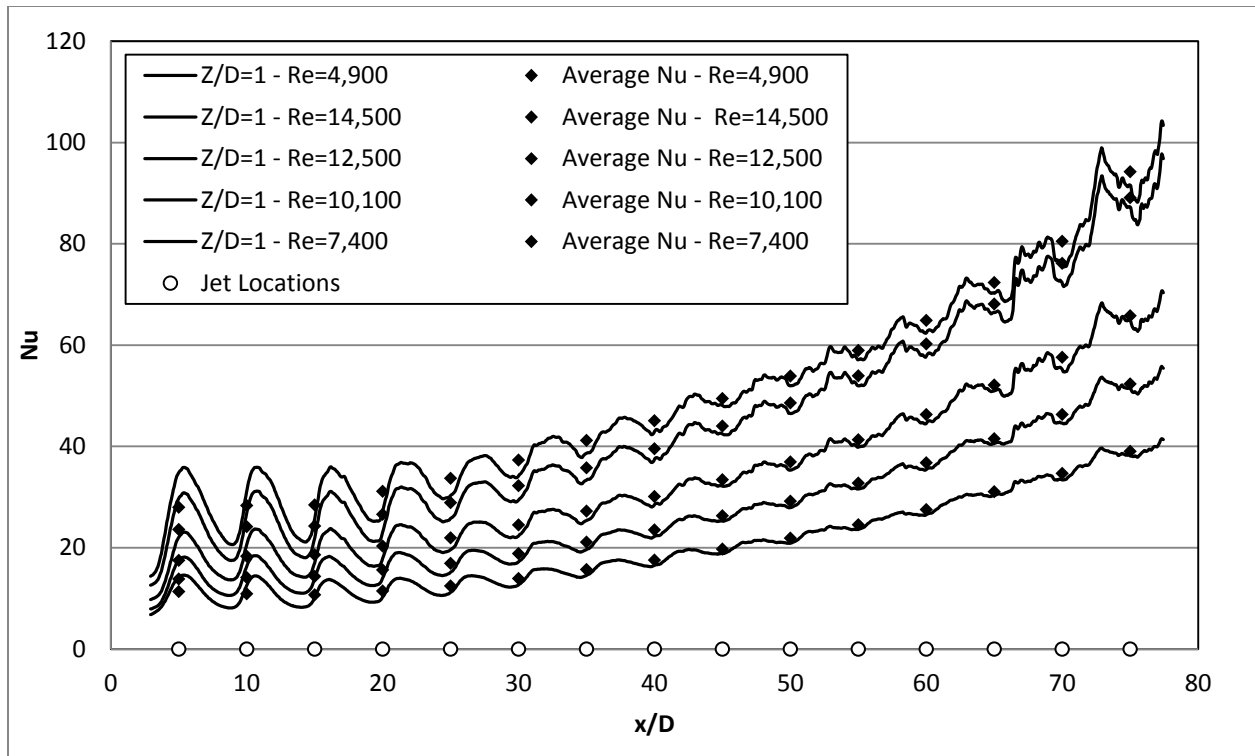


Figure 44: Target Wall Laterally Averaged Nusselt Number for $Z/D=1$

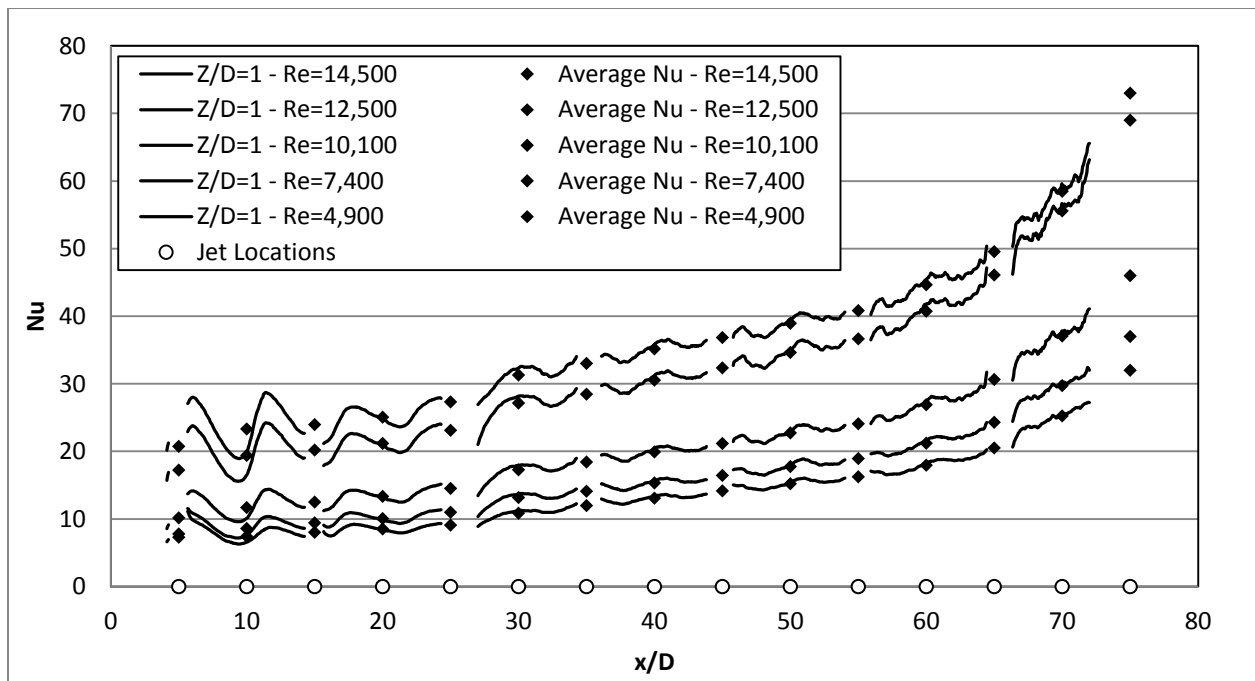


Figure 45: Side Wall Laterally Averaged Nusselt Number for $Z/D=1$

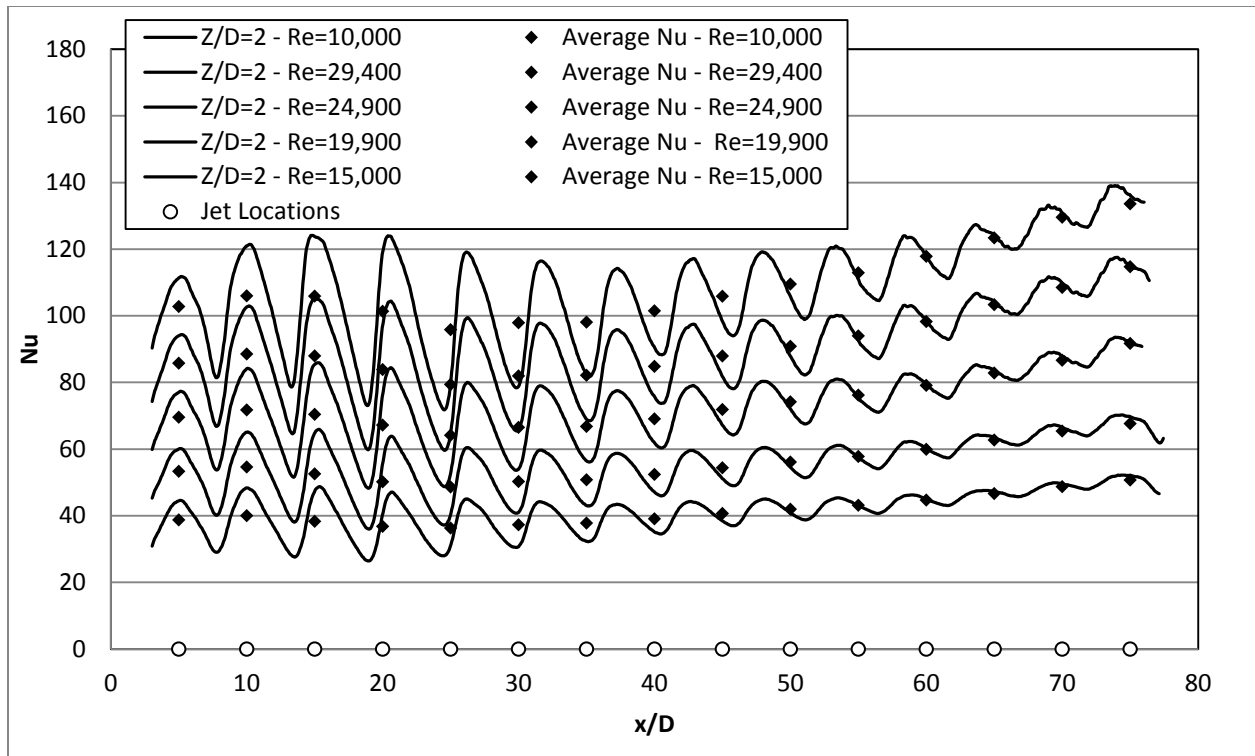


Figure 46: Target Wall Laterally Averaged Nusselt Number for $Z/D=2$

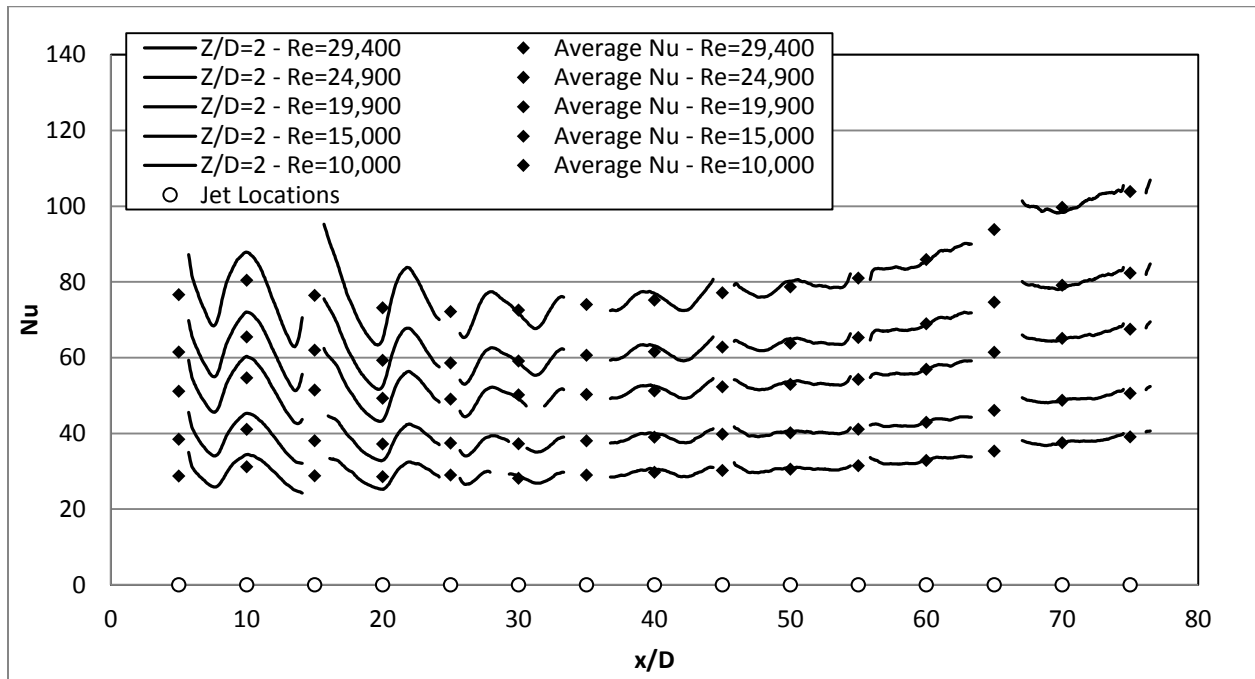


Figure 47: Wall Laterally Averaged Nusselt Number for $Z/D=2$

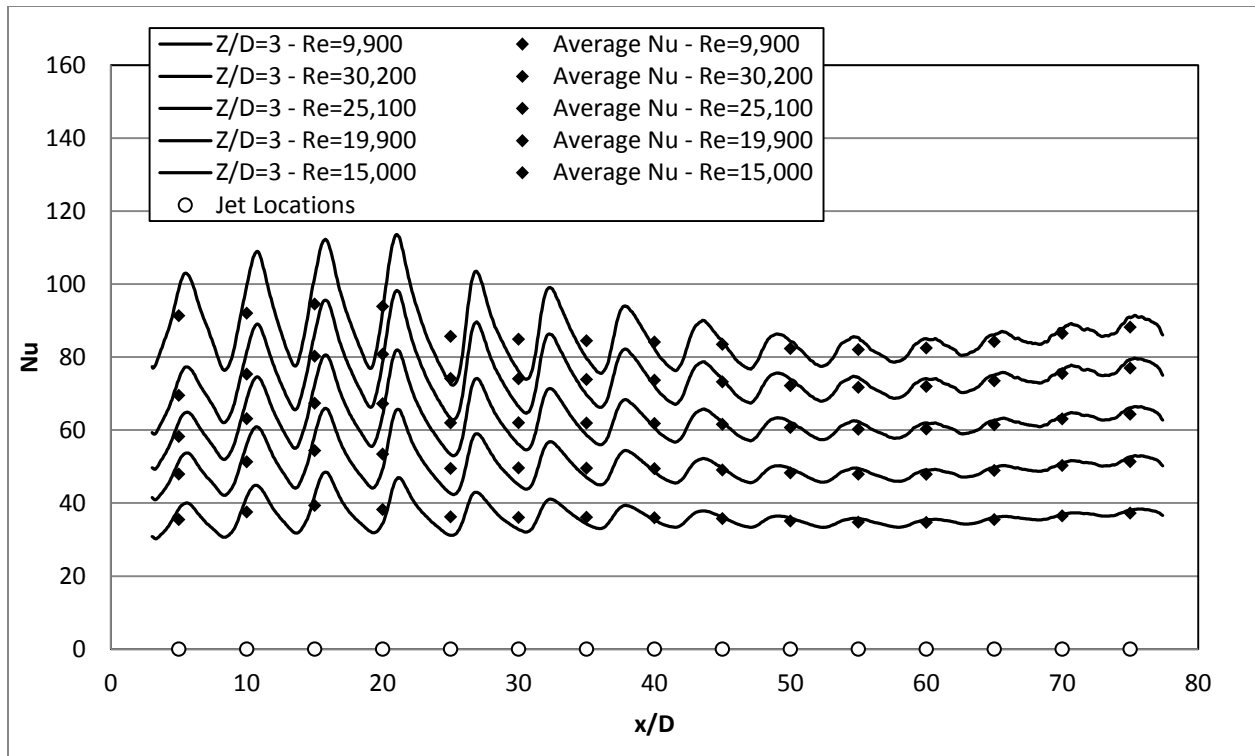


Figure 48: Target Wall Laterally Averaged Nusselt Number for $Z/D=3$

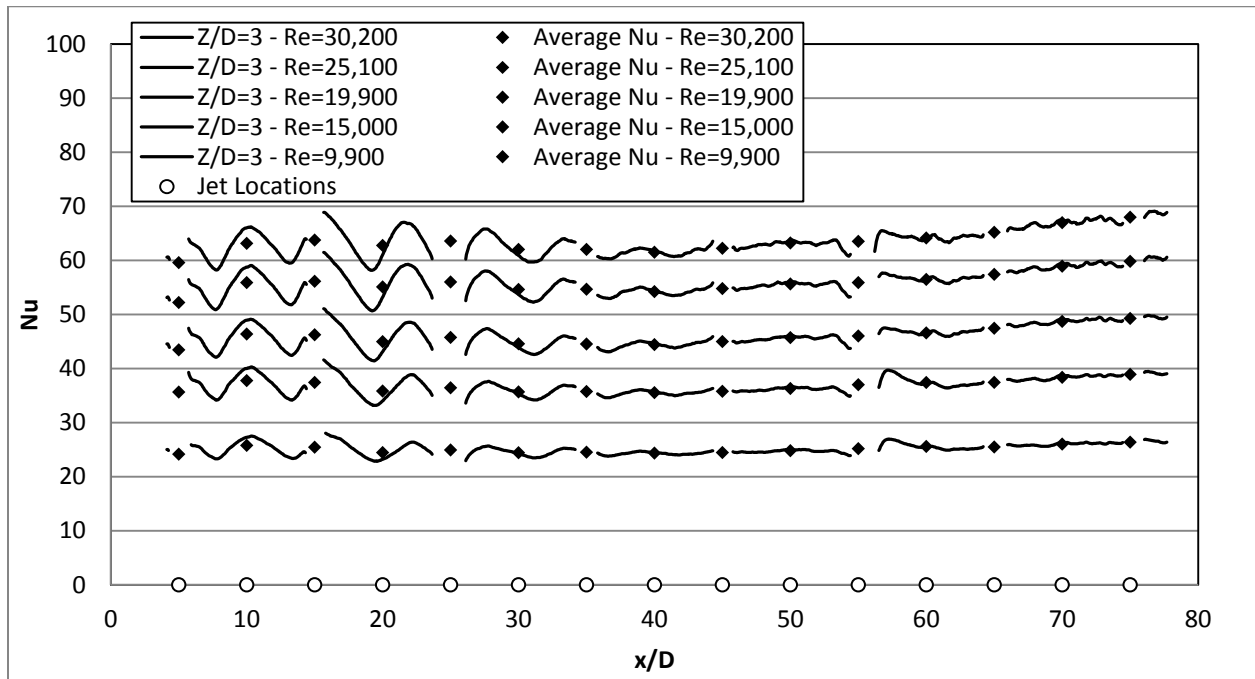


Figure 49: Wall Laterally Averaged Nusselt Number for $Z/D=3$

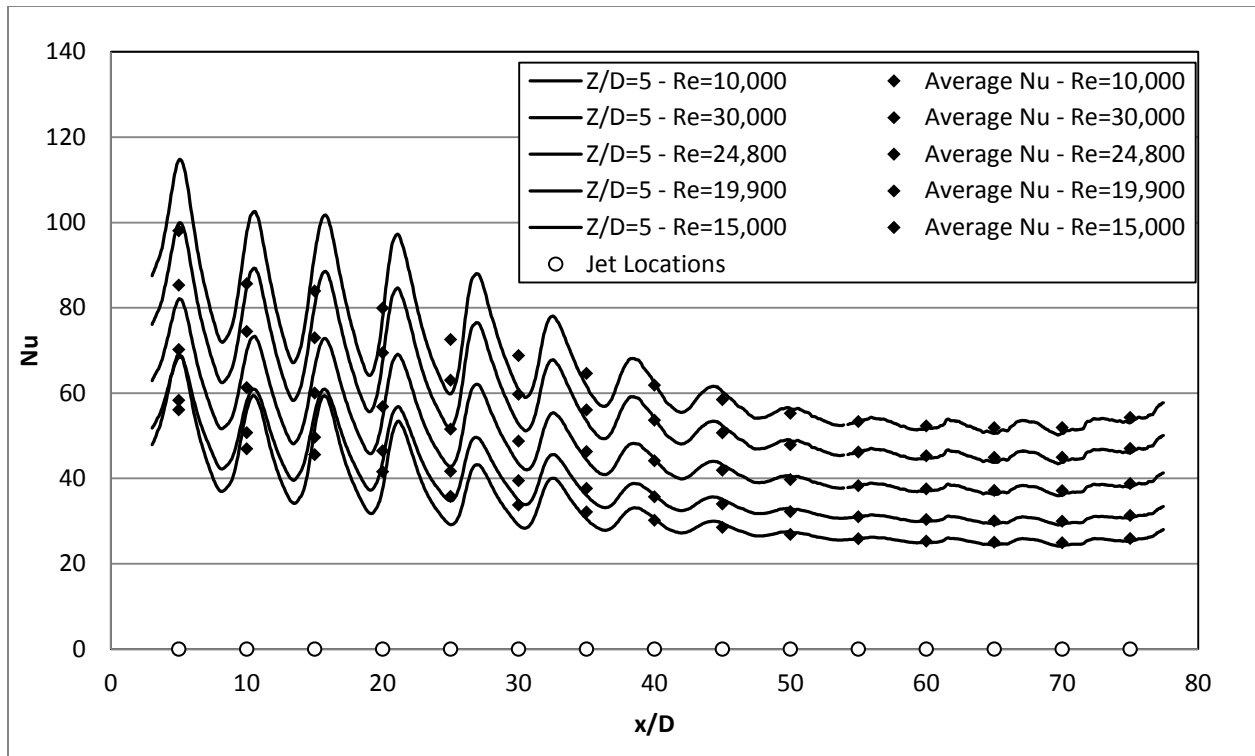


Figure 50: Target Wall Laterally Averaged Nusselt Number for $Z/D=5$

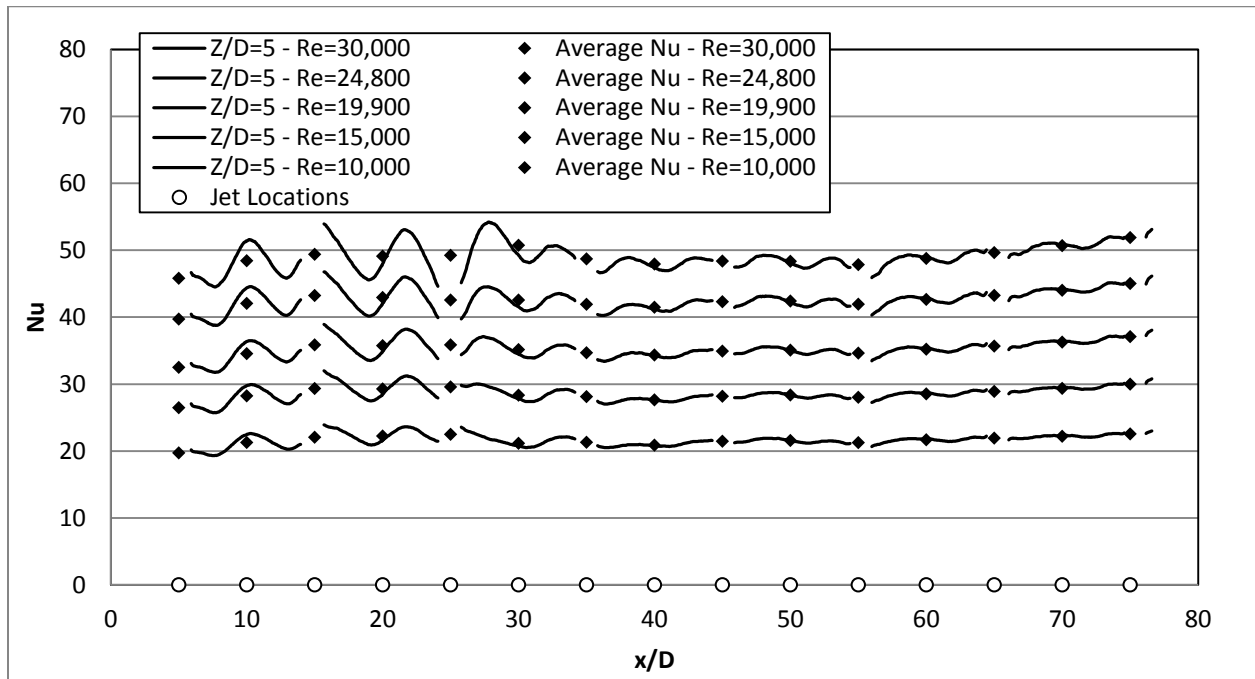


Figure 51: Wall Laterally Averaged Nusselt Number for $Z/D=5$

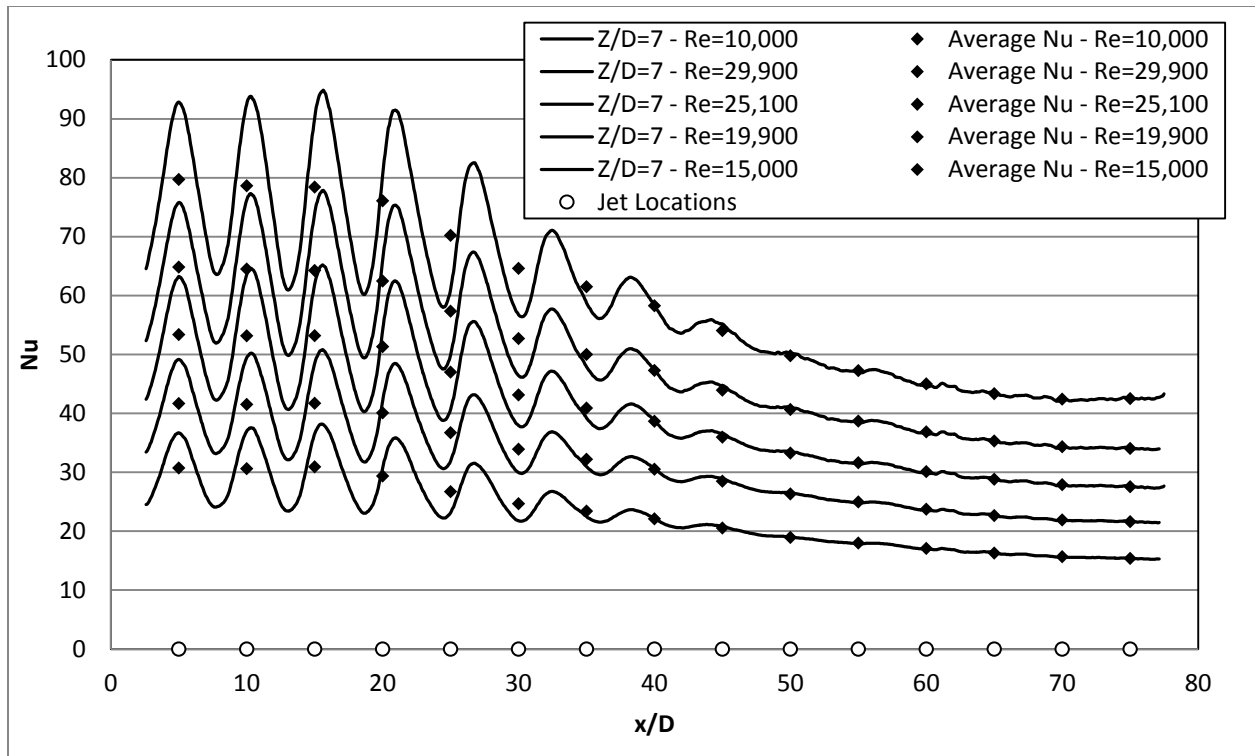


Figure 52: Target Wall Laterally Averaged Nusselt Number for $Z/D=7$

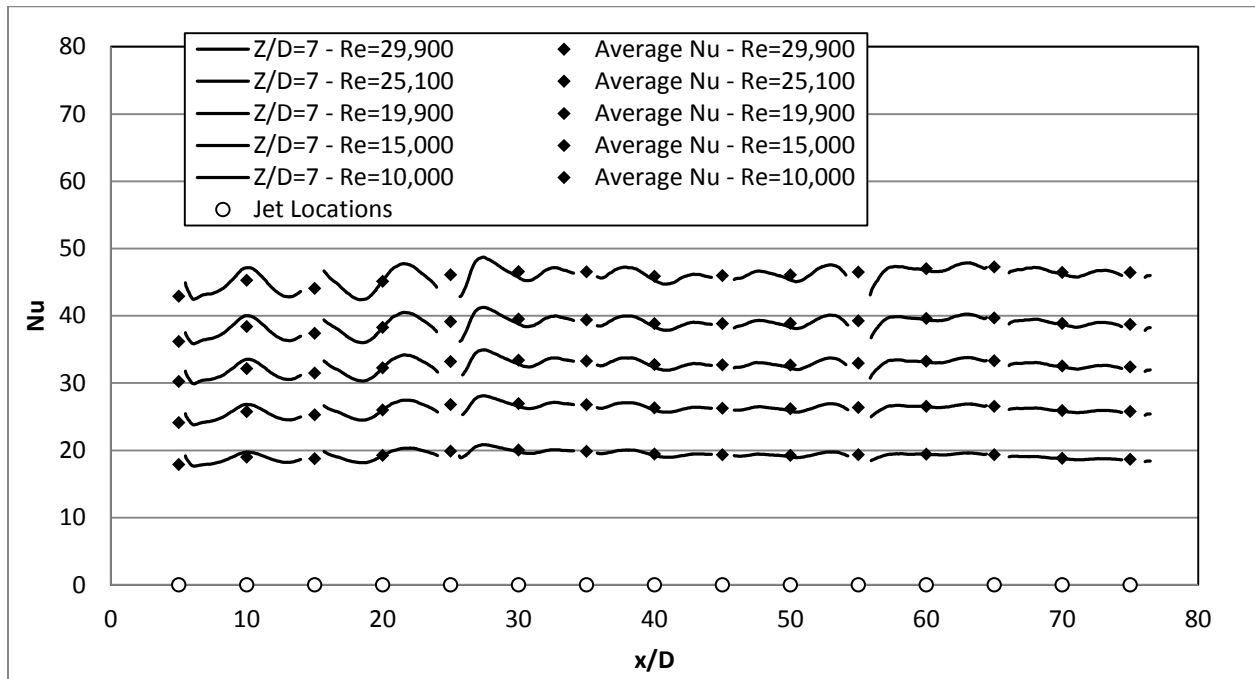


Figure 53: Wall Laterally Averaged Nusselt Number for $Z/D=7$

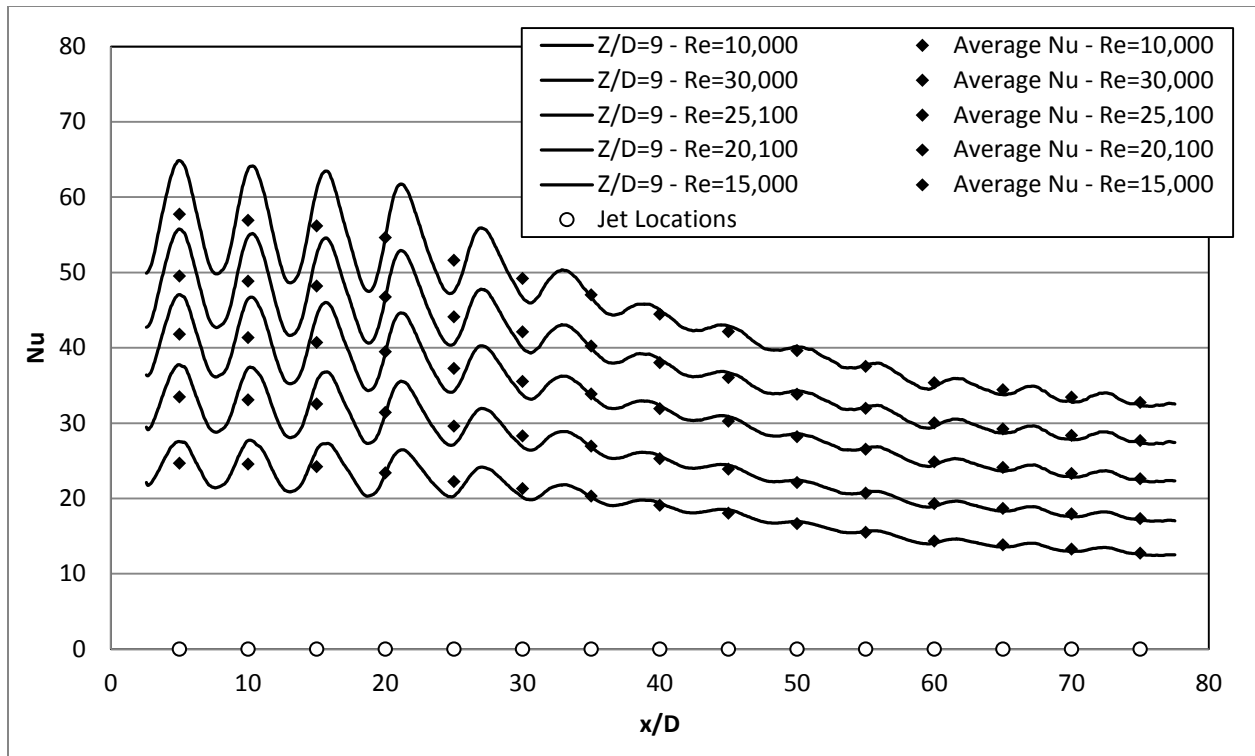


Figure 54: Target Wall Laterally Averaged Nusselt Number for Z/D=9

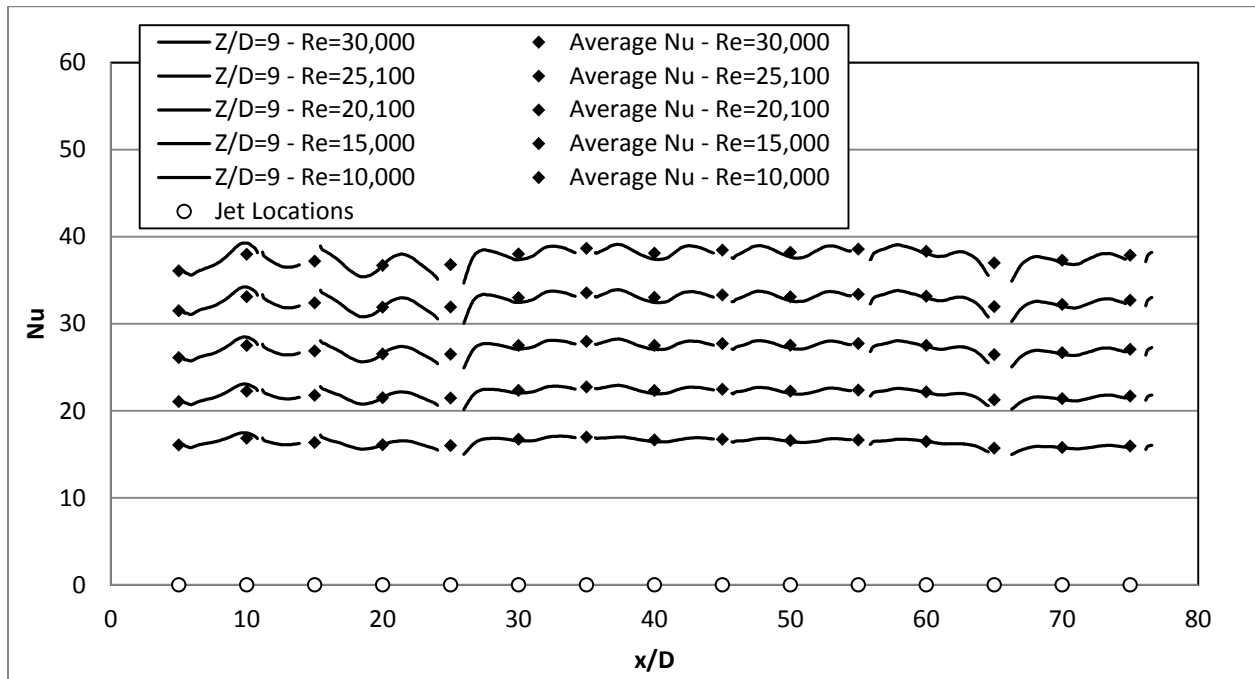


Figure 55: Wall Laterally Averaged Nusselt Number for Z/D=9

APPENDIX C: TABULATED NUSSELT NUMBER DATA

Table 7: Z/D=1 Target Wall Pitch Averaged Nusselt Number

Z/D=1 Target Wall Pitch Averaged Nusselt Number					
Jet No	Re=14,500	Re=12,500	Re=10,100	Re=7,400	Re=4,900
1	28.00	23.62	17.52	13.84	11.36
2	28.34	24.17	18.34	14.14	10.91
3	28.46	24.29	18.62	14.35	10.71
4	31.15	26.60	20.34	15.63	11.47
5	33.72	28.91	21.96	16.92	12.46
6	37.32	32.25	24.52	18.86	13.94
7	41.20	35.79	27.24	21.12	15.71
8	45.08	39.55	30.12	23.53	17.57
9	49.46	44.03	33.44	26.32	19.75
10	53.90	48.60	36.95	29.20	21.90
11	58.96	53.95	41.33	32.77	24.55
12	64.89	60.25	46.30	36.79	27.54
13	72.37	68.13	52.13	41.54	31.08
14	80.51	76.16	57.61	46.32	34.69
15	94.24	89.12	65.81	52.35	39.04
Area Avg	49.84	45.03	34.15	26.91	20.18

Table 8: Z/D=1 Side Wall Pitch Averaged Nusselt Number

Z/D=1 Side Wall Pitch Averaged Nusselt Number					
Jet No	Re=14,500	Re=12,500	Re=10,100	Re=7,400	Re=4,900
1	20.74	17.23	10.17	7.79	7.30
2	23.32	19.41	11.70	8.60	7.42
3	23.97	20.20	12.51	9.42	8.03
4	25.06	21.18	13.35	10.06	8.53
5	27.32	23.12	14.52	11.00	9.09
6	31.30	27.15	17.28	13.17	10.86
7	33.02	28.47	18.43	14.11	11.98
8	35.17	30.54	19.91	15.33	13.08
9	36.84	32.36	21.17	16.44	14.16
10	38.95	34.64	22.73	17.75	15.22
11	40.83	36.65	24.09	18.94	16.24
12	44.66	40.74	26.90	21.21	17.96
13	49.55	46.10	30.64	24.31	20.51
14	58.48	55.58	37.07	29.73	25.25
15	73.00	69.00	46.00	37.00	32.00
Area Avg	37.48	33.49	21.76	16.99	14.51

Table 9: Z/D=2 Target Wall Pitch Averaged Nusselt Number

Z/D=2 Target Wall Pitch Averaged Nusselt Number					
Jet No	Re=29,400	Re=24,900	Re=19,900	Re=15,000	Re=10,000
1	102.80	85.79	69.58	53.34	38.76
2	106.00	88.55	71.77	54.63	40.03
3	105.92	87.97	70.44	52.58	38.34
4	101.37	83.88	67.22	50.19	36.82
5	95.85	79.41	64.17	48.64	36.33
6	97.93	81.96	66.53	50.29	37.31
7	98.11	82.16	66.81	50.80	37.81
8	101.50	84.83	69.08	52.41	39.09
9	105.88	87.96	71.89	54.40	40.70
10	109.53	90.86	74.19	56.12	41.97
11	112.93	93.99	76.21	57.79	43.16
12	117.85	98.28	79.13	59.94	44.72
13	123.40	103.36	82.84	62.73	46.67
14	129.58	108.52	86.67	65.43	48.74
15	133.61	114.73	91.72	67.66	50.72
Area Avg	109.48	91.48	73.88	55.80	41.41

Table 10: Z/D=2 Side Wall Pitch Averaged Nusselt Number

Z/D=2 Side Wall Pitch Averaged Nusselt Number					
Jet No	Re=29,400	Re=24,900	Re=19,900	Re=15,000	Re=10,000
1	76.63	61.48	51.12	38.44	28.73
2	80.44	65.46	54.65	41.06	31.17
3	76.45	61.97	51.43	38.05	28.79
4	73.16	59.29	49.28	37.19	28.55
5	72.16	58.59	49.04	37.43	28.99
6	72.55	59.10	50.17	37.25	28.14
7	74.03	60.63	50.27	38.03	28.98
8	75.19	61.56	51.21	38.99	29.71
9	77.13	62.78	52.29	39.78	30.20
10	78.68	63.78	52.94	40.14	30.53
11	81.00	65.31	54.26	41.10	31.46
12	85.90	68.95	56.93	42.92	32.85
13	93.83	74.64	61.42	46.07	35.32
14	99.69	79.12	65.09	48.74	37.52
15	103.86	82.35	67.51	50.58	39.06
Area Avg	81.38	65.67	54.51	41.05	31.33

Table 11: Z/D=3 Target Wall Pitch Averaged Nusselt Number

Z/D=3 Target Wall Pitch Averaged Nusselt Number					
Jet No	Re=30,200	Re=25,100	Re=19,900	Re=15,000	Re=9,900
1	91.36	69.54	58.26	47.95	35.49
2	92.05	75.35	63.14	51.32	37.57
3	94.56	80.28	67.38	54.39	39.37
4	93.91	80.80	67.26	53.44	38.25
5	85.70	74.16	61.99	49.51	36.24
6	84.93	74.07	62.03	49.65	36.07
7	84.50	73.89	61.93	49.58	36.13
8	84.15	73.69	61.82	49.44	35.99
9	83.52	73.23	61.60	49.08	35.76
10	82.36	72.19	60.72	48.28	35.11
11	82.08	71.73	60.24	47.93	34.77
12	82.51	71.98	60.31	47.90	34.70
13	84.28	73.51	61.47	48.95	35.49
14	86.52	75.51	63.09	50.32	36.50
15	88.23	77.02	64.36	51.37	37.26
Area Avg	86.71	74.46	62.37	49.94	36.31

Table 12: Z/D=3 Side Wall Pitch Averaged Nusselt Number

Z/D=3 Side Wall Pitch Averaged Nusselt Number					
Jet No	Re=30,200	Re=25,100	Re=19,900	Re=15,000	Re=9,900
1	59.58	52.20	43.45	35.65	24.16
2	63.15	55.89	46.38	37.77	25.78
3	63.75	56.13	46.24	37.42	25.44
4	62.76	55.09	44.97	35.84	24.45
5	63.58	56.00	45.75	36.44	24.93
6	62.03	54.62	44.57	35.68	24.43
7	62.02	54.66	44.53	35.75	24.52
8	61.50	54.22	44.42	35.54	24.35
9	62.23	54.78	44.98	35.78	24.46
10	63.21	55.64	45.71	36.31	24.81
11	63.51	55.89	46.02	37.01	25.18
12	64.14	56.47	46.58	37.41	25.59
13	65.19	57.41	47.45	37.44	25.48
14	66.97	58.92	48.71	38.36	26.02
15	67.98	59.82	49.26	38.92	26.38
Area Avg	63.44	55.85	45.93	36.75	25.07

Table 13: Z/D=5 Target Wall Pitch Averaged Nusselt Number

Z/D=5 Target Wall Pitch Averaged Nusselt Number					
Jet No	Re=30,000	Re=24,800	Re=19,900	Re=15,000	Re=10,000
1	93.27	85.32	70.22	58.33	56.09
2	85.65	74.47	61.31	50.73	46.95
3	83.95	72.98	60.03	49.66	45.59
4	79.93	69.46	56.83	46.47	41.59
5	72.57	63.03	51.57	41.68	35.80
6	68.81	59.74	48.76	39.49	33.78
7	64.63	56.08	46.31	37.66	32.15
8	61.86	53.66	44.15	35.70	30.20
9	58.48	50.70	41.93	34.02	28.53
10	55.27	47.89	39.73	32.23	26.88
11	53.34	46.20	38.30	31.02	25.87
12	52.32	45.31	37.55	30.38	25.31
13	51.91	44.95	37.19	30.06	25.05
14	51.94	44.97	37.15	29.98	24.92
15	54.30	47.05	38.80	31.33	25.93
Area Avg	65.88	57.45	47.32	38.58	33.64

Table 14: Z/D=5 Side Wall Pitch Averaged Nusselt Number

Z/D=5 Side Wall Pitch Averaged Nusselt Number					
Jet No	Re=30,000	Re=24,800	Re=19,900	Re=15,000	Re=10,000
1	45.80	39.71	32.49	26.46	19.71
2	48.42	42.05	34.54	28.23	21.27
3	49.38	43.23	35.85	29.33	22.05
4	49.10	42.93	35.73	29.27	22.23
5	49.23	42.55	35.85	29.57	22.48
6	50.73	42.55	35.15	28.33	21.15
7	48.70	41.91	34.67	28.12	21.29
8	47.93	41.48	34.34	27.63	20.87
9	48.37	42.30	34.91	28.17	21.45
10	48.34	42.40	35.06	28.36	21.56
11	47.84	41.93	34.62	28.02	21.25
12	48.77	42.64	35.20	28.53	21.67
13	49.64	43.24	35.67	28.90	21.92
14	50.68	44.01	36.26	29.35	22.19
15	51.89	45.02	37.08	29.98	22.55
Area Avg	48.99	42.53	35.16	28.55	21.58

Table 15: Z/D=7 Target Wall Pitch Averaged Nusselt Number

Z/D=7 Target Wall Pitch Averaged Nusselt Number					
Jet No	Re=29,90 0	Re=25,10 0	Re=19,90 0	Re=15,00 0	Re=10,00 0
1	79.71	64.83	53.38	41.68	30.74
2	78.64	64.50	53.17	41.53	30.62
3	78.41	64.26	53.20	41.72	30.93
4	76.08	62.47	51.33	40.09	29.37
5	70.22	57.35	47.01	36.73	26.72
6	64.61	52.71	43.14	33.92	24.67
7	61.50	50.01	40.91	32.22	23.42
8	58.28	47.29	38.67	30.53	22.10
9	54.06	43.94	35.97	28.50	20.55
10	49.79	40.66	33.27	26.33	18.95
11	47.26	38.70	31.63	24.98	18.00
12	45.01	36.86	30.12	23.74	17.09
13	43.35	35.31	28.82	22.66	16.29
14	42.42	34.35	27.90	21.92	15.68
15	42.52	34.05	27.55	21.63	15.39
Area Avg	59.46	48.49	39.74	31.21	22.70

Table 16: Z/D=7 Side Wall Pitch Averaged Nusselt Number

Z/D=7 Side Wall Pitch Averaged Nusselt Number					
Jet No	Re=29,90 0	Re=25,10 0	Re=19,90 0	Re=15,00 0	Re=10,00 0
1	42.91	36.18	30.23	24.12	17.89
2	45.28	38.40	32.15	25.75	18.98
3	44.08	37.40	31.48	25.28	18.75
4	45.12	38.27	32.26	25.99	19.25
5	46.10	39.13	33.20	26.80	19.87
6	46.57	39.51	33.40	26.94	20.04
7	46.53	39.39	33.27	26.78	19.85
8	45.87	38.84	32.75	26.31	19.45
9	45.98	38.84	32.70	26.25	19.34
10	46.08	38.88	32.68	26.18	19.24
11	46.49	39.25	32.95	26.36	19.35
12	47.00	39.60	33.25	26.54	19.42
13	47.25	39.68	33.31	26.53	19.34
14	46.44	38.87	32.54	25.91	18.81
15	46.43	38.72	32.39	25.77	18.66
Area Avg	45.88	38.73	32.57	26.10	19.21

Table 17: Z/D=9 Target Wall Pitch Averaged Nusselt Number

Z/D=9 Target Wall Pitch Averaged Nusselt Number					
Jet No	Re=30,000	Re=25,100	Re=20,100	Re=15,000	Re=10,000
1	57.74	49.53	41.81	33.48	24.68
2	56.93	48.85	41.36	33.09	24.57
3	56.19	48.20	40.71	32.54	24.22
4	54.64	46.76	39.48	31.42	23.40
5	51.63	44.12	37.27	29.61	22.24
6	49.21	42.12	35.54	28.30	21.31
7	47.03	40.24	33.87	26.95	20.31
8	44.47	38.03	31.92	25.28	19.10
9	42.16	36.05	30.26	23.89	18.04
10	39.63	33.84	28.20	22.11	16.66
11	37.54	31.97	26.54	20.71	15.51
12	35.37	30.04	24.86	19.31	14.34
13	34.44	29.23	24.12	18.68	13.85
14	33.45	28.37	23.31	17.96	13.27
15	32.75	27.68	22.62	17.33	12.74
Area Avg	44.88	38.34	32.12	25.38	18.95

Table 18: Z/D=9 Side Wall Pitch Averaged Nusselt Number

Z/D=9 Side Wall Pitch Averaged Nusselt Number					
Jet No	Re=30,000	Re=25,100	Re=20,100	Re=15,000	Re=10,000
1	36.08	31.50	26.12	21.06	16.07
2	37.99	33.11	27.51	22.26	16.85
3	37.20	32.40	26.88	21.78	16.35
4	36.71	31.91	26.53	21.50	16.10
5	36.79	31.93	26.50	21.47	16.01
6	38.02	33.00	27.50	22.34	16.73
7	38.67	33.56	27.98	22.74	16.98
8	38.11	33.03	27.51	22.33	16.65
9	38.47	33.31	27.72	22.47	16.73
10	38.21	33.10	27.53	22.26	16.58
11	38.58	33.39	27.74	22.37	16.64
12	38.33	33.17	27.51	22.17	16.47
13	36.99	31.97	26.46	21.26	15.71
14	37.30	32.23	26.68	21.40	15.78
15	37.88	32.71	27.06	21.69	15.95
Area Avg	37.69	32.69	27.15	21.94	16.37

APPENDIX D: ACTUAL REYNOLDS NUMBERS

Table 19: Actual Reynolds Numbers

X/D	Y/D	Z/D	Reynolds number
5	4	1	4,900
			7,400
			10,100
			12,500
			14,500
		2	10,000
			15,000
			19,900
			24,900
			29,400
		3	9,900
			15,000
			19,900
			25,100
			30,200
		5	10,000
			15,000
			19,900
			24,800
			30,000
		7	10,000
			15,000
			19,900
			25,100
			29,900
9	10,000		
	15,000		
	20,100		
	25,100		
	30,000		

APPENDIX E: LATERAL CONDUCTION CALCULATIONS

Lateral Conduction Consideration

Thickness of foil heater

$$t := 50 \mu\text{m}$$

Sample volume width

$$\delta := 1 \text{mm}$$

Volume of sample volume

$$V := \delta^2 \cdot t$$

$$k := 20 \frac{\text{W}}{\text{m} \cdot \text{K}}$$

Heat flux

$$q_{\text{flux}} := 6000 \frac{\text{W}}{\text{m}^2}$$

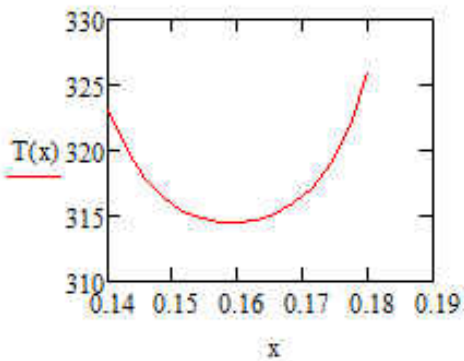
Volumetric heat generation

$$q_{\text{vol}} := \frac{q_{\text{flux}}}{t}$$

Temperature profile from the first row of impingement. ONLY valid for $.02 < x < .045$

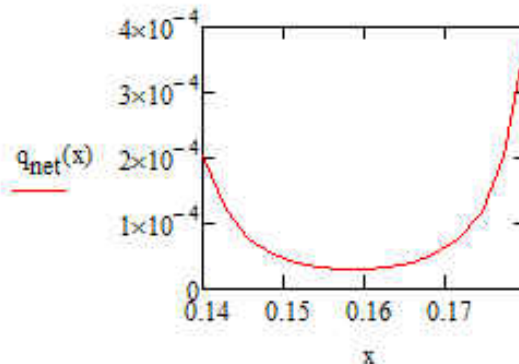
$$T(x) := 298 \text{K} + \frac{q_{\text{flux}}}{(-346049.69x^2 + 110116.18x - 8395.06) \frac{\text{W}}{\text{m}^2 \cdot \text{K}}}$$

$$x := \left(.14, \frac{.18 - .14}{N - 1} + .14, .18 \right)$$



$$A := \delta \cdot t$$

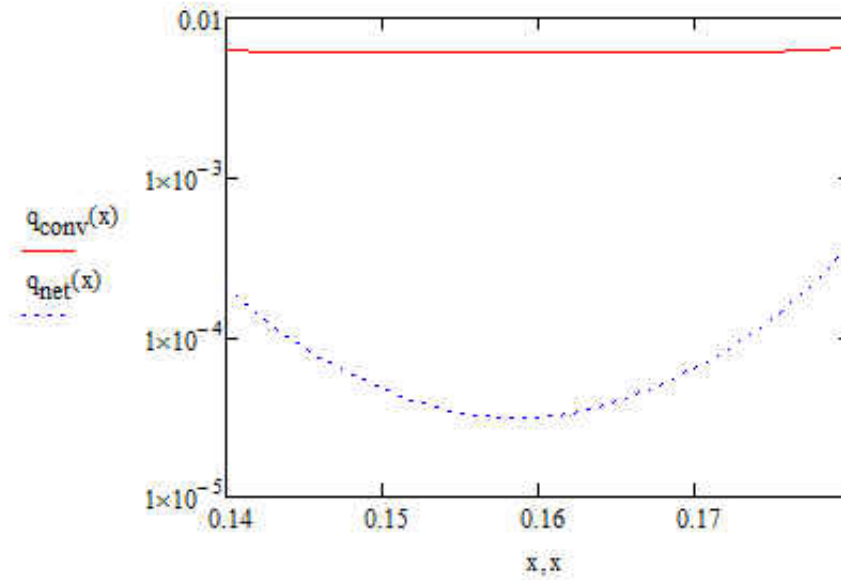
$$q_{\text{net}}(x) := A \cdot k \cdot \left(\frac{d}{dx} T \left(x + \frac{\delta}{m} \right) - \frac{d}{dx} T(x) \right) \frac{1}{m}$$



Now comparing the net heat gained by lateral conduction to heat generated and convected out,

$$q_{\text{gen}} := q_{\text{vol}} \cdot V = 6 \times 10^{-3} \text{ W}$$

$$q_{\text{conv}}(x) := \delta^2 \cdot q_{\text{flux}} + q_{\text{net}}(x)$$



It can be seen that the lateral conduction into the sample volume is two orders of magnitude smaller than the heat removed by convection.

REFERENCES

- [1] U. E. I. Administration, "Annual energy Review," DOE/EIA-0384(2011), Washington DC, 2012.
- [2] J. P. Downs and K. K. Landis, "Turbine Cooling Systems Design - Past, Present and Future," in *Proceedings of ASME Turbo Expo*, GT2009-59991, 2009.
- [3] R. S. Bunker, "Gas Turbine Heat Transfer: Ten Remaining Hot Gas Path Challenges," *Journal of Turbomachinery*, vol. 129, no. April, pp. 193-201, 2007.
- [4] J. C. Han and S. E. S. Dutta, *Gas Turbine Heat Transfer and Cooling Technology*, New York: Taylor & Francis, Inc., 2000.
- [5] L. A. El-Gabri and D. A. Kaminski, "Numerical investigation of jet impingement with crossflow - Comparison of Yang-Shih and standard k-e turbulence models," *Numerical Heat Transfer*, vol. 47, pp. 441-469, 2005.
- [6] M. Zuckerman and N. Lior, "Impingement Heat Transfer: Correlations and Numerical Modeling," *Journal of Heat Transfer*, vol. 124, p. 544, 2005.
- [7] K. S. Mushatat, "Analysis of the turbulent flow and heat transfer of the impingement cooling in a channel with cross flow," *Journal of King Abdulaziz University*, vol. 18, no. 2, pp. 101-122, 2007.
- [8] M. E. Taslim, K. Bakhatari and H. Liu, "Experimental and numerical investigation of impingement on a rib-roughened leading-edge wall," *Journal of Turbomachinery*, vol. 125, pp. 682-691, 2003.
- [9] S. Acharya, A. Eshtiaghi and R. Schilp, "Flow distribution and heat transfer coefficients

- inside gas holes discharging into an orthogonal cross flow," *International Journal of Heat and mass transfer*, vol. 55, pp. 7036-7045, 2012.
- [10] P. Gulati, V. Katti and S. Prabhu, "Influence of the shape of the nozzle on local heat transfer distribution between smooth flat surface and impinging air jet," *International Journal of Thermal Sciences*, vol. 48, pp. 602-617, 2009.
- [11] R. Herrero Martin and J. M. Buchlin, "Jet impingement heat transfer from lobed nozzles," *International Journal of Thermal Sciences*, vol. 50, pp. 1199-1206, 2011.
- [12] J. Lee and S.-J. Lee, "The effect of nozzle configuration on stagnation region heat transfer enhancement of axisymmetric jet impingement," *International Journal of Heat and Mass Transfer*, vol. 43, pp. 3497-3509, 2000.
- [13] H. Martin, "Heat and Mass Transfer between Impinging Gas Jets and Solid Surfaces," *Advances in Heat Transfer*, 1977.
- [14] R. Viskanta, "Heat Transfer to Impinging Isothermal Gas and Flame Jets," *Experimental Thermal and Fluid Science*, vol. 6, pp. 111-134, 1993.
- [15] B. Weigand, "Multiple Jet Impingement - A Review," *Heat Transfer Research*, vol. 42, no. 2, pp. 101-142, 2011.
- [16] C. Carcasci, "An experimental investigation on air impinging jets using visualisation methods," *International Journal of Thermal Science*, vol. 38, pp. 808-818, 1999.
- [17] L. Florschuetz, R. A. Berry and D. E. Metzger, "Periodic Streamwise Variations of Heat Transfer Coefficients for Inline and Staggered Arrays of Circular Jets with Cross Flow of Spent Air," *Journal of Heat Transfer*, vol. 102, pp. 132-137, 1980.

- [18] L. W. Florschuetz, C. R. Truman and D. E. Metzger, "Streamwise Flow and Heat Transfer Distributions for Jet Array Impingement with Cross flow," *Journal of Heat Transfer*, vol. 103, p. 337, 1981.
- [19] L. W. Florschuetz and Y. Isoda, "Flow Distributions and Discharge Coefficient for Jet Array Impingement with Initial Cross Flow," *Journal of Engineering for Power*, vol. 105, p. 296, 1983.
- [20] Y.-H. Liu, S.-J. Song and Y.-H. Lo, "Jet impingement heat transfer on target surfaces with longitudinal and transverse grooves," *International Journal of Heat and Mass Transfer*, vol. 58, pp. 292-299, 2013.
- [21] D. E. Metzger and R. J. Korstad, "Effects of crossflow on impingement heat transfer," *Journal of Engineering for Power*, pp. 35-41, 1972.
- [22] J.-Y. San and W.-Z. Shiao, "Effects of jet plate size and plate spacing on the stagnation Nusselt number for a confined circular air jet impinging on a flat surface," *International Journal of Heat and Mass Transfer*, vol. 49, pp. 3477-3486, 2006.
- [23] J.-Y. San and M.-D. Lai, "Optimum jet-to-jet spacing of heat transfer for staggered arrays of impinging air jets," *International Journal of Heat and Mass Transfer*, vol. 44, no. 21, pp. 3997-4007, 2001.
- [24] K. W. Van Treuren, Z. Wang, P. Ireland, T. V. Jones and S. Kohler, "Comparison and prediction of local and average heat transfer coefficients under an array of inline and staggered impinging jets," in *International Gas Turbine and Aeroengine Congress*, Birmingham, UK, 1996.

- [25] A. C. Chambers, D. R. H. Gillespie, P. T. Ireland and G. M. Dailey, "The effect of initial cross flow on the cooling performance of a narrow impingement channel," *Journal of Heat Transfer*, vol. 127, pp. 358-365, 2005.
- [26] J. Park, M. Goodro, P. Ligrani, M. Fox and H.-K. Moon, "Separate effects of Mach number and Reynolds number on jet array impingement heat transfer," *Journal of Turbomachinery*, vol. 129, pp. 269-280, 2007.
- [27] M. Goodro, J. Park, P. Ligrani, M. Fox and H.-K. Moon, "Effects of hole spacing on spatially-resolved jet array impingement heat transfer," *International Journal of Heat and Mass Transfer*, vol. 51, pp. 6243-6253, 2008.
- [28] H. H. Cho and D. H. Rhee, "Local heat/mass transfer measurement on the effusion plate in impingement/effusion cooling systems," *Journal of Turbomachinery*, vol. 123, pp. 601-608, 2001.
- [29] A. J. Onstand, C. J. Elkins, R. J. Moffat and J. K. Eaton, "Full-field flow measurements and heat transfer of a compact jet impingement array with local extraction of spent fluid," *Journal of Heat Transfer*, vol. 131, pp. 1-8, 2009.
- [30] R. S. Bunker and D. E. Metzger, "Local heat transfer in internally cooled turbine airfoil leading edge regions: Part I - Impingement cooling without film coolant extraction," *Journal of Turbomachinery*, vol. 112, pp. 451-458, 1990.
- [31] D. E. Metzger and R. S. Bunker, "Local heat transfer in internally cooled turbine airfoil leading edge regions: Part II - Impingement cooling with film coolant extraction," *Journal of Turbomachinery*, vol. 112, pp. 459-466, 1990.

- [32] D. R. H. Gillespie, Z. Wang, P. T. Ireland and S. T. Kohler, "Full surface local heat transfer coefficient measurements in a model of an integrally cast impingement cooling geometry," *Journal of Turbomachinery*, vol. 120, pp. 92-99, 1998.
- [33] H. Deng, Z. Gu, J. Zhu and Z. Tao, "Experiments on impingement heat transfer with film extraction flow on the leading edge of rotating blades," *International Journal of Heat and Mass Transfer*, vol. 55, pp. 5425-5435, 2012.
- [34] M. Fenot, E. Dorignac and J.-J. Vullierme, "An experimental study on hot round jets impinging a concave surface," *International Journal of Heat and Mass Transfer*, vol. 29, pp. 945-956, 2008.
- [35] W. M. Yan and S. Mei, "Measurement of detailed heat transfer along rib-roughened surface under arrays of impinging elliptic jets," *International Journal of Heat and Mass Transfer*, vol. 49, pp. 159-170, 2006.
- [36] W. M. L. H. S. C. Y. W. Yan, "Experimental study of impinging heat transfer along rib-roughened walls by using transient liquid crystal technique," *International journal of Heat and Mass Transfer*, vol. 48, pp. 2420-2428, 2005.
- [37] K. Kanokjaruvijit and R. F. Martinez-Botas, "Jet impingement on a dimpled surface with different crossflow schemes," *International Journal of Heat and mass Transfer*, vol. 48, pp. 161-170, 2005.
- [38] A. P. Rallabandi, D.-H. Rhee, Z. Gao and J. Han, "Heat transfer enhancement in rectangular channels with axial ribs or porous foam under through flow and impinging jet conditions," *International Journal of Heat and Mass Transfer*, vol. 53, pp. 4663-4671, 2010.

- [39] S. V. Ekkad and D. Kontrovitz, "Jet impingement heat transfer on dimpled target surfaces," *International journal of heat and Fluid Flow*, vol. 23, pp. 22-28, 2002.
- [40] K. V. Akella and J.-C. Han, "Impingement cooling in rotating Two-Pass Rectangular Channels with Ribbed Walls," *Journal of Thermophysics and Heat Transfer*, vol. 13, no. 3, pp. 364-371, 1999.
- [41] Q. Liu, A. Sleiti and J. Kapat, "Application of pressure and temperature sensitive paints for study of heat transfer to a circular impinging air jet," *International Journal of Thermal Sciences*, vol. 47, pp. 749-757, 2008.
- [42] Q. Liu, Study of Heat Transfer Characteristics of Impinging Air Jet Using Pressure and Temperature Sensitive Luminescent Paint, University of Central Florida Dissertation, 2006.
- [43] F. Incropera, Fundamentals of Heat and Mass Transfer, Hoboken: Wiley, 2006.
- [44] M. Ricklick and J. Kapat, "Sidewall effects on heat transfer coefficient in a narrow impingement channel," *Journal of Thermophysics and Heat Transfer*, vol. 24, no. 1, pp. 123-132, 2010.
- [45] B. D. Figliola R.S., Theory and Design for Mechanical Measurements, Hoboken: Wiley, 2006.